8-1-2018

# Translating Data from the Laboratory into Simulation: A Computational Framework for Subject-Specific Finite Element Musculoskeletal Simulation

Donald R. Hume
*University of Denver*

## Recommended Citation

Hume, Donald R., "Translating Data from the Laboratory into Simulation: A Computational Framework for Subject-Specific Finite Element Musculoskeletal Simulation" (2018). *Electronic Theses and Dissertations*. 1499.
https://digitalcommons.du.edu/etd/1499

# Translating Data from the Laboratory into Simulation: A Computational Framework for Subject-Specific Finite Element Musculoskeletal Simulation

## Abstract

Computational modeling is a powerful tool which has been used to inform decisions made by engineers, scientists, and clinicians for decades. Musculoskeletal modeling has emerged as a computational modeling technique used to understand the interaction between the body and its surroundings. There are several common approaches used for musculoskeletal modeling which take advantage of different model formulations to obtain information of interest. Unfortunately, models with different joint formulations inherit disparities in representations of ligament, muscle, and cartilage at joints of interest. These differences affect the way the joint functions and limit the insight it provides through computational analysis. Musculoskeletal models with high fidelity joint representations in a finite element framework have become increasingly viable in recent years, but three challenges limit progression: *model personalization*, *modeling infrastructure*, and *computational efficiency*. The goal of musculoskeletal modeling is almost entirely to understand the motion of the body, the mechanics of the joints, and the strain on the tissues in subjects performing various activities. These interests require models that act as the subject's body would – a very complex task. Improving on methods in *model personalization* for calibrating joint strength, soft tissue response, and modeling geometry will continue to drive this work toward true subject specificity. Previously, software has been released which provides a *modeling infrastructure* for musculoskeletal modeling using rigid body dynamics. No such framework exists to build and perform musculoskeletal modeling with high fidelity joint representations in a finite element environment. A computational framework which provides methods to scale models and estimate joint kinematics and muscle forces directly from laboratory data would improve the accessibility and usability of these complex techniques. Developing tools which promote *computational efficiency* and manage effective parallelization of simulation and optimization will help improve the usability of musculoskeletal finite element modeling. The purpose of this work was to improve upon methods in musculoskeletal finite element modeling by developing novel techniques to evolve the current state-of-the-art in this area of research. Specifically, the first study calibrated the knee strength response of a musculoskeletal model of the lower limb to healthy data collected from subjects. The model was then used in the second study to perform concurrent estimation of muscle forces and tissue strain in subjects performing two activities. The third study considered markerbased motion and compared it to kinematics obtained from stereo radiography-based bone tracking. As part of this study a new set of polynomial splines describing the motion in 5 degrees of freedom at the knee were provided. Lastly, a computational framework was developed which served to scale a generic musculoskeletal finite element model and perform estimations of joint kinematics and muscle forces directly from laboratory data. The goal of this dissertation was to increase the accessibility of a powerful modeling approach to researchers around the globe by developing and advancing techniques which improve the usability of these methods.

## Document Type

Dissertation

## Degree Name

Ph.D.

## Department

Mechanical Engineering

## First Advisor

Kevin B. Shelburne, Ph.D.

## Second Advisor

Paul Rullkoetter

## Third Advisor

Peter Laz

## Keywords

Finite element, Muscle, Musculoskeletal, Simulation

## Subject Categories

Engineering | Mechanical Engineering

## Publication Statement

# Translating Data from the Laboratory into Simulation: A Computational Framework for Subject-Specific Finite Element Musculoskeletal Simulation

---

A Dissertation

Presented to

the Faculty of the Daniel Felix Ritchie School of Engineering and Computer Science

University of Denver

---

In Partial Fulfillment

of the Requirements for the Degree

Doctor of Philosophy

---

by

Donald R. Hume

August 2018

Advisor: Kevin B. Shelburne

Author: Donald Hume
Title: Translating Data from the Laboratory into Simulation: A Computational Framework for Subject-Specific Finite Element Musculoskeletal Simulation
Advisor: Kevin B. Shelburne
Degree Date: August 2018

# ABSTRACT

Computational modeling is a powerful tool which has been used to inform decisions made by engineers, scientists, and clinicians for decades. Musculoskeletal modeling has emerged as a computational modeling technique used to understand the interaction between the body and its surroundings. There are several common approaches used for musculoskeletal modeling which take advantage of different model formulations to obtain information of interest. Unfortunately, models with different joint formulations inherit disparities in representations of ligament, muscle, and cartilage at joints of interest. These differences affect the way the joint functions and limit the insight it provides through computational analysis. Musculoskeletal models with high fidelity joint representations in a finite element framework have become increasingly viable in recent years, but three challenges limit progression: *model personalization*, *modeling infrastructure*, and *computational efficiency*. The goal of musculoskeletal modeling is almost entirely to understand the motion of the body, the mechanics of the joints, and the strain on the tissues in subjects performing various activities. These interests require models that act as the subject's body would – a very complex task. Improving on methods in *model personalization* for calibrating joint strength, soft tissue response, and modeling geometry will continue to drive this work toward true subject specificity. Previously, software has been released which provides a *modeling infrastructure* for musculoskeletal modeling using rigid body dynamics. No such framework exists to build and perform musculoskeletal modeling with high fidelity joint representations in a finite element environment. A computational framework which provides methods to scale models and estimate joint kinematics and muscle forces directly from laboratory data would improve the accessibility and usability of these complex techniques. Developing tools which promote *computational efficiency* and manage effective parallelization of simulation and optimization will help improve the usability of musculoskeletal finite element modeling. The purpose of this work was to improve upon methods in musculoskeletal finite element modeling by developing novel techniques to evolve the current state-of-the-art in this area of research. Specifically, the first study calibrated the knee strength response of a musculoskeletal model of the lower limb to healthy data collected from subjects. The model was then used in the second study to perform concurrent estimation of muscle forces and tissue strain in subjects performing two activities. The third study considered marker-based motion and compared it to kinematics obtained from stereo radiography-based bone tracking. As part of this study a new set of polynomial splines describing the motion in 5 degrees of freedom at the knee were provided. Lastly, a computational framework was developed which served to scale a generic musculoskeletal finite element model and perform estimations of joint kinematics and muscle forces directly from laboratory data. The goal of this dissertation was to increase the accessibility of a powerful modeling approach to researchers around the globe by developing and advancing techniques which improve the usability of these methods.

# ACKNOWLEDGEMENTS

This journey has been a difficult one, and I’m not sure I’d be writing these words without the support of some very important people in my life. The statistic that “39% of graduate students are suffering from moderate to severe depression” is terrifying and admittedly relatable. Without my family to provide overwhelming support I would have quit sometime near the beginning of my third year. So, first and foremost thanks to my wife, Chels, and my family who held me up when things felt most grim.

Next, I’d like to thank my adviser, Dr. Kevin Shelburne, for helping me traverse the PhD as an academic mentor while distinguishing himself through his kindness and excellent character. He’s demonstrated to me what it means to be a good mentor, but more importantly what it means to be a good human being. Thanks Kev.

I’d also like to thank some of my colleagues for their help and contributions seen throughout this dissertation. The work presented here paralleled work by Drs. Navacchia and Ali in both subject and timing. I am grateful for their contributions over the past several years. My dissertation, and our laboratory in general, has been supported by the guidance of faculty that have fostered a unique research environment which I am lucky to have been a part of, so thank you to Drs. Paul Rullkoetter, Peter Laz, Bradley Davidson, and Chadd Clary.  Furthermore, our lab has seen a very tight knit group over the years, and I’d be remiss not to thank the other members: Gaffney, Myers, Simons, Sintini, Kefala, Wilson, Behnam, and Burton. I’ll conclude by thanking anyone else who has been there when I’ve needed them to be. Thank you all.

# TABLE OF CONTENTS

# LIST OF TABLES

# LIST OF FIGURES

# CHAPTER 1. INTRODUCTION

## 1.1. Introduction

"How beauteous mankind is! O brave new world that has such people in't" marveled Miranda in Shakespeare's *The Tempest* (5.1.182-183). Undeniably, mankind is wrought of beauty as seen through many lenses, most importantly the lens of a philosopher or scientist. There is much that is yet unknown to humans about our very existence and it is this unknown which serves as the impetus to propel our understanding and quench this hunger. The rate at which our technological prowess as a civilization drives forward discoveries in medicine, science, and mathematics is certainly the reality of this *brave new world*.

Research performed on the human body, specifically musculoskeletal research, has seen an enormous spike in the past 50 years as advances in technology have paved the way for discoveries in science, medicine, and engineering. Experimental research is the primary approach used to investigate causal relationships found in science. It can be further divided into *in vivo*, meaning in life, and *in vitro*, meaning in the glass. *In vivo* research allows for the inspection of the body in people or animals that are alive and can be asked to perform complex motions and tasks. This technique allows for a better understanding of the whole body and joint scales but is limited in the ability to explore internal quantities of interest at the tissue or cellular scales. Additionally, the body is a complex system, and it is often difficult to isolate the contribution of individual tissues in response to force and motion. *In* *vitro* experiments allow for the analysis of bone, ligaments, and muscles in cadaveric specimens. Mechanical testing can be used to determine precise response of tissue or joints to exact loading and unloading conditions. *In vitro* analysis is costly which can be prohibitive of continued use. Furthermore, it requires a precise application of force and motion. Given this requirement, it is difficult to apply experimental loading conditions to mimic conditions experienced *in vivo*.

Computational modeling has emerged as a technique to bridge the gap between *in vivo* and *in vitro* experimental research. This technique allows researchers to replicate parts of the body at a variety of scales depending on the scope of research. With ample validation, models can be used to analyze design alternatives, predict patient outcomes, and suggest improvements to surgical technique and implant design without having to implement what could otherwise be a costly or dangerous practice. However, no two people are alike, which makes it difficult to use computational modeling to effectively model inherent subject-variability. Care must be taken to properly validate models appropriately at each scale being considered. For example, to properly validate the contributions of ligaments to stability at the knee, both the individual ligament tissue models, and the entire joint soft tissue response to loading should be considered.

Rigid body dynamics applications specific to musculoskeletal modeling have improved modeling accessibility to researchers around the globe. These software packages use whole body modeling to estimate kinematics, kinetics, and muscle forces but fail to capture high-fidelity detail at joints of interest. Rigid body musculoskeletal models frequently represent the joint as a simple hinge (Anderson and Pandy, 2001a) or using average measurements taken from cadaveric knees (Arnold et al., 2010; Delp et al., 2007). These approaches likely misrepresent the joint and prevent any passive or active joint deformability which plays a large role in muscle force estimations and joint strength. Furthermore, current musculoskeletal models use muscle modeling parameters obtained from cadaveric specimens (Arnold et al., 2010; Ward et al., 2007), which when coupled with single fiber muscle representations often fail to capture the force generating characteristics of the muscle over the entire excursion of the joint (Blemker and Delp, 2006, 2005; Herzog and ter Keurs, 1988). Finite element analysis allows for modeling of details such as wrapping of ligament and muscle (Fitzpatrick et al., 2010), complex material properties (Ali et al., 2017; Blemker and Delp, 2005; Fernandez and Hunter, 2005), and deformable contact (Ali et al., 2017; Armitage and Oyen, 2017; Yao et al., 2008). Opportunities for improvements in the field of computational biomechanics can be divided into three areas: *model personalization*, *modeling infrastructure*, and *computational efficiency*. *Model personalization* seeks to improve the sophistication and representation of subject and specimen-specific models. Model behavior is directly affected by its shape, size, and the way the muscles and soft tissue are represented. The increase in modeling capabilities seen in finite element modeling comes with an increase in complexity of the model and simulations. Currently, no software exists to estimate kinematics, kinetics, and muscle forces in a single framework finite element simulation. Development of *modeling infrastructure* to streamline the creation of simulations would help to improve the usability and repeatability of this powerful technology. The third opportunity, *computational efficiency*, is also related to finite element musculoskeletal simulations. These simulations are computationally slow when compared to rigid body dynamics models which take only a few minutes to run. To facilitate optimization-based finite element models which estimate kinematics and muscle forces, improvements need to be made in parallelization and efficiency to improve the feasibility of these models in computational biomechanics.

## 1.2. Objectives

The objective of this dissertation was to address limitations in computational modeling associated with model personalization, modeling infrastructure, and computational efficiency. The first specific objective was to calibrate two existing lower extremity musculoskeletal finite element models to healthy subject strength measurements. This objective helped to improve personalization and highlight changes to muscle and model geometry with a deformable joint representation when compared to a simplified joint representation. The second specific objective was to estimate muscle forces for two subject models during two tasks: stance phase of gait and chair rise. This objective incorporated new modeling infrastructure to perform single framework muscle force estimations and demonstrated the feasibility of a single framework approach. The final specific objective was to develop a computational framework to aid in the translation of laboratory data to finite element simulation. This framework improved modeling infrastructure by including techniques to scale models, and estimate joint kinematics, kinetics, and muscle forces. Computational efficiency was a large consideration of this final objective and was improved through the implementation of a core application programming interface (API) which managed asynchronous process control during estimation of muscle forces and joint kinematics.

### 1.3. Dissertation Overview

Chapter 2 provides a review of recent literature associated with the field of musculoskeletal biomechanics. The chapter describes current approaches to musculoskeletal modeling and concludes with discussion on the benefits of single framework musculoskeletal modeling.

Chapter 3 presents *The Interaction of Muscle Moment Arm, Knee Laxity, and Torque in a Multi-Scale Musculoskeletal Model of the Lower Limb* whose objective was to demonstrate the impact of a deformable joint representation on muscle moment arms and joint torque in a multi-scale musculoskeletal finite element model of the lower limb. This work is in press with the Journal of Biomechanics (Hume et al., in press).

Chapter 4 presents *Simulation of Activity Using a Multi-Scale Finite Element Model of the Lower Limb* whose objective was to estimate muscle forces for two subjects during two activities: the stance phase of gait and a chair rise. Muscle forces, ligament loads, tibiofemoral and patellofemoral contact forces, and center of pressure locations were compared for different subjects and tasks to highlight feasibility of muscle force estimation and soft tissue analysis in a single framework musculoskeletal finite element model.

Chapter 5 presents *Comparison of Marker-Based and Stereo Radiography Knee Kinematics in Activities of Daily Living* whose objective was to compare kinematics obtained through optical motion capture to kinematics obtained from radiography-based bone tracking and discuss the reliability of marker-based methods in a variety of activities. Updated polynomial equations for secondary degrees of freedom as a function of flexion angle were developed from radiography-based kinematics of knee extension and compared to previous results obtained from cadavers. This work is in press with Annals of Biomedical Engineering (Hume et al., in press).

Chapter 6 presents *A Computational Framework for Building Explicit Finite Element Musculoskeletal Simulations Directly from Laboratory Data* whose objective was to demonstrate a single framework to scale models and estimate joint kinematics, kinetics, and muscle forces in a musculoskeletal model of the lower limb directly from laboratory marker and force plate data.

Chapter 7 discusses the contributions to the field of computational biomechanics made by this dissertation and suggests direction for future work in this field.

# CHAPTER 2. BACKGROUND INFORMATION AND LITERATURE REVIEW

## 2.1. Experimental Biomechanics

Biomechanics is the study of the mechanical laws relating to the movement or structure of living organisms. Biomechanical studies have been cited dating back to the 17th century by scientists such as Giovanni Alfonso Borelli who studied animal locomotion, but improvements in medicine, imaging, and computational capabilities have led to a sharp increase in biomechanical interest in the past fifty years. The desire to understand the human body and how it responds to the world around it is an ideology which has helped drive changes in medicine, surgical intervention, and clinical practice. Musculoskeletal modeling is one specific form of biomechanical analysis which employs deterministic models to allow for investigation into regions of interest in the body. It allows researchers to gain insight into the interaction of muscle and joint mechanics that cannot practically be measured by simple observation alone. Musculoskeletal modeling is supported almost entirely by the *in vivo* study of human motion and the *in vitro* study of tissues.

### 2.1.1. In Vivo Experimental Analysis

The *in vivo* study of human locomotion is a dominant area of biomechanics and has helped researchers to quantify healthy and pathologic kinematics and control strategies. The task of reaching down to pick up a washcloth might be conducted differently when performed by a healthy individual, an individual with a hip or shoulder replacement, or an individual with limb amputation. It is the desire to understand these differences which drives *in vivo* research and data analysis. Data collection in the laboratory is supported by a number of different technologies which help to obtain measurements that are of great importance to researchers. The “standard” motion analysis laboratory consists of optical motion capture used to track the Euclidian motion of markers affixed to regions of interest, force plates to record the reaction forces and moments imparted by the ground on the body, and electromyography to quantify the activation of muscles driving motion of the body during various activities. Analyses have been performed on lower extremity kinematics and kinetics in adults (DeVita et al., 2016; Kadaba et al., 1990; Schipplein and Andriacchi, 1991) and children (Bell et al., 2002; Chen et al., 1998; MacWilliams et al., 2003) using these technologies. Although less common, dynamic radiography has also become a valuable tool in clinical research to better understand the underlying motion of the bones (Kefala et al., 2017; Myers et al., 2012; Torry et al., 2011), which often occurs at levels such as a few millimeters or degrees. Despite the many benefits, *in vivo* data collection does not allow researchers to access internal quantities of interest. As an example, despite realizing the motion of the knee joint using marker-based or dynamic radiography-based kinematics during walking, it is currently impossible to know the amount of force in the ACL or the contact pressure on the meniscus using non-invasive techniques. Furthermore, *in vivo* data collections can be cost prohibitive and require extensive approval processes by an institutional review board.

### 2.1.2. In Vitro Experimental Analysis

*In vitro* analyses allow for the study of tissues of cadaveric specimens in any area of the body. This permits a wide range of studies to be performed which may not otherwise be possible during *in vivo* experiments. Material properties of ligaments (Bigliani et al., 1992; Chandrashekar et al., 2006; Woo et al., 1991), cartilage (Chen et al., 2001), muscle (Ward et al., 2009), and bone (Sueyoshi et al., 2017) may be ascertained through compressive, tensile, and fatigue analysis. Experimental testing can also be performed at the joint level to see how the joint as a system responds to loading and changes in kinematics. Cyr et al. (2015) mapped loading of the superficial medial collateral ligament to total joint contact force at various flexion angles and applied loading conditions (Cyr et al., 2015). Though informative, *in vitro* testing fails to capture the information about *in vivo* conditions which researchers are keen to explore. To step closer to *in vivo* motion, some researchers have developed joint simulators of the spine (Mannen et al., 2015), knee (Maletsky and Hillberry, 2005), and shoulder (Gulotta et al., 2012) to prescribe physiological motion and loading while examining internal quantities otherwise inaccessible. These simulators simplify the joint representations to facilitate the application of loads and kinematics. For example, the Kansas Knee Simulator (KKS) (Maletsky and Hillberry, 2005) represented the quadriceps tendon using a single line of action and neglected hamstrings representation. While joint simulators allow for more realistic application of joint loads and kinematics, they fall short in accurately representing *in vivo* loading conditions.

## 2.2. Computational Modeling in Biomechanics

Computational modeling allows researchers to build deterministic computer-based models to analyze fracture, structural, and fluid mechanics in components or regions of interest. In the field of biomechanics, computational modeling acts to complement *in vivo* and *in vitro* experimental analysis. As discussed throughout section 2.1.1 and 2.1.2, *in vivo* analysis allows researchers to examine and evaluate the motion of the body through a lens that prohibits quantitative understanding of mechanics and dynamics experienced by tissues inside the body. *In vitro* analysis partly fills this gap by allowing researchers to perform exploratory science by testing the mechanics of materials, considering changes in surgical intervention, and examining features of the body that are not readily available during *in vivo* analysis. Computational biomechanics bridges the gap between these two approaches to experimental biomechanics through the creation of computer simulations which, when properly validated, can shed light onto the internal mechanics of the joint experienced during complex activities.

Validation is a crucial part of building effective computational models in any area of science and should be present at each scale being considered. Validation is the process of confirming that the predictions of a computational model match a known outcome. This can be achieved by comparison to analysis performed in *in vivo* or *in vitro* experiments. This work considers the whole body and joint scales, but computational models may also consider research at the tissue, cellular, and atomic scales as well. Regardless of the scope, care must be taken to ensure the ability of the model to accurately describe what is being represented. Building computational models which mimic in vitro experimental analysis is a common way to highlight validity of model response and improve faith in computational results. For example, computational models were built to accurately mimic indentation results of a healthy cartilage-bone interface (Armitage and Oyen, 2017) and tissue engineered cartilage constructs (Meloni et al., 2017). Computational models are often built to mimic experimental testing and joint simulators such as those discussed previously. Baldwin et al. (2009) developed a model to mimic the experimental setup of the KKS and used it to verify specimen-specific patellofemoral kinematics obtained from a finite element representation of the knee (Figure 2.1) (Ali et al., 2016; Baldwin et al., 2009). Harris et al. (2016) calibrated ligament material properties and geometry in finite element models of healthy knee specimens to match load displacement profiles obtained from in vitro experiments (Harris et al., 2016).

Computational modeling in biomechanics can be divided into three approaches: whole body modeling using rigid body dynamics applications, high fidelity joint modeling using finite element analysis, and a hybrid approach which uses whole body modeling in sequence with high fidelity joint models, each with benefits and limitations.

## 2.3. Whole Body Musculoskeletal Modeling

### 2.3.1. Applications

Whole body musculoskeletal models provide a method to take data from the motion analysis laboratory and estimate joint kinematics, joint kinetics, and muscle forces. Most commonly built in rigid body dynamics software packages (OpenSim, AnyBody), they consist of bony geometry constrained by joints with linear musculotendon actuators running along the bones. These models routinely neglect ligaments and articular contact and represent joints such as the knee as a simple hinge (Anderson and Pandy, 2001a) or prescribe secondary degrees of freedom (DOF) as a function of knee flexion angle (Arnold et al., 2010; Blemker et al., 2007; Rajagopal et al., 2016; Thelen and Anderson, 2006). These simplifications made to the joints help facilitate calibration of parameters defining muscle geometry such as moment arm, and parameters defining force development such as tendon slack length. Simply put, these models do not deform kinematically to internal or external loads imparted on the joint. They can be used for the estimation of muscle forces but do not give insight into joint mechanics.

Despite these limitations, whole body musculoskeletal modeling has had an incredible impact on the field of biomechanics. Beginning as a tool to evaluate potential surgical intervention (Delp et al., 1990), the open source software application OpenSim (OpenSim, Stanford, CA) has improved accessibility to musculoskeletal modeling for the biomechanics research community. Recent work has used OpenSim to examine medial compartment loading in subjects with osteoarthritis (Richards and Higginson, 2010) and obese children (Lerner et al., 2014), variations in joint kinematics during walking in healthy and obese populations (Haight et al., 2014), and metabolic costs estimated during the stance and swing phases of gait (Umberger, 2010). The ability to efficiently estimate muscle forces, whole body kinematics, and joint reaction forces will maintain OpenSim’s place in the field of computational biomechanics.

### 2.3.2. Muscle Representation

In the body, the geometries of muscles are defined by their attachments to bone as an origin and insertion location, the direction of fiber orientation or *pennation angle*, and the physiological cross-sectional area which determines max force generating capability. The ability to measure and represent muscle geometry appropriately is paramount to effective estimation of muscle forces.

The path of the muscle is an important feature to be considered in musculoskeletal models to maintain accurate joint representations. The path a muscle takes determines its moment arm, or the effectiveness of the muscle about a joint. Determined partly by the insertion and origin, the muscle and tendon complex is commonly represented as a linear musculotendon unit which follows the path of the muscle centroid (Jensen and Davy, 1975). The musculotendon path is held in place by a series of via points and geometric primitives which enable wrapping over joints. Muscles with broad insertions into the bone are often represented by several fibers, such as the deltoid muscle located at the shoulder. Some models have multifiber representations for all muscles, with the goal to more effectively facilitate force production over the entire range of muscle excursion (Carbone et al., 2015).

Moment arm as it relates to muscle modeling is defined as the effectiveness of a particular muscle at generating a particular motion of interest, such as knee flexion during gait (Sherman et al., 2015). Geometrically, the muscle moment arm can be described as the perpendicular distance from the muscle to the center of rotation of the joint. This is a difficult quantity to visualize, as the instantaneous center of rotation of the joint changes significantly even in simple tasks such as gait (Koo and Andriacchi, 2008). An incorrect description of muscles moment arms can have large effects on joint torque but also incorrectly bias the muscle force estimation strategy, which often favors muscles based on how effective they are. There are several methods for estimating muscle moment arm. The first is the tendon excursion method which is based on the principle of virtual work and estimates moment arm as the change in length with respect to the change in joint angle (An et al., 1984). This method assumes inextensibility of the musculotendon unit and treats contact as a workless constraint. A second method to calculate moment arm is the estimation of effective moment arm (Grood et al., 1984), which can be defined as the ratio of reaction torque at the joint to the applied muscle force. This method assumes the joint acts as a simple lever mechanism and can be expressed numerically:

$$\tau = MA \times F$$

where tau is measured reaction torque at the joint and F is the applied force by the muscle. Taking the derivative of both sides and rearranging terms develops a numerical estimation of moment arm:

$$MA = \frac{d\tau}{dF}$$

Thus, the change in output torque divided by the change in input force describes the effective moment arm of the muscle. Muscle moment arm measurements are often performed *in vitro* (Arnold et al., 2010; Buford et al., 1997, 2001; Grood et al., 1984), and the results have been used to support the development and validation of musculoskeletal geometry (Arnold et al., 2010; Delp et al., 2007). Defining rigid representations of the muscle path and moment arm encourages effective muscle force and joint reaction force prediction in whole body musculoskeletal modeling, however it does not facilitate changes to musculoskeletal geometry given change in applied muscle force.

### 2.3.3. Muscle Force Estimation

Force production in muscles is a complex cascade of electrochemical signaling between the brain and muscle. In skeletal muscle, fibrils make up fascicles, and fascicles make up fibers which are oriented in parallel along the line of action. Muscle fibrils are constituted of sarcomeres, the functional unit of muscle, and arranged in series. Muscle force is generated by the sarcomere when the head of the heavy chain myosin binds to actin chains via linking domains on the troponin complex. Hydrolysis of adenosine triphosphate facilitates the *power stroke* in the myosin and results in tension developing in the sarcomere. It is currently impossible to measure muscle forces exerted by an individual without the implantation of a tendon transducer which requires invasive surgery (Fukashiro et al., 1993).

Mathematical models of muscle have existed throughout most of the 20th century, but it wasn't until 1989 that Felix Zajac submitted a numerical model representation of the passive and active definitions of the musculotendon complex (Zajac, 1989) based on the Hill muscle model (Hill, 1938). The Hill-type model, or lumped parameter model, represents the muscle as a contractile (active) component in parallel with an elastic (passive) element and then in series with another elastic (passive) element representing the tendon (Figure 2.2). The Hill-type model is defined by normalized descriptions of the force-length and force-velocity relationships of muscle, as well as the force-length relationship of tendon. These curves along with empirical measurements taken of muscle fiber and tendon lengths, sarcomere lengths, physiological cross section area, and pennation angle (Arnold et al., 2010; Ward et al., 2009) allow for estimation of muscle forces and are commonly used in muscle modeling.

The contraction of the muscle is defined by optimal fiber length ($l_f^o$), tendon slack length ($l_t^s$), maximum muscle force ($F_M^o$), and pennation angle (α). The optimal fiber length ($l_f^o$) represents the length at which the muscle can generate maximum force ($F_M^o$), which was determined by the specific fiber tension multiplied by the cross-sectional area of the muscle. Muscle pennation affects the transmission of force through the aponeurosis and is likely tied in with the function and excursion of the muscle as well as the fiber composition. These three parameters have been measured empirically (Arnold et al., 2010; Ward et al., 2009), and are mostly agreed upon in the literature surrounding computational muscle modeling. However, the tendon slack length ($l_t^s$) is difficult to measure directly, though attempts have been made to measure (Hug et al., 2013) and compute values numerically (Manal and Buchanan, 2003). Commonly used whole body models scale these four parameters with the size of the model to maintain the same force-length relationships across all joint angles (Arnold et al., 2010; Delp et al., 2007). Musculotendon length, velocity, and activation coupled with these parameters ($l_f^o$, $l_t^s$, $F_M^o$, α) and the relationships describing force-length and force-velocity characteristics determine the force output developed by the muscle.

### 2.3.4. Muscle Force Estimation Strategies for Human Locomotion

The human body has more muscles than degrees of freedom. As an indeterminate system there are many possible solutions to resolve a given loading condition making muscle force estimation a non-trivial task. Several different strategies are used to estimate muscle forces required for human locomotion. A common strategy, and the one employed in Chapters 4 and 6, is inverse dynamics optimization (Tsirakos et al., 1997). This technique requires that kinematics of the body are known, as well as ground reaction forces and moments obtained from force platforms. Given this information, an inverse dynamics approach can be used in which reaction forces and moments are applied to the body at each time instant and resultant moments and forces are calculated at the joints. A performance criterion is then chosen to resolve the resultant moments at the joints by the application of muscle forces. Previous work has considered the minimization of activation (Li et al., 1999), muscle stress (Crowninshield and Brand, 1981), and fatigue (Dul et al., 1984) to converge on a solution. Validation of the optimization solution can be considered by comparing the prescribed model activations to electromyography recorded during *in vivo* experimental analysis. The inverse dynamics optimization technique is computationally efficient but limited in that it only considers one time point at a time without history dependence of muscle force predictions. This technique is also quite common in whole body musculoskeletal modeling as it does not require contact to be represented in the model.

Other techniques have been used to predict muscle forces. Dynamic optimization performs a forward integration on the equations of motion:

$$M(\boldsymbol{q})\ddot{\boldsymbol{q}} + C(\boldsymbol{q})\dot{\boldsymbol{q}}^2 + G(\boldsymbol{q}) + R(\boldsymbol{q})\boldsymbol{F}^{\boldsymbol{MT}} + E(\boldsymbol{q}, \dot{\boldsymbol{q}}) = \boldsymbol{0}$$

where M correspond to the mass matrix of the system; $\boldsymbol{q}, \dot{\boldsymbol{q}},$ and $\ddot{\boldsymbol{q}}$ correspond to the rotational position, velocity, and acceleration of each joint in the system; $C(\boldsymbol{q})\dot{\boldsymbol{q}}^2$ is a term representing Coriolis forces and torques; $G(\boldsymbol{q})$ represents gravity applied to segments;

$R(\boldsymbol{q})\boldsymbol{F^{MT}}$ is a term relating to the angular torque due to muscle forces; and $E(\boldsymbol{q}, \dot{\boldsymbol{q}})$ is a term relating to the interaction of the body with external forces (Pandy, 2001). This method does not require laboratory motion capture and force plate data, but instead a numerical representation of the objective function must be defined (Anderson and Pandy, 1999). The limitation of this method is the computational expense required to perform multiple iterations of optimization on the cost function while integrating the equations of motion. Optimal control solutions have presented a powerful alternative to optimization based solutions (Audu and Davy, 1985), and recent work using PID controllers to predict muscle forces while tracking joint kinematics has shown promising results (Fitzpatrick et al., 2014; Navacchia, 2016)

## 2.4. Joint Level Modeling

Computational modeling at the joint scale allows for an increased level of realism when compared to whole body musculoskeletal modeling. Active and passive structures that carry load through the joint, complex material representations, and three-dimensional representation of bone and soft tissue structures can all improve the fidelity of the joint representation. Rigid body dynamics software applications, such as OpenSim and Anybody, support contact based on the elastic foundation “bed of springs” theory (Fregly et al., 2003). When considering the knee, this limits the implementation of any deformable contact such as the wrapping and deformation of ligaments, cartilage, and menisci. Finite element analysis (FEA) has become a platform where highly detailed joint representations can be effectively represented. The software package used in the work described in this dissertation, Abaqus (SIMULIA, Providence, RI), has become a standard tool used for mechanical, thermodynamic, and fluid problem formulations. FEA is a numerical method which can be applied to boundary value problems by solving a series of partial differential equations. Rigid bodies are discretized into nodes and elements which can then be bounded by constraints and manipulated in response to load and motion. It was the strength of this numerical method, which made it so successful in mechanical engineering, that propelled its translation into skeletal biomechanics in 1972 (Brekelmans et al., 1972). The primary limitation of the finite element method is long computational run times. It is common for a simulation to take several hours using FEA, compared to a rigid body dynamics simulation which may take only a few minutes to complete. Furthermore, without references to the whole body it is difficult to determine boundary conditions that mimic *in vivo* conditions in joint level models. Despite these limitations, improvements in computational hardware and methods continue to drive forward the usability of FEA in computational biomechanics.

Development of a finite element joint model, specifically at the knee, requires careful consideration regarding the complexity of structural representations. As the complexity of the model and the structures included increases so does the computational expense. A key strength of musculoskeletal modeling in FEA is model modularity: the ability to simplify specific structures or material representations while maintaining high fidelity in those of greater importance. This can be seen in previous work which has modeled ligaments as three-dimensional structures with wrapping capability (Limbert et al., 2004; Shim et al., 2014), and by contrast as one-dimensional springs (Harris et al., 2016; Hume et al., 2018; Smith et al., 2015). Cartilage has been represented as fully deformable with isotropic

(Donahue et al., 2002) and biphasic poroviscoelastic non-linear (Mattei et al., 2014) material representations, and using a pressure over-closure relationship based on elastic foundation theory (Fitzpatrick et al., 2010; Harris et al., 2016). This work, despite vast differences in implementation of identical structures, was successful due to the careful consideration given to model complexity and scope of the research question. The same consideration to scope should is given to whole body musculoskeletal modeling and joint level finite element modeling to answer different research questions.

### 2.5. Musculoskeletal Modeling: A Sequential Approach

Whole body musculoskeletal and joint level models allow researchers access to different questions: “How does the body respond?” and “How does the joint respond?”. Logically, the next question is “How does the joint respond while the body is performing an activity”. To consider the simultaneous response at multiple modeling scales recent work has turned to a combined sequential approach to musculoskeletal modeling. In this approach loading conditions, muscle forces, and joint reaction forces and moments are obtained from a whole body musculoskeletal model and then applied to a high-fidelity model of the joint. The finite element joint model then estimates stresses and strains in ligaments, cartilage, and bone, returning detailed information to the researcher. This state of the art technique has been used to consider subject-specific knee mechanics in healthy (Adouni and Shirazi-Adl, 2014b; Shelburne et al., 2005) and implanted (Kim et al., 2009; Navacchia et al., 2016b) subject populations.

Limitations with the sequential modeling approach involve the disconnect developed between models at two different modeling scales. As discussed in section 2.3.1, whole body musculoskeletal models include simplified representations of the knee joint where motion is constrained to a 1 degree of freedom hinge (Anderson and Pandy, 2001a) or prescribed for secondary degrees of freedom as a function of flexion angle (Arnold et al., 2010; Delp et al., 1990; Rajagopal et al., 2016; Thelen and Anderson, 2006). Thus, the relative position of the bones with respect to one another does not change under any circumstance. Muscle forces are estimated while moment arms are held fixed, so individual muscles will always maintain the same efficacy at a given joint angle. When these loading conditions are applied to the complex knee representation with deformable joint definition the joint will deform according to the constraints of contact, ligament, and muscle. This will cause changes in muscle moment arms and consequently the efficacy of a muscle with prescribed loading conditions (Fiorentino, 2013; Hume et al., 2018; Lunnen et al., 1981; Navacchia et al., 2017). Simply put the model communication is unidirectional with no kinematic or kinetic feedback returned to the whole body musculoskeletal model. (Care must be taken when using the term 'deformable joint definition'. For this work, 'deformable joint representation' refers to a joint which allows translational DOF and does not constrain the joint kinematically or use prescribed joint motion as a function of knee flexion angle.) Performing muscle force estimations using a full body musculoskeletal model with complex knee geometry developed entirely in a finite element framework would combine muscle force estimation and deformable tissue strain analysis into a single framework. This technique would eliminate the disconnect observed in the sequential modeling approach and develop a more accurate musculoskeletal response. Recent work in single-framework musculoskeletal modeling has been promising. Halloran et al. (2010)

performed concurrent estimations of muscle force and tissue strain at the foot during gait. This planar representation of the lower extremity was successful in estimating tissue strain but took between 10 and 14 days to successfully run – 99.5% of which was due to the finite element simulation (Halloran et al., 2010). Adouni et al. (2012) performed joint level concurrent muscle force estimations and tissue strain analysis. Muscles had fixed orientation of lines of action relative to the bones and neglected elasticity and force-length properties of muscle. Computational runtime was not reported (Adouni et al., 2012). Line et al. (2010) performed concurrent estimations of muscle and joint contact forces during gait. The models used surrogate representations of contact and neglected the force-length properties of muscle. Run times were reported between 42 minutes and 32 hours (Lin et al., 2010).

## 2.6. Gaps and Opportunities

Single framework musculoskeletal simulation offers an untapped area of potential research growth, but progress needs to be made to increase usability. Opportunities for single framework musculoskeletal simulation involve the effective translation of laboratory data into finite element simulation. Specifically, this can be broken down into three distinct areas of work: “model personalization”, “modeling infrastructure”, and “computational efficiency”. OpenSim has been successful, arguably, due to its ease of use and open nature of the software and techniques which have been used by hundreds of universities around the globe. Improving upon these three facets of single framework musculoskeletal finite element simulation would be of great benefit to biomechanics research.

### 2.6.1. Model Personalization

Effective musculoskeletal modeling requires the scaling of model segment lengths, masses, and muscle strengths. Whole body models represented in OpenSim and AnyBody are scaled to the size of subjects using optical marker data obtained from the gait lab. Model segment scaling is performed by considering the length between two markers placed on a segment of a generically sized model to the length measured from a subject. The ratio of distances can then be used to scale the relative length, and other dimensions if necessary, of the musculoskeletal model segment and is repeated for all segments included in the model (Lund et al., 2015). This allows for accurate estimation of joint kinematics and application of ground reaction forces and moments. Whole body musculoskeletal finite element models are represented by millions of nodes and elements and are frequently assembled using single subject geometries. Presently there is no way to use marker data from the motion laboratory to directly scale a musculoskeletal finite element model.

Differences among individuals in muscle geometry and strength is seldom captured in whole body musculoskeletal modeling. As discussed in section 2.3.2, moment arms are difficult to measure *in vivo*, but joint strength information is easily obtained through maximum isometric strength testing on joint dynamometers. Determining the maximum isometric flexion or extension torque at joints of interest allows for generic scaling of muscle group strength which can lead to more realistic estimations of muscle forces and joint response (Myers et al., 2018).

### 2.6.2. Modeling Infrastructure

Improved modeling infrastructure is important to the usability and repeatability of single framework finite element musculoskeletal simulations. OpenSim allows users to scale musculoskeletal models and build simulations that estimate kinematics, joint kinetics, and muscle forces in a repeatable and efficient way. Currently there is no software package that allows for such control of building and running musculoskeletal simulations in FEA. A user-friendly computational framework which would offer techniques for model scaling, kinematics estimation, and muscle force estimation would significantly lower the entrance threshold to a currently complex and inconvenient modeling workflow. Finite element simulations are composed of inputs files representing bone, muscle, tendon, material properties, kinematics, and ground reaction forces. As an example, the multi-scale musculoskeletal finite element model described in chapters 3, 5, and 6 is composed of 200-300 input text files including more than 2,000,000 lines of syntax. Manipulating a model of this magnitude efficiently to allow for multi-subject simulation work is nearly impossible. Development of a computation framework to streamline this musculoskeletal workflow in FEA will not only increase the usability of musculoskeletal finite element modeling, but it will open the door to other standardized work flows in model modularity and personalization.

### 2.6.3. Computational Efficiency

Computational efficiency is a known limitation of FEA in musculoskeletal simulation. Muscle force estimations performed by rigid-body-based simulations such as OpenSim step sequentially through time, using the resultant activations from the previous time point as an initial guess to the optimization for the following increment. This approach is ineffective for computationally expensive musculoskeletal FEA as it would increase the runtime linearly by the number of time points to be optimized. Current computer architecture, in both workstation or cluster environments, has access to countless computer processing unit (CPU) cores. The desktop computer in most homes has between 4 and 8 CPU cores, which scales up to 16-32 cores in high end workstations and more than 100 cores in cluster computing environments. Implementing a method for effective parallelization to solve simultaneous solutions for kinematics or muscle force estimations at multiple time points would continue to drive improvements in scalability and efficiency of musculoskeletal FEA.

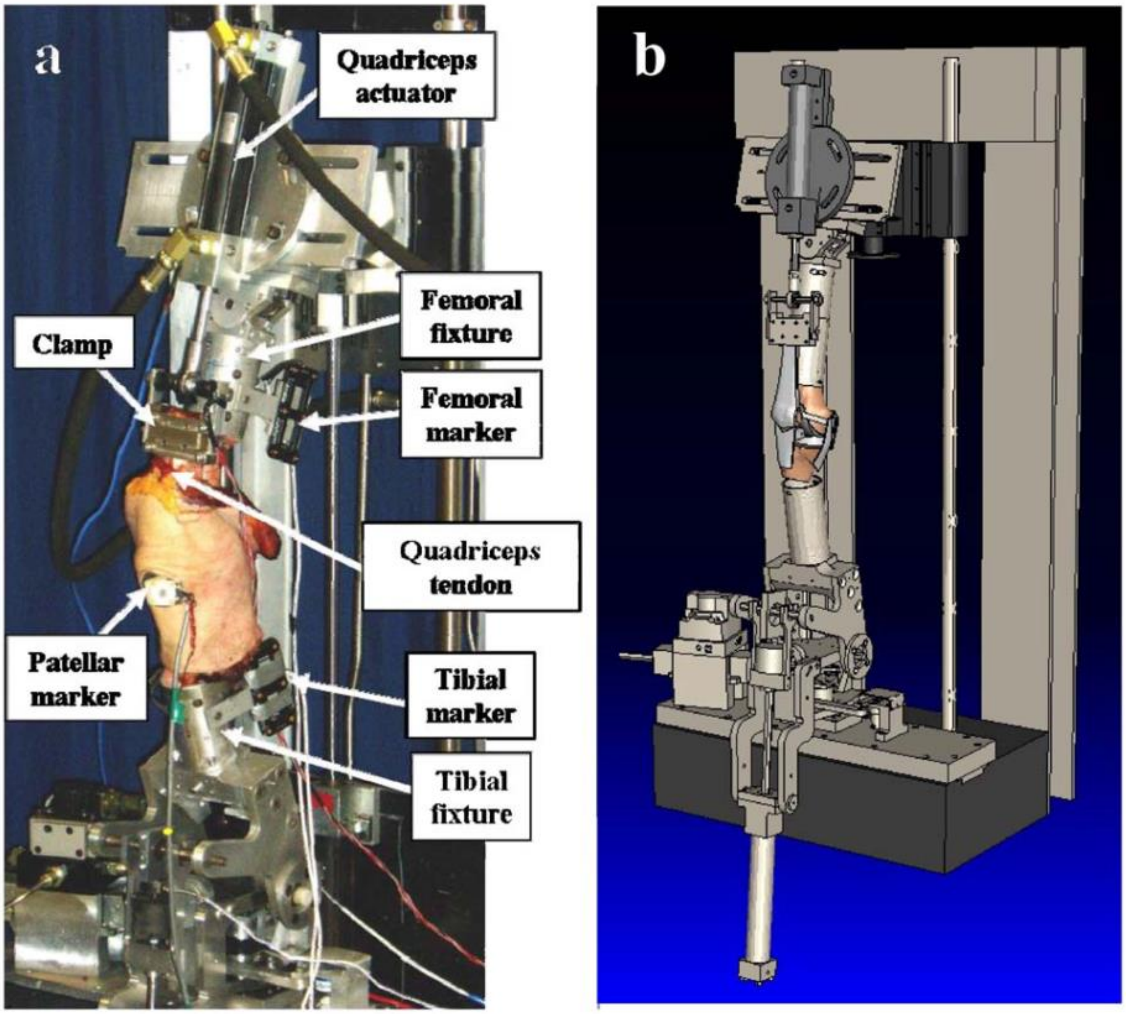

Figure 2.1 Computational representation of the Kansas Knee Simulator (KKS) used to validate predicted patellofemoral kinematics in a finite element representation of the knee [from Fig 1 (Baldwin et al., 2009)].

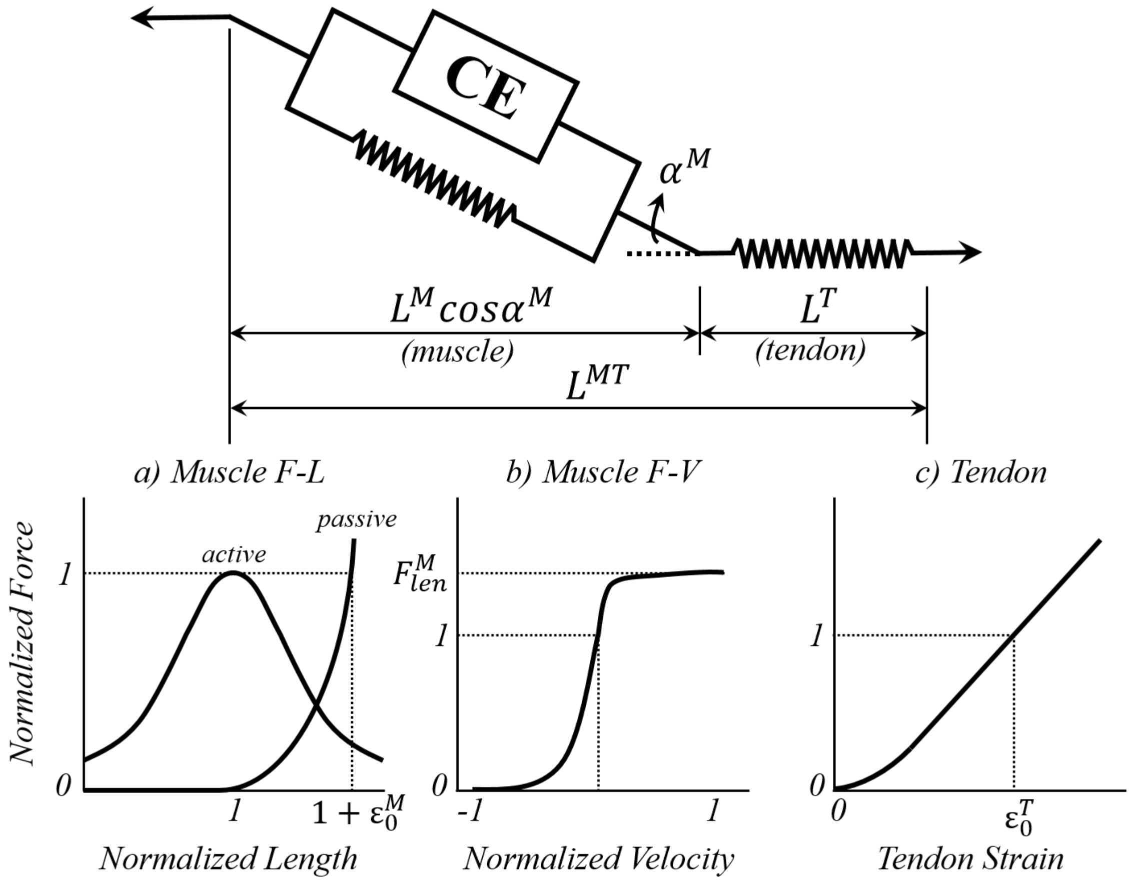

Figure 2.2 Representation of the lumped parameter model also known as a Hill-type model. The model is represented by a contractile element (active) in parallel with an elastic element (passive) representing the muscle, and then in series with another elastic element (passive) representing the tendon. The subfigures represent the normalized mathematical force-length and force-velocity representations of the muscle and force-length properties of tendon.

# CHAPTER 3. THE INTERACTION OF MUSCLE MOMENT ARM, KNEE LAXITY, AND TORQUE IN A MUTLI-SCALE MUSCULOSKELETAL MODEL OF THE LOWER LIMB

## 3.1. Abstract

**Introduction** Musculoskeletal modeling allows insight into the interaction of muscle force and knee joint kinematics that cannot be measured in the laboratory. However, musculoskeletal models of the lower extremity commonly use simplified representations of the knee that may limit analyses of the interaction between muscle forces and joint kinematics. The goal of this research was to demonstrate how muscle forces alter knee kinematics and consequently muscle moment arms and joint torque in a musculoskeletal model of the lower limb that includes a deformable representation of the knee. **Methods** Two musculoskeletal models of the lower limb including specimen-specific articular geometries and ligament deformability at the knee were built in a finite element framework and calibrated to match mean isometric torque data collected from 12 healthy subjects. Muscle moment arms were compared between simulations of passive knee flexion and maximum isometric knee extension and flexion. In addition, isometric torque results were compared with predictions using simplified knee models in which the deformability of the knee was removed and the kinematics at the joint were prescribed for all degrees of freedom. **Results** Peak isometric torque estimated with a deformable knee representation occurred between 45° and 60° in extension, and 45° in flexion. The maximum isometric flexion torques generated by the models with deformable ligaments were 14.6% and 17.9% larger than those generated by the models with prescribed kinematics; by contrast, the maximum isometric extension torques generated by the models were similar. The change in hamstrings moment arms during isometric flexion was greater than that of the quadriceps during isometric extension (a mean RMS difference of 9.8 mm compared to 2.9 mm, respectively). **Discussion** The large changes in the moment arms of the hamstrings, when activated in a model with deformable ligaments, resulted in changes to flexion torque. When simulating human motion, the inclusion of a deformable joint in a multi-scale musculoskeletal finite element model of the lower limb may preserve the realistic interaction of muscle force with knee kinematics and torque.

## 3.2. Introduction

Musculoskeletal modeling allows researchers to gain insight into the interaction of muscle and joint mechanics that cannot practically be measured in the laboratory. The current status quo in musculoskeletal modeling of the knee is to either constrain it to a hinge joint (Anderson and Pandy, 2001), or prescribe secondary degrees of freedom (DOF) as a function of flexion angle (Arnold et al., 2010; Delp et al., 1990; Rajagopal et al., 2016; Thelen and Anderson, 2006). Furthermore, the patellar mechanism is often represented as a pulley to simplify the transfer of force to the tibia (Arnold et al., 2010; Rajagopal et al., 2016). These simplified joint representations facilitate the calibration of muscle geometry parameters such as muscle moment arm, and calibration of muscle force-development parameters such as tendon slack length. In short, if the joint does not respond kinematically to loading, muscle geometry and parameters may be calibrated with only concern for knee flexion. However, simplified models of the knee limit the insight into changes in soft tissue constraint and contact mechanics due to injury or pathology.

The real knee responds to load in multiple DOF with well described soft tissue characteristics (Bendjaballah et al., 1997, 1998; Moglo and Shirazi-Adl, 2003), which interact with muscles forces, lines of action, and moment arms (Fiorentino, 2013; Lunnen et al., 1981; Navacchia et al., 2017). More recently, the inclusion of ligaments and articular surface interaction have made musculoskeletal models more realistic and better able to reveal the complex relation between knee loading and kinematics in healthy, pathologic, and repaired populations (Navacchia et al., 2016a; Smith et al., 2015, 2016). However, these models often require an iterative approach using separate models of muscle force as input to models with detailed knee mechanics (Adouni and Shirazi-Adl, 2014a; Navacchia et al., 2016b) creating a disconnect between joint and muscle force estimation. Translations and rotations at the TF and PF joints can alter muscle moment arms and thus muscular contribution to knee torque by making muscles more or less effective (Draganich et al., 1987; Pandy and Shelburne, 1998). In addition, changes in kinematics may change the length of the muscles, affecting their inherent ability to generate force at a given joint angle (Pandy and Shelburne, 1998).

The goal of this study was to demonstrate how muscle forces alter knee kinematics and consequently muscle moment arms and joint torque in a musculoskeletal model of the lower limb that includes a deformable model of the knee. Multi-scale musculoskeletal models were created incorporating two different models of the natural knee developed in prior work (Ali et al., 2016; Harris et al., 2016) with specimen-specific TF ligaments, patellar mechanisms, and articular geometry. The two models were used to show how muscle forces altered moment arms and joint torques during maximum isometric flexion and extension simulations. We hypothesized that maximal contraction of the extensor or flexor muscles would change the kinematics of the TF joint and alter (1) muscle moment arms, (2) muscle forces, and (3) maximum isometric torques.

## 3.3. Methods

### 3.3.1. Measurement of Extension and Flexion Torque

Twelve subjects (6M/6F, 70.29±13 kg, 176.91±10.87 cm, 29.3±4.4 years) provided informed consent to participate in a University of Denver IRB approved study. The subjects were seated with their hip angle at 60° and their knee joint line coincident with the axis of rotation of a Cybex dynamometer. Their shank was parallel to a lever arm attached just above the ankle with a Velcro pad (Cybex International, Medway MA) (Figure 3.1). Each subject performed a series of maximum isometric knee flexion and extension efforts at 15°, 45°, 60°, 75°, 90° and 115° of knee flexion. The subjects began with neutral ankle angle, though plantarflexion was not constrained by the experimental setup. Three flexion and three extension efforts were performed at each knee angle. The maximum knee flexor and extensor torques were recorded by the dynamometer for each subject. Mean and standard deviation were calculated across the subject sample at each joint angle.

### 3.3.2. Musculoskeletal Model of the Lower Extremity

Two finite element (FE) models of the lower limb including previously developed knee models of two healthy specimens were created in ABAQUS/Explicit (SIMULIA, Providence, RI) (Figure 3.2). The models of the lower limb were adapted from Delp et al. (2007) and consisted of four segments from pelvis to foot. Two unique specimen-specific models of the knee were utilized to quantify the sensitivity of the results to specimen-specific response (Model 1: “S1” and Model 2: “S2” from Harris et al. (2016)). The formulation of the knee models has been discussed previously (Ali et al., 2017, 2016; Harris et al., 2016) but will be summarized below. Bone and cartilage geometries were reconstructed from computed tomography (CT) and magnetic resonance imaging (MRI) (1 mm x 0.35 mm x 0.35 mm), respectively, using ScanIP (Synopsys, Exeter, UK). For all analyses, bones were meshed with rigid triangular shell elements (R3D3) while cartilage was meshed using hexahedral elements (C3D8). The cartilage mesh was formed by using a semi-automated morphing technique to match a hexahedral template to the surface geometry obtained from MRI (Baldwin et al., 2010). Contact between the cartilage surfaces was modeled with a pressure-overclosure relationship, based on elastic foundation theory, previously verified to accurately mimic deformable contact (Fitzpatrick et al., 2010). A coefficient of friction of 0.01 was applied at the articular cartilage surfaces (Unsworth et al., 1975).

Seven ligamentous structures crossing the TF joint were represented, including the anterior and posterior cruciate ligaments (ACL, PCL), medial and lateral collateral ligaments (MCL, LCL), popliteofibular ligament (PFL), anterolateral ligament (ALS), and medial and lateral representations of the posterior capsule (PCAP) (Harris et al., 2016). Ligaments were modeled as bundles of point-to-point tension-only non-linear springs and were calibrated to specimen-specific joint laxity envelopes (Harris et al., 2016).

### 3.3.3. Muscle Model Representation

Ten muscles spanning the knee were represented as Hill-type muscles comprised of a contractile element (active fiber force-length curve) in parallel with a passive elastic element (passive fiber force-length curve), then in series with an elastic tendon (Zajac, 1989). Specifically, rectus femoris (RF), vastus medialis (VM), vastus lateralis (VL), vastus intermedius (VI), semimembranosus (SM), semitendinosus (ST), biceps femoris short (BFS) and long (BFL) heads, medial gastrocnemius (MG), and lateral gastrocnemius (LG) were modeled (Figure 3.2). Muscles were divided into functional groups: the extensor group including RF, VM, VL, and VI, and the flexor group including SM, ST, BFS, and BFL. The line of action of the four quadriceps muscles was estimated from the Visible Human Project (Ackerman, 1998) as the centroid path of each muscle belly (Fitzpatrick et al., 2016). A multi-fiber representation was adopted to better represent force generation over the entire excursion of the joint (Ettema and Huijing, 1994; Herzog and ter Keurs, 1988). The VM and VL were divided into three and two fibers (Figure 3.2), respectively, according to a previously described cadaveric data set that grouped fibers based on function and sarcomere length (Klein Horsman et al., 2007). VI and RF were each represented by a single muscle fiber. Patellar tendon and quadriceps tendon were modeled as 2D fiber reinforced membrane elements (Baldwin et al., 2009) and were previously calibrated to match TF and PF experimental kinematics for the two specimens (Ali et al., 2017, 2016).

Patellar and quadriceps tendons wrapped over femoral bone and articular geometries (Figure 3.2). The tendons of the SM and ST wrapped over cylindrical analytical surfaces fit to the posterior aspect of the femoral condyles and posterior edge of the tibial plateau to more accurately follow the centroid of the muscle paths (Shelburne and Pandy, 1997). Insertion and origin for the four hamstrings and two gastrocnemii were derived from anatomical landmarks as reported by Delp (Delp et al., 2007). Muscle geometries were calibrated such that moment arms calculated during passive knee flexion closely matched values reported from in vitro experiments (Buford et al., 1997). This was done by perturbing the attachment sites and muscle wrapping surfaces within physiological bounds (Navacchia et al., 2016a). A modified force-length curve (Rajagopal et al., 2016) was adopted and optimal fiber lengths were adapted from Delp et al. (Delp et al., 2007) for the hamstrings and gastrocnemius muscles and Ward et al. (Ward et al., 2009) for the quadriceps. Optimal fiber length was scaled by the overall muscle length according to the optimal fiber and muscle length ratios reported by Ward et al. (2009). The tendon slack length and maximum isometric force of each muscle were adjusted manually (Anderson and Pandy, 2001; Buchanan et al., 2004; Zajac, 1989) until the resultant maximum isometric torque produced by the two models was within one standard deviation of the mean isometric extension and flexion profiles from the test subjects (Table 3.1).

### 3.3.4. Simulation Setup

Three activities were simulated in ABAQUS/Explicit using the two lower limb models: passive knee flexion, maximum isometric knee extension, and maximum isometric knee flexion. The activities were performed quasi-statically with the hip fixed at 60° and the knee placed at angles ranging from 5° to 120° of flexion. Gravity was ignored for all simulations. Activations were applied uniformly to muscle groups over the range of flexion angles for each simulated activity. Muscle moment arms were estimated as the partial derivative of knee torque with respect to force by applying small perturbations to muscle forces.

### 3.3.5. Passive Knee Flexion

Passive knee flexion was simulated by minimal activation of both flexor and extensor muscle groups (a=0.05) in the nine different positions. Aside from knee flexion angle, kinematics at the knee were unconstrained and determined based on the interaction of muscle, contact, and ligament restraint. The objective of the passive knee flexion simulation was to determine passive joint kinematics and muscle moment arms at discrete flexion angles for comparison to maximum isometric simulations.

### 3.3.6. Maximum Isometric Flexion-Extension (Deformable Joint Representation)

Maximum isometric flexion and extension were simulated by activating the primary muscle group maximally (a=1.00) while the opposing muscle group remained at minimal levels (a=0.05). The gastrocnemius muscles remained at 5% activation for isometric extension and 30% activation during isometric flexion to reflect the moderate level of gastrocnemius electromyography shown during maximum isometric knee flexion (Gravel et al., 1987). Like the setup of the dynamometer used in the subject measurements (Figure 3.1), a constraint was placed at the distal tibia to mimic the strap used to prevent knee flexion and extension during isometric contractions. The net torque applied by the muscles at the knee was calculated by cross multiplying the constraint force on the distal tibia with its moment arm with respect to the knee joint center. Internal-external rotation of the knee model was constrained kinematically to the rotations calculated during the passive flexion task. The objective of these simulations was to highlight the effect of a deformable joint on muscle moment arms and maximum isometric torque output at the knee.

### 3.3.7. Maximum Isometric Flexion-Extension (Kinematically Prescribed Joint Representation)

Maximum isometric flexion and extension simulations were repeated constraining knee kinematics to those obtained from the passive knee flexion. The objective of this simulation was to compare knee torque and moment arm results between musculoskeletal models with and without a deformable joint, given the commonality of prescribed kinematics in other models and studies.

## 3.4. Results

### 3.4.1. Experimental Isometric Extension and Flexion Torque

The mean peak extension torque for the 12 subjects (189.5 Nm) occurred at 75° of knee flexion (Figure 3.3). Peak isometric extension torque for individual subjects ranged from 91.0-244.0 Nm and occurred between 60°-90° knee flexion. The mean peak for isometric flexion torque (-94.2 Nm) occurred at 15°, corresponding to the most extended position of the knee collected during the study. Peak isometric flexion torque occurred between 15° and 45° of knee flexion for individual subjects and ranged from 52.8-151.0 Nm.

### 3.4.2. Model Isometric Extension and Flexion Torque

Simulations of isometric extension torque produced peak torques at 45° (156.4 Nm) and 60° (140.8 Nm) for Models 1 and 2, respectively (Figure 3.3). RMS differences between the simulations and the mean results from the experiments were 16.6 Nm and 19.4 Nm, respectively, over the flexion range. Simulation of isometric flexion torque produced peak torque at 45° for both models. RMS differences between the simulation and the mean isometric flexion results from the subjects were 16.0 Nm and 17.9 Nm for Models 1 and 2, respectively, over the flexion range.

### 3.4.3. Model Passive Knee Flexion Moment Arms

Quadriceps moment arms peaked between 15° and 30° of knee flexion (Figure 3.4). In general, moment arms were lowest at the highest knee flexion angle (i.e. 115°). The SM and ST moment arms exhibited minimal change through early flexion, peaked between 45° and 60° (Model 1: 38.6 mm, 47.5 mm, Model 2: 40.0 mm, 49.5 mm), and decreased into deep flexion. The BFL and BFS moment arms increased in early flexion, peaked at 75° (Model 1: 25.7 mm, 20.1 mm. Model 2: 34.0 mm, 24.7 mm), and then decreased during late flexion.

### 3.4.4. Model Maximum Isometric Flexion and Extension Moment Arms

Quadriceps moment arms during maximum isometric extension simulations exhibited minimal change from those calculated during passive knee flexion (Figure 3.4) with a mean RMS difference of 2.91 mm (Table 3.2), which is 6.7% of the mean peak. The location of peak moment arm did not change between simulated isometric extension and passive flexion: between 15° and 30° of knee flexion. Peak moment arm values for RF

(47.6 mm and 43.7 mm), VM (41.0 mm and 43.1 mm), VL (42.8 mm and 43.0 mm), and VI (48.7 mm and 47.3 mm) did not substantially change from passive knee flexion.

Hamstring moment arms changed substantially during maximum isometric flexion simulations (Figure 3.4) with a mean RMS difference equal to 9.80 mm which is 28.0% of the mean peak moment arm of the hamstrings, significantly higher than for the quadriceps ($p < 0.005$) (Table 3.2). The location of the peak hamstring moment arms remained consistent between 45° and 60°, with peak values for SM (51.8 mm and 54.4 mm), ST (59.7 mm and 63.1 mm), BFL (37.0 mm and 46.0 mm), and BFS (31.5 mm and 38.6 mm) that saw large increases throughout mid flexion (15°-90°) when compared to passive knee flexion.

### 3.4.5. Maximum Isometric Torque Differences (Deformable vs Kinematically Prescribed)

At 60° of knee flexion, maximum extensor torques in models with a deformable joint representation were 0.5% smaller (Model 1) and 0.4% larger (Model 2) than in models with kinematics prescribed to passive knee flexion (Figure 3.5**)**. RMS differences between these two cases were 2.6 Nm and 1.6 Nm for the two models. The muscle force output for the extensor muscles decreased by 1.4% and 1.0% with the inclusion of joint ligaments.

Maximum flexion torques were 14.6% (Model 1) and 17.9% (Model 2) larger than flexion torques without joint deformability, and the location of the maximum flexion torque shifted from 45° to 60° in both models. RMS differences between these two cases were 13.5 Nm and 15.3 Nm for the two models. The maximum flexion task saw 5.7%

and 4.8% decreases in flexor muscle force summed over all flexion angles when joint ligaments were included.

Changes in position of the tibia relative to the femur were seen during both isometric torque activities when compared to passive knee flexion. Relative tibial translation was calculated by subtracting the AP location obtained during the passive knee flexion from the AP location obtained during the maximum isometric activity (Figure 3.6). During the extension task, the tibia translated anteriorly between 5° and 30° of knee flexion and posteriorly from 30° to 120°. Peak changes in tibial AP location during maximum isometric extension were -10.8 mm and -8.8 mm and occurred at 120° of knee flexion. During the isometric flexion task, the tibia translated posteriorly for the entire range of joint angles. Peak changes during isometric flexion were -16.6mm and -15.5mm and occurred at 90° of knee flexion.

## 3.5. Discussion

The torque a muscle generates at the knee is partly due to its moment arm, which can be altered by changes in joint kinematics. In this study, we demonstrated the interaction between muscle force, joint kinematics, muscle moment arms, and joint torque in a musculoskeletal model of the lower limb with a deformable model of the knee. Maximum isometric knee extension and flexion were simulated to examine the effect of joint deformability on muscle moment arms and the torque produced at the knee. Only small changes were observed for quadriceps moment arms and extensor torque while moment arms for the hamstrings were altered substantially during maximum isometric simulations. Maximum isometric torque reflected the changes seen in hamstrings moment arms, with substantial changes to magnitude and peak location for isometric flexion torque. Changes in flexion torque were caused by changes in relative AP kinematics during the activity.

Experimental maximum isometric torque was similar to previously reported measurements in healthy adults (Anderson et al., 2007; Shelburne and Pandy, 1997) and simulation results were able to replicate both trend and magnitude of the experimental data. A notable difference between the in vivo and simulation results was the location of peak extensor torque. Mean subject data peaked at 75° (range: 60°-90°) while the simulation results peaked at 45° (Model 1) and 60° (Model 2). Prior musculoskeletal models of the lower limb have produced similar early peaks in maximum extensor moment (Arnold et al., 2010; Delp et al., 1990; Pandy and Shelburne, 1998). This might be explained by the fact that the Hill-type muscle model represents a muscle bundle using a single fiber, which does not replicate the wider force production range of whole muscle (Blemker and Delp, 2006, 2005; Herzog and ter Keurs, 1988). Even so, RMS errors between model and experiment were 16.6 Nm and 19.4 Nm for isometric extension torque and 16.4 Nm and 17.9 Nm for isometric flexion torque for Models 1 and 2, respectively. Simulation results remained within one standard deviation of experimental data. Furthermore, many subjects exhibited varying peak location in extensor moment (Figure 3.3) indicating substantial subject variability.

Our estimates of quadriceps moment arms were similar to prior results. Quadriceps moment arms during knee extension presented larger peak values in magnitude than those reported by Buford et al. (1997) but matched in trend (Figure 3.4). Effective quadriceps moment arms described by Grood et al. (1984) better agreed with the results of the present study. Previous modeling of the extensor mechanism also showed agreement with our results (Ali et al., 2016; Yamaguchi and Zajac, 1989).

Lateral hamstrings (BFL and BFS) moment arms increased as the knee reached full extension (Figure 3.4). This can be explained by the screw home mechanism - a phenomenon where the tibia rotates externally as it becomes fully extended, pivoting mostly about the medial condyle and moving the insertion of the biceps muscles further posterior to the knee, thus increasing their moment arms (Jagodzinski et al., 2003).

Contrary to our hypothesis, minimal change occurred in isometric extensor torque between models with prescribed kinematic motion and joint deformability. This is consistent with other findings that show similar extensor torques in knees with resected cruciate ligaments when compared with healthy knees (Draganich et al., 1987; Pandy and Shelburne, 1998). However, as hypothesized, a large increase in isometric flexion torque occurred at 30° in models with joint deformability: 22% and 21% for Models 1 and 2, respectively. Conflicting with our hypotheses, the summed muscle forces for the flexion group changed only 1.0% and 2.5% at that joint angle. The small changes in muscle forces, point to changes in moment arms as the primary contributor to changes in flexion torque. To our knowledge no prior studies have examined the change of hamstring moment arms resulting from the deformability of the knee during maximum isometric flexion.

The mechanism behind the changes in moment arm, and thus changes in joint torque, can be explained by the translation of the tibia that occurs due to muscle forces in models with deformable ligaments. Both maximum isometric flexion and extension produced a posterior translation of the tibia as the knee was flexed. The large posterior tibial translation during isometric flexion was caused by the increasing shear force of the hamstrings on the tibia as the knee flexed, peaking at 90° (Figure 3.4). The posterior translation of the tibia during isometric extension is explained by the natural femoral rollback that occurs in knee flexion causing the patellar tendon to be angled posteriorly relative to the long axis of the tibia, producing a posterior shear force acting on the tibia during quadriceps contraction (Shelburne and Pandy, 1997). The difference between isometric flexion and extension was that tibial AP translation had little impact on the patellar tendon moment arm and patellar mechanism, whereas posterior tibial translation produced large changes in the line of action of the hamstring muscles, the hamstring moment arms, and flexion torque (Markolf et al., 2004).

Notable differences were observed between the moment arms and maximum isometric torques of the two lower limb models used in the study. For example, peak isometric extensor torque occurred at 45° for Model 1 and 60° for Model 2. In addition, biceps femoris moment arms were greater in Model 2 than Model 1. However, subject-specific geometry played a small role in how moment arm and maximum isometric torque changed with and without inclusion of ligament response. Inclusion of ligaments elicited minimal change in torques during isometric extension, while in flexion the models exhibited similar increases (14.6% and 17.9%).

Limitations of the computational model concern model complexity and subject specificity. While the soft tissue deformation of each knee was calibrated based on a specimen-specific laxity response (Harris et al., 2016), the torque of the musculoskeletal model was calibrated to mean subject isometric torque. The variance of the measured isometric torque in our young healthy cohort indicates large inter-subject variability, which we did not capture in this study. Additionally, the model did not include a meniscus which has been shown to carry anterior-posterior load under various loading conditions (Markolf et al., 1976), particularly with the ACL absent. However, our simulations utilized models of the healthy knee that were calibrated to experimental data that incorporated the contribution of the meniscus to joint laxity.

There were also limitations to the analyses. While all five secondary DOF were unconstrained during passive knee flexion, the internal-external DOF was constrained in maximum isometric flexion and extension simulations to the profile from passive knee flexion. This limited out of plane rotations in the musculoskeletal simulation to the physiologic internal-external rotation of the specimens. To test the impact on our results, a sensitivity analysis was performed by prescribing an additional 5° of internal and external rotation during isometric flexion and extension simulations with the knee flexed to 60°: four simulations in total. The results showed less than 2.5% change in knee torques for each simulation. Further limitations included constant activation of the muscle groups during passive flexion, maximum isometric flexion, and extension simulations. Additionally, the gastrocnemii were assumed to remain at minimal activation levels (5%) for passive knee flexion and isometric extension, and 30% activation for isometric flexion despite the possibility of a more complex contribution to knee flexion torque. A further limitation was the lack of in vivo measurements to validate our findings of large changes in hamstring moment arms caused by posterior tibial translation during isometric flexion.

In conclusion the changes that occur to joint kinematics when the loading response of the knee is represented may alter muscle moment arm and joint torque. Changes in maximum hamstring moment arms between 58% and 83% were observed during the isometric flexion simulations. Maximum moment arm changes in the quadriceps were more moderate during isometric extensions simulations (between 15% and 36%). The inclusion of a deformable joint model with calibrated ligament representation in a multi-scale musculoskeletal FE model may provide a more realistic representation of the interaction of muscle force with joint kinematics.

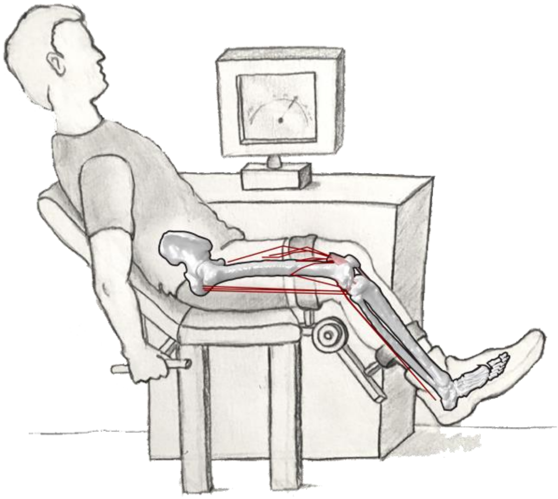

Figure 3.1 Experimental and simulation setup for maximum isometric flexion and extension tasks.

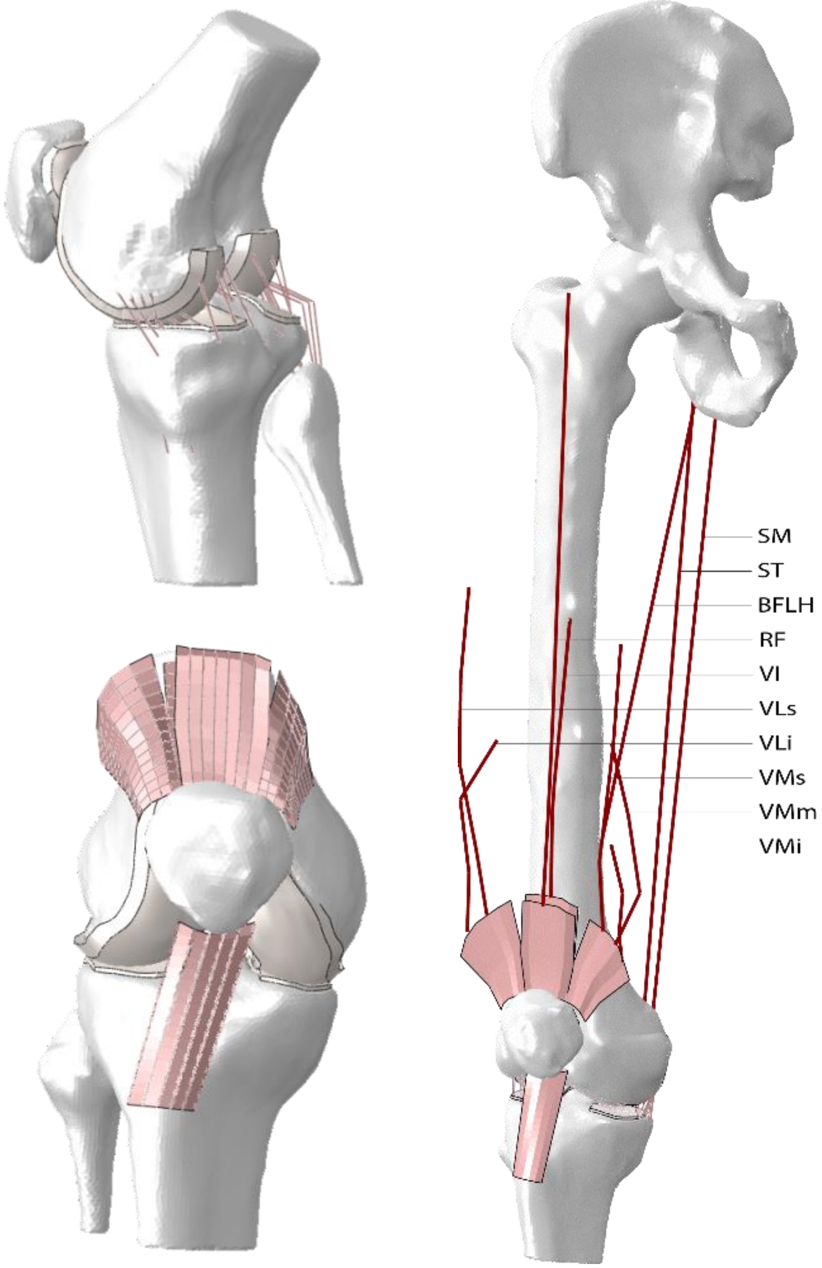

Figure 3.2 Specimen-specific knee model illustrating the ligament representation (top left)(Harris et al., 2016) and tendon wrapping (bottom left)(Ali et al., 2016). Musculoskeletal model highlighting semimembranosus (SM), semitendinosus (ST), biceps femoris long head (BFL), rectus femoris (RF), vastus intermedius (VI), and multi-fiber representations of vastus medialis (VMs, VMm, VMi) and vastus lateralis (VLs, VLi) (right). Gastrocnemius and biceps femoris short head geometry not shown.

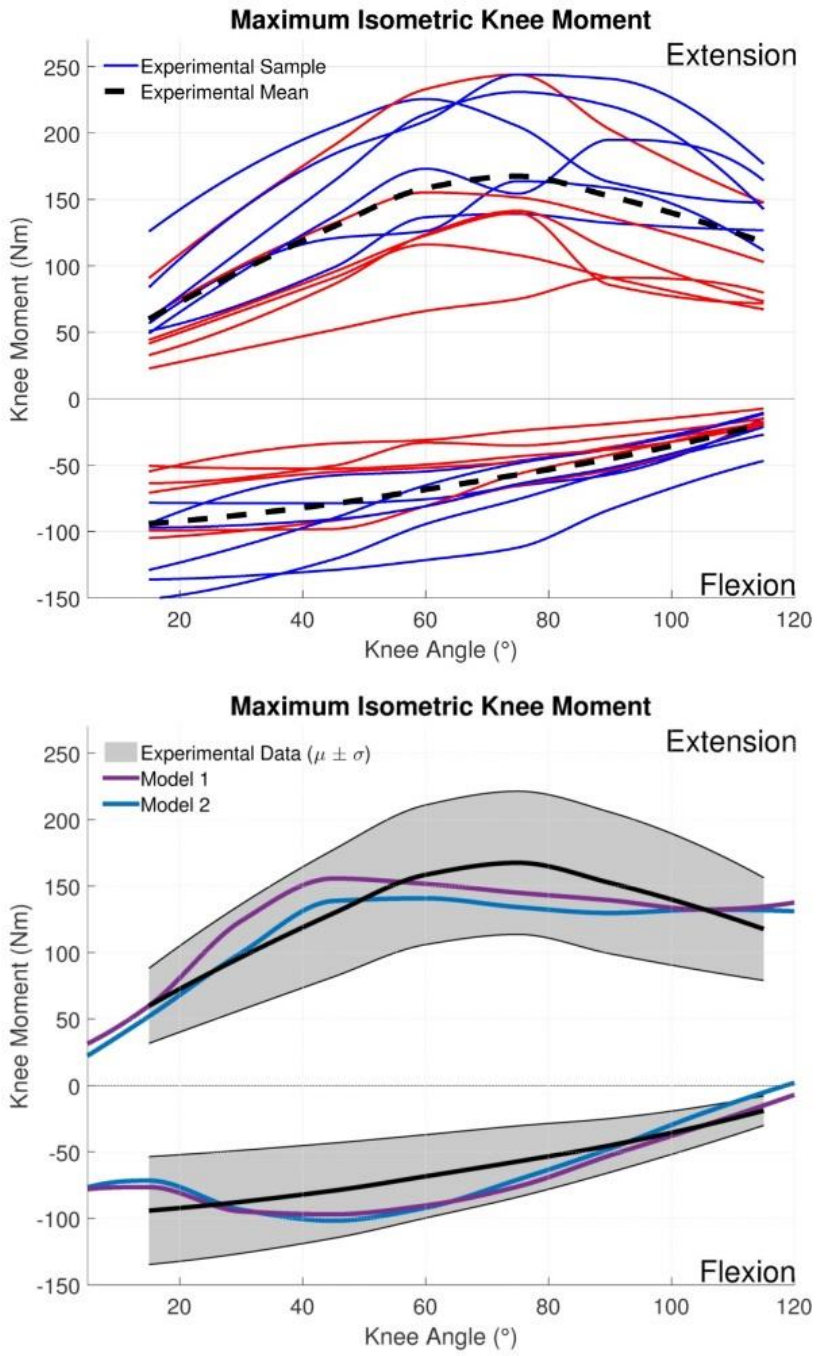

Figure 3.3 Maximum isometric flexion and extension torque of 12 subjects (red-female, blue-male) including mean curve (black) (top) and torque response of calibrated models during maximum isometric flexion and extension simulations compared to mean subject response (μ±σ) (bottom).

Table 3.1 Muscle parameters used for Hill-type muscle model after calibration to torque data. Parameters differing between models are reported as Model 1, Model 2. (*) denotes parameters which were calibrated to match model and mean subject knee torque data.

| **Muscle** | $L_m^o$ **(mm)** | $L_t^s$ **(mm)*** | $F_m^{max}$ **(N)*** | **θ (°)** |
|---|---|---|---|---|
| **RF** | 75.9 | 295.0 , 288.0 | 1265.8 | 12.0 |
| **VMi** | 126.8 | 27.0 | 436.5 | 12.6 |
| **VMm** | 96.8 | 120.0 | 896.2 | 12.6 |
| **VMs** | 96.8 | 174.0 , 169.0 | 931.9 | 12.6 |
| **VLi** | 129.4 | 90.0 | 1551.4 | 21.7 |
| **VLs** | 99.4 | 194.0 , 200.0 | 1294.5 | 21.7 |
| **VI** | 119.3 | 135.0 , 130.0 | 888.0 | 3.0 |
| **BFL** | 109.0 | 319.0 , 310.0 | 716.8 , 672.0 | 0.0 |
| **BFS** | 173 | 38.0 , 35.0 | 643.2 , 603.0 | 23.0 |
| **SM** | 105.0 | 323.0 , 314.0 | 982.4 , 921.0 | 15.0 |
| **ST** | 201.0 | 210.0 , 200.0 | 328.0 , 307.5 | 5.0 |
| **MG** | 90.0 | 353.0 , 373.0 | 1140.7 | 17.0 |
| **LG** | 64.0 | 377.0 , 390.0 | 500.2 | 22.0 |

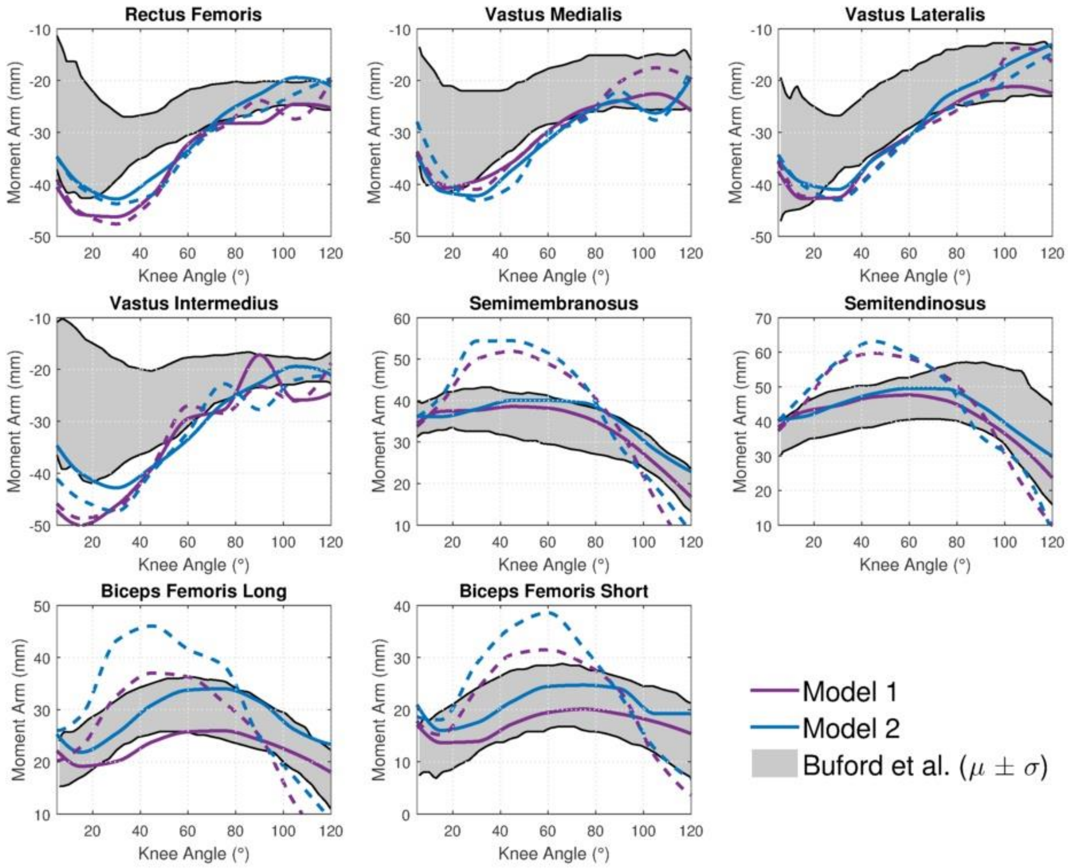

Figure 3.4 Comparison between post-calibration passive knee flexion moment arms (solid) and moment arms calculated during maximum isometric torque simulations (dashed) compared with experimental bounds (μ±σ) reported by Buford et al. (1997). Data from Buford et al. represent moment arms estimated from tendon excursion measurements in cadavers.

Table 3.2 Root mean squared difference between moment arms calculated for maximum isometric simulation and passive knee flexion simulation

| | Model 1 RMS (mm) | Model 2 RMS (mm) |
|---|---|---|
| RF | 2.64 | 2.07 |
| VM | 3.15 | 2.99 |
| VL | 3.47 | 2.12 |
| VI | 2.98 | 3.88 |
| SM | 9.25 | 10.43 |
| ST | 9.16 | 11.36 |
| BFL | 9.33 | 10.63 |
| BFS | 8.84 | 9.40 |

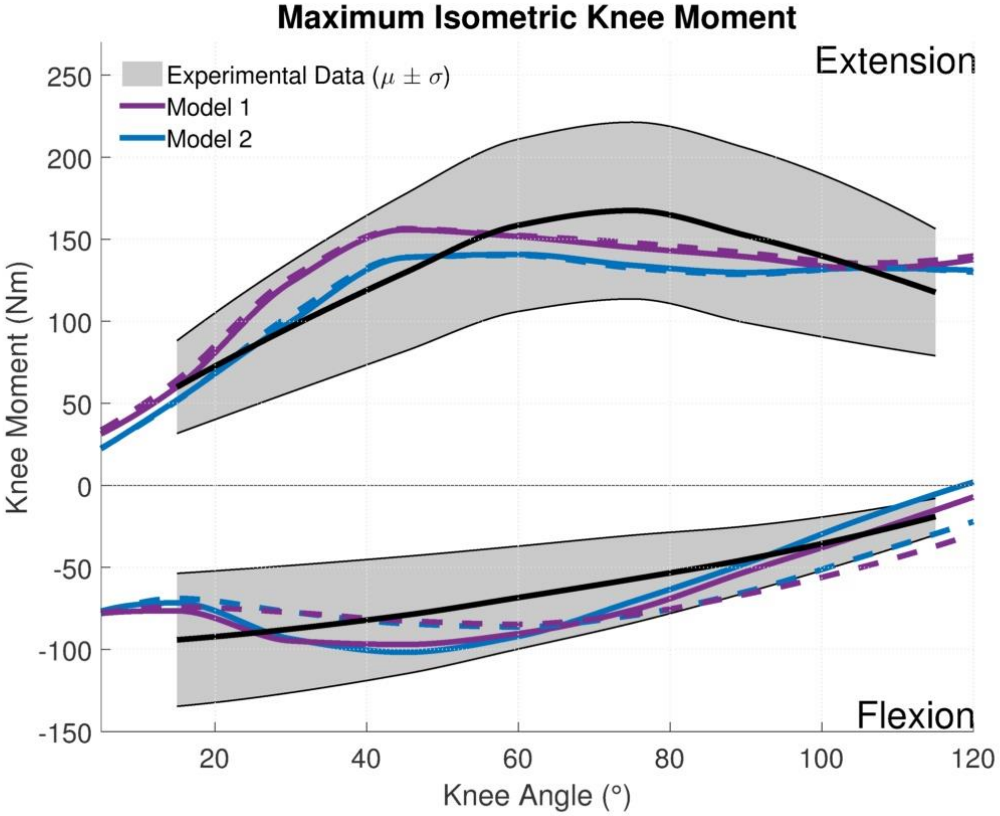

Figure 3.5 Changes in maximum isometric torque with (solid) and without (dashed) joint laxity representation.

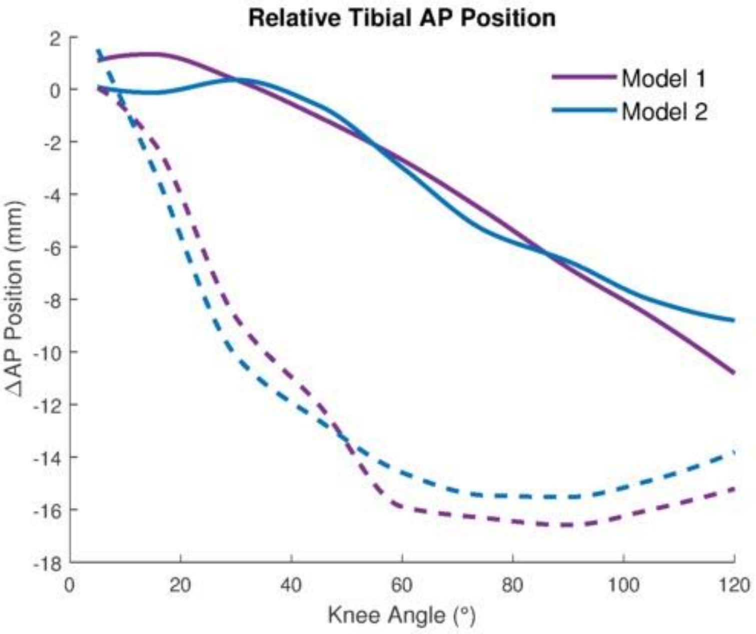

Figure 3.6 Relative anterior-posterior (AP) tibial translation (passive knee extension AP subtracted from maximum isometric activity AP) for isometric flexion (dashed) and extension (solid). A negative value indicates a posterior translation.

# CHAPTER 4. SIMULATION OF ACTIVITY USING A MULTISCALE FINITE ELEMENT MODEL OF THE LOWER LIMB

## 4.1. Abstract

A key strength of computational modeling is that it can provide estimates of muscle, ligament, and joint loads, stresses, and strains through non-invasive means. However, simulations that can predict the forces in the muscles during activity while maintaining sufficient complexity to realistically represent the muscles and joint structures can be computationally challenging. For this reason, the current state of the art is to apply separate rigid-body dynamic and finite-element (FE) analyses in series. However, the use of two or more disconnected models often fails to capture key interactions between the joint-level and whole-body scales. The objective of the current study was to create a multi-scale FE model of the human lower extremity that combines optimization, dynamic muscle modeling, and structural FE analysis in a single framework and to apply this framework to evaluate the mechanics of a healthy knee specimen. Two subject-specific FE models (Model 1, Model 2) of the lower extremity were developed in ABAQUS/Explicit including detailed representations of the muscles. Muscle forces, knee joint loading, and articular contact were calculated for two activities using an inverse dynamics approach and static optimization. Quadriceps muscle forces peaked at the onset of chair rise (2174 N, 1962 N)

and in early stance phase (510 N, 525 N), while gait saw peak forces in the hamstrings (851 N, 868 N) in midstance. Joint forces were similar in magnitude to available telemetric patient data. This study demonstrates the feasibility of detailed quasi-static, muscle-driven simulations in an FE framework. These models can be used as tools in comparative evaluation of implant designs on joint mechanics and assessment of muscle performance in physical therapy strategies.

## 4.2. Introduction

Musculoskeletal modeling allows researchers to gain insight into the interaction of muscle and joint mechanics that cannot practically be measured in the laboratory (Fernandez et al. 2011; Shelburne et al. 2011). A key challenge of the computational approach is determining the forces in the muscles during activity while maintaining sufficient complexity to realistically represent the tissues. Muscle forces contribute to joint load and have a strong influence on joint mechanics (Lenhart et al., 2015), which in turn partially determine muscle length, line-of-action, and moment arm (Fiorentino, 2013; Hume et al., 2018; Navacchia et al., 2017). This interaction between muscle forces, muscle moment arms, and joint torque at the knee is an important relationship that influences the biomechanics of the musculoskeletal system and can only be described in a model that incorporates both joint deformability and muscle mechanics (Hume et al., 2018; Shelburne and Pandy, 2002). Treatments that change or seek to restore healthy joint mechanics are rarely evaluated through a lens that includes the interaction of joint kinematics with muscle function.

The current state of the art is to apply separate rigid-body dynamic and finite-element (FE) analyses in series (Adouni and Shirazi-Adl, 2014a; Navacchia et al., 2016b). The series approach utilizes a rigid-body musculoskeletal model to calculate a muscle loading condition that is then applied to a detailed joint-level finite element (FE) model. Rigid body dynamic analyses (e.g. OpenSim, AnyBody) represent whole-body motions and may include large numbers of muscles. When used in conjunction with optimization, they can be used to predict forces in individual muscles required to perform an activity (Anderson and Pandy, 2001a; Besier et al., 2009; Smith et al., 2015). These analyses are computationally efficient, but have limited joint-level fidelity because bones are approximated as rigid bodies, joint representations are simplified (e.g. knee as a hinge joint or prescribing secondary kinematics) (Anderson and Pandy, 1999; Arnold et al., 2010), and muscle geometry is limited to wrapping of line segments over geometric primitives such as cylinders. The output of these rigid body simulations can then be applied to a detailed FE model focused on the joint of interest. FE analyses allows for representation of structures such as joints and ligaments in sufficient detail to allow for accurate solutions of the internal stresses and strains in structures including complex contact conditions and material representations such as anisotropic hyperelastic behavior (Fitzpatrick et al., 2010), with the tradeoff of longer computational times.

However, the use of two or more disconnected models in series inherits differences between models in joint representations, contact conditions, and application of the boundary conditions, and can fail to capture key interactions between the joint-level and whole-body scales. For example, it has been shown that knee contact forces contribute substantially to the resultant joint torques (Walter et al., 2015). Thus, these contributions would not be included in the inverse dynamics solutions of rigid body analyses ultimately affecting the muscle force predictions. Even so, studies which performed muscle force optimization directly in a finite element framework were often limited in complexity to avoid lengthy computational time (Adouni et al., 2012; Halloran et al., 2010, 2009; Lin et al., 2010). Notably, Lin et al. (2010) and Adouni et al. (2012) used a single model approach to obtain simultaneous muscle force and joint contact solutions for gait. However, these researchers modeled the muscles as ideal actuators, setting aside the elasticity of tendon and the force-length properties of muscle. As computational power continues to improve and becomes less limiting, effective parallelization of static optimization routines will become increasingly viable for musculoskeletal simulations in a finite element framework.

The objectives of this study were 1) to create a multi-scale musculoskeletal finite element (MSFE) model of the human lower extremity that combined muscle modeling and deformable FE analysis into a single model, and 2) to test whether static optimization can be practically applied to achieve simulation of human activity. Simultaneous analyses of muscle and joint function during physical activity can improve assessment of patient function and help to inform surgical and clinical practice.

## 4.3. Methods

### 4.3.1. Human Experiments

Laboratory measurements were collected from 2 healthy subjects during chair rise (Subject 1, age 60, 174 cm, 74.8 kg) and gait (Subject 2, age 59, 177.2 cm, 74.4 kg). The subjects provided informed consent to participate in a University of Denver IRB approved study. Each subject was screened for history of orthopedic injury to the lower extremity joints and excluded in concomitant conditions that limit function such as advanced arthritis of the hip. Kinematic, force-plate, and EMG data were collected for a battery of activities testing function during activities of daily living (Kefala et al., 2017). Two subjects and two activities were chosen to test the robustness of the proposed methodology. Ground reaction forces were measured with strain-gauged force platforms (Bertec Corp, Columbus, OH) embedded in the laboratory floor. Active EMG surface electrodes (Noraxon USA, Scottsdale, AZ) recorded activity of six dominant lower extremity muscles. Raw EMG data were rectified, filtered, and normalized to maximum isometric contractions, and used for validating the muscle activations predicted in the computer simulations. The 3D positions of passive retro-reflective markers mounted on the body were measured using an eight-camera motion-capture system (Vicon Motion Systems Inc., Centennial, CO). Joint angles were calculated from the marker positions using a rigid body modeling software package (OpenSim, Stanford, CA). A high-speed stereo radiography (HSSR) system was used in conjunction with motion capture to calculate six degree of freedom (DOF) kinematics for the dominant knee during each task (Kefala et al., 2017). Lower limb kinematics and ground reaction forces were used as input to the musculoskeletal simulations of gait and chair rise.

### 4.3.2. Musculoskeletal Model

Two MSFE models of the lower limb including knee models of healthy specimens were created for dynamic analyses in ABAQUS/Explicit (SIMULIA, Providence, RI)

(Figure 4.1). Two distinct knee models with specimen-specific articular geometry and calibrated laxity response were used to test the robustness of single-framework MSFE to changes in joint mechanics. The formulation for the model of the knees has been discussed previously (Ali et al., 2017, 2016; Harris et al., 2016; Hume et al., 2018) but will be summarized below. The model included specimen-specific bone and cartilage geometry which were segmented from CT and MRI, respectively. Contact was modeled with a pressure-overclosure relationship, based on elastic foundation theory, previously verified to accurately mimic deformable contact (Fitzpatrick et al., 2010). The model included a 1 DOF hinge-joint at the ankle, a 3 DOF ball-joint at the hip, and 6 DOF joints representing the tibiofemoral (TF) and patellofemoral (PF) joints.

TF and PF ligaments were calibrated to specimen specific laxity and flexion-extension tests (Ali et al., 2016; Harris et al., 2016). Seven ligamentous structures crossing the tibiofemoral joint were represented including the anterior and posterior cruciate ligaments (ACL, PCL), medial and lateral collateral ligaments (MCL, LCL), popliteofibular ligament (PFL), anterolateral ligament (ALS), and both medial and lateral representations of the posterior capsule (PCAP) (Harris et al., 2016). Ligaments were modeled as bundles of point-to-point tension-only non-linear springs and were calibrated to the joint laxity envelope of the same specimens whose geometry was used to build the knees ("S1" and "S2" in Harris et al.). Patellar and quadriceps tendon were modeled as 2D reinforced membrane elements permitted to wrap over cartilage and bone (Baldwin et al., 2009).

Twenty muscles spanning the hip, knee, and ankle were represented as 3-element Hill-type muscles. The muscles represented in the model were soleus, gastrocnemius (medialis and lateralis), tibialis anterior, vastus medialis (3 musculotendon units), vastus intermedius, vastus lateralis (2 units), rectus femoris, semimembranosus, semitendinosus, biceps femoris short and long head, gluteus maximus (3 units), iliacus, and psoas. Insertion and origin were derived initially from anatomical landmarks as reported by Delp et al. (2007). Muscle geometries were calibrated such that moment arms calculated during passive knee flexion closely matched values reported from *in vitro* experiments (Buford et al., 1997). Hill-type muscle model parameters were calibrated to match mean isometric flexion and extension torque curves recorded from healthy subjects (Hume et al., 2018).

### 4.3.3. Calculation of Muscle Forces in Chair Rise and Gait

Muscle activations and forces, and joint loads and contact pressures were calculated for the chair rise activity and during the stance phase of gait. Using a quasi-static inverse dynamics approach, muscle forces were estimated using static optimization at six body positions throughout the chair rise and seven body positions during gait. Static optimization was used because the number of muscles that span the knee exceeds the kinematic degrees of freedom. For activities that do not involve rapid movement, a quasi-static analysis is reasonable because inertial forces contribute little to tissue loading (Anderson and Pandy, 2003). The inputs to the static optimization were the joint angles of the hip, knee, and ankle joints, and the ground reaction forces and centers of pressure applied relative to the foot center of mass (COM). In the ABAQUS/Explicit simulation, the kinematics of the hip, knee, and ankle were prescribed and enforced by residual torques applied at those joints to maintain the required position. The remaining DOF of the tibiofemoral joint and the patellofemoral joint were unconstrained at the knee and determined based on the interaction between tibiofemoral and patellofemoral contact force, muscle force, and ligament restraint. The variables in the optimization design vector were the activation levels of the muscles. An initial guess for these values was obtained from the normalized subject EMG. The optimization found the muscle activations that reduced the residual flexion-extension torques to less than 1 N-m at the hip, knee, and ankle and minimized the sum of the cube of muscle stress (Crowninshield and Brand 1981).

The static optimization routine was implemented in MATLAB (Mathworks, Natick, MA) using the Nelder-Mead Simplex method, which combined ABAQUS/Explicit concurrent simulations of each activity's time points with muscle forces calculated using subroutines written in MATLAB and Python. The total number of time points included in the static optimization was 13 for the two activities. Separate optimizations were performed simultaneously at each of the 13 time-points in MATLAB using a custom computational framework that managed multithreading and parallel process control. During the optimization, each FE simulation used the current design vector of muscle activations coupled with the previous kinematic pose and corresponding muscle geometry to estimate muscle forces for each time point. Each optimization concluded when the improvements on the cost function became less than 0.1% for 20 iterations.

## 4.4. Results

Parallel simulations of chair rise and gait required 60 hours using a desktop workstation with 16 Intel® Xeon® 3.50 GHz processors and 64.0 GB of memory. Each iteration of static optimization took approximately 6 minutes of computational time, therefore requiring a maximum of 600 iterations to complete all 13 time-points. Results reported for both models will be ordered as Model 1 (M1: "S1") and Model 2 (M2: "S2"), unless otherwise stated.

Activations predicted by the static optimization during chair rise matched normalized subject EMG in both trend and magnitude (Figure 4.2) with no notable differences between models M1 and M2. Muscle forces for the quadriceps, echoing the model activations and subject EMG, peaked at the beginning of the chair rise (2174 N, 1962 N) and decreased throughout the activity (Figure 4.3**)**. The gluteus maximus exhibited a similar trend with large forces (1278 N, 1109 N) at the beginning that decreased throughout the activity. Iliopsoas and hamstrings produced very little force over the entirety of the activity. Gastrocnemii and soleus saw larger forces at the beginning (828 N, 919 N) and end (657 N, 799 N) of the chair rise. Normalized subject EMG, recorded from the medial gastrocnemius started at 4% activation that increased toward full extension. However, the estimated activation from the optimization fell between 5% and 20% activation but was similar in trend for both Model 1 and Model 2.

During the chair rise activity, total TF contact forces (calculated along the superior-inferior axis of the tibia) peaked early in the activity (337% BW, 341% BW) and then decreased as the subject progressed to stance. PF contact forces echoed the estimated muscle forces seen in quadriceps peaking at the beginning of chair rise (227% BW, 233% BW) and decreasing with the knee flexion angle through the activity. PCL, MCL, and PFL carried load throughout the chair rise, peaking in the beginning with 413 N and 575 N, 425

N and 327 N, and 368 N and 225 N of load, respectively, and then diminishing as knee flexion angle decreased.

During the gait activity, quadriceps forces peaked during contralateral toe off (CTO) (896 N, 870 N) and decreased through stance phase to contralateral heel strike (CHS) (Figure 4.4**)**. Normalized subject EMG peaked at 35% and 33% of stance for the medial and lateral vasti, respectively. Maximum hamstring forces occurred midway through single limb support (851 N, 868 N) and decreased through stance to CHS. Normalized subject EMG peaked for medial hamstrings at 46% of stance. Predicted activations for hamstrings matched normalized subject EMG with peaks occurring at 54% of stance for both models. Gastrocnemii and soleus saw minimal muscle contribution at CTO (181 N, 90 N), echoed by predicted model activations and subject EMG, which then increased throughout stance peaking at CHS (2171 N, 2281 N). Muscle forces from iliopsoas increased during stance with Model 1 forces ultimately increasing (520 N) at CHS and Model 2 forces decreasing at CHS (234N).

During the stance phase of gait, total TF contact forces increased throughout stance until CHS (402% BW, 397% BW). Both Model 1 and Model 2 started with a 50%/50% medial to lateral distribution of contact at CTO and deviated throughout the trial to 79%/21% and 89%/11% at CHS for the two models, respectively. The patella was in contact with the femur from CTO to mid-stance with maximum contact occurring at CTO (36% BW, 25% BW). The ACL, PCL, and MCL carried load during the second half of stance, with respective peaks of 293 N and 213 N, 122 N and 81 N, and 120 N and 163 N.

## 4.5. Discussion

A multi-scale musculoskeletal model of the lower extremity was created that combined muscle modeling and deformable FE analysis into a single model and was used in a static optimization to simultaneously solve for muscle forces and tibiofemoral and patellofemoral mechanics during a chair rise and the stance phase of gait. The musculoskeletal model combined representations of the bones, muscles, tendons, and ligaments into a single deformable model of the lower extremity. Two separate knee models with calibrated specimen-specific ligament representations were used to illuminate differences in the simulations due to geometry and soft tissue representation. The multi-scale musculoskeletal model was calibrated as reported in prior work (Hume et al., 2018) to match mean healthy maximum isometric flexion and extension torques recorded from test subjects. The model results showed that muscle forces can be calculated in a single framework without the use of serial models with inherently dissimilar geometry, loading conditions, and scales. Our solution was important because it demonstrated that a representation of muscle geometry and properties can be combined with a detailed and deformable computational model of the knee in a simulation to predict muscle forces, soft tissue, and joint mechanics simultaneously.

The computational time required to run single framework finite element solutions for chair rise and gait, constituted 13 parallel optimizations in total, was 60 hours per subject. Required computational time for the present study was shorter than recent finite element optimization-based solutions, which reported computational times between 32 hours and 4 weeks (Halloran et al., 2010, 2009; Lin et al., 2010), and often include planar models of the joints (Halloran et al., 2010, 2009) and surrogate representations of the contact mechanism (Halloran et al., 2009; Lin et al., 2010). While rigid body dynamics simulations allow for fast convergence of static optimization solutions (Smith et al., 2015; Thelen et al., 2014) and forward dynamics solutions (Guess et al., 2014), they are limited in their ability to model complex anisotropic material representations (Ali et al., 2017). The work presented here highlights the ability to perform 3-dimensional analyses of individuals performing complex activities to examine soft tissue stresses and strain in a single finite element framework using optimization-based muscle prediction.

Muscle forces predicted during the chair rise activity were similar in trend and magnitude to previous predictions. Shelburne and Pandy (2002) reported peak quadriceps forces at 80° of knee flexion of 2800 N compared to 2174/1962 N, for Model 1 and Model 2, respectively. Predicted hamstrings forces were nearly identical to those presented in this study with predicted peak forces of 500 N throughout the activity. Although the subject from the present study was slightly heavier, Shelburne and Pandy (2002) instructed their subject to rise "as quickly as possible" which might explain the discrepancy in quadriceps muscle forces. Joint loads predicted by the simulation were similar to previous joint load predictions and measurements made using telemetric implants. Peak tibiofemoral and patellofemoral contact forces were seen at 0% cycle: 336/341% BW and 227/233% BW respectively. Our results for TF contact fall within $\pm 2\sigma$ bounds representative of 7 subjects with telemetric implants performing a chair rise (Bergmann et al., 2014). Shelburne and Pandy (2002) reported similar results for TF contact, but with larger magnitude of PF contact at 80° knee flexion, 450% BWs compared to 227/233% BW. Contact forces in both

PF and TF decreased through the activity, as expected based on decreasing quadriceps muscle force profiles. Ligament forces predicted by the models were similar with previously published work. During the chair rise task, the PCL carried most of the shear load, with peak force of 413/575 N occurring at 80° of knee flexion. Shelburne and Pandy (2002) reported larger peak PCL force (650 N), with minimal MCL contribution (max: 50 N) and negligible ACL contribution. Our work indicated load sharing between the PCL and MCL (max: 327 N / 425 N) in deep flexion. This is likely explained by the internal-external DOF represented in the present model, compared to the planar representation from Shelburne and Pandy (2002).

Muscle forces compared well with previous predictions performed using static optimization during instrumented (Lin et al., 2010) and healthy gait (Adouni and Shirazi-Adl, 2014b; Anderson and Pandy, 2001b). Previously reported peak vasti forces fell between 600 and 1200 N compared to 510/525 N at CTO, and peak gastrocnemii forces between 300 and 900 N compared to 1000 N/1112 N at CHS. Previous results predicted 300 N (Anderson and Pandy, 2001b), between 0 and 600 N (Lin et al., 2010), and 225 N (Adouni and Shirazi-Adl, 2014b) of hamstring force, where our models predicted peak hamstring forces 851/868 N during mid stance (30% cycle), following the shape of normalized subject EMG. Models moderately overpredicted TF contact forces when compared to $\pm 2\sigma$ bounds representative of 6 subjects with telemetric implants during gait with 381/396% BW TF contact at CHS. The expected two-peak shape of the TF contact loading was not evident, likely attributed by the uncharacteristically large hamstrings loads predicted by the simulations. The patella only remained in contact through midstance, which can be explained by the hyper extension of the knee determined by the radiography-based kinematics. ACL forces played a larger role in gait than chair rise, with peak magnitudes occurring at CHS (293/205 N). Similar trends can be found in previous work, which showed increasing ACL loading profile as the knee was hyperextended, with a mean of 80 N in 2° of hyperextension (Jagodzinski et al., 2003).

Subject specific response to loading at the knee has a large effect on muscle forces, lines of action, and moment arms (Fiorentino, 2013; Hume et al., 2018; Lunnen et al., 1981; Navacchia et al., 2017). The differences in the optimization results from the two knee models demonstrated the importance of calculating muscle forces and joint mechanics simultaneously. The two knee models produced results which were similar in trend, but with different load sharing of the functional muscle groups. Specifically, the peak quadriceps force output was 11% larger during the chair rise task for Model 1. Furthermore, the movement of the COP on the patellar cartilage (Figure 3) was illustrative of differences in load sharing between the vastus medialis and vastus lateralis. At 0% cycle the %VM/%VL to total quadriceps force was 51%/21% and 60%/13% for the two models, respectively. This ratio of contribution changed throughout the activity concluding at 100% cycle with 38%/33% and 35%/40%. The change in contribution of different muscles at varying normalized fiber lengths highlights the ability of static optimization to resolve the muscle redundancy problem effectively and the sensitivity of muscle forces to variation in articular geometry (Smoger et al., 2015), ligament representation (Smith et al., 2015), and muscle moment arms that occurs in a deformable model of the joint (Hume et al., 2018). This sensitivity further highlights the importance of a single framework approach which includes rigid body kinematics and muscle force estimation with soft tissue modeling in a single framework.

The present study included several limitations. First, the kinematics and kinetics applied to the models came from an *in vivo* study whereas the models were derived form *in vitro* work which tuned their soft tissue response to cadaveric specimens. The *in vivo* subjects were similarly matched in size to the two lower extremity models, but differences in articular geometry, and soft tissue response remain. It is likely that the hyperextension measured by the HSSR during gait was subject specific and did not represent the kinematic behavior of the knee models. Nevertheless, the purpose of this study was to highlight the importance of a single framework approach on MSFE models with calibrated soft tissue response at the knee. Secondly, predictions of joint forces during most activities depend heavily on the muscle forces calculated for the activities (Shelburne et al., 2006). While no data exist to directly confirm the calculated values of the muscle forces obtained here for squatting, the predicted joint loads, and muscle activation patterns compared favorably with measurements of the same activities obtained *in vivo*. For example, the level of vastus activation and muscle force decreased as the subject moved through stance, while gastrocnemius muscle force increased through CHS (Figure 4.4). In addition, joint loads during chair rise were similar to those obtained using telemetric tibial implants. A final limitation is that the optimization took 60 hours of computational time on 13 cores for each subject. However, the current FE framework has the advantage of allowing modular complexity in tissue definitions that can dramatically affect, increase or decrease, solution speeds. This capability allows solution refinement, specifically increasing the number and complexity of deformable tissues, as the simulation progresses. In addition, ever increasing numbers of processers and processer speeds will further enable practical use of deformable, multiscale musculoskeletal simulations.

In summary, a detailed multi-scale MSFE model with calibrated soft tissue response was used to perform simultaneous predictions of muscle forces, joint mechanics, and loading of structures using laboratory data from a subject as input. This study demonstrates the feasibility of predicting muscle forces in dynamic, muscle-driven simulations that maintain high-fidelity joint representation. This methodology can be used in clinically relevant evaluation of soft tissue changes that occur due to injury, pathology, or surgical intervention at the joint level scale while providing assessment of physical therapy strategies at muscle and whole-body scales.

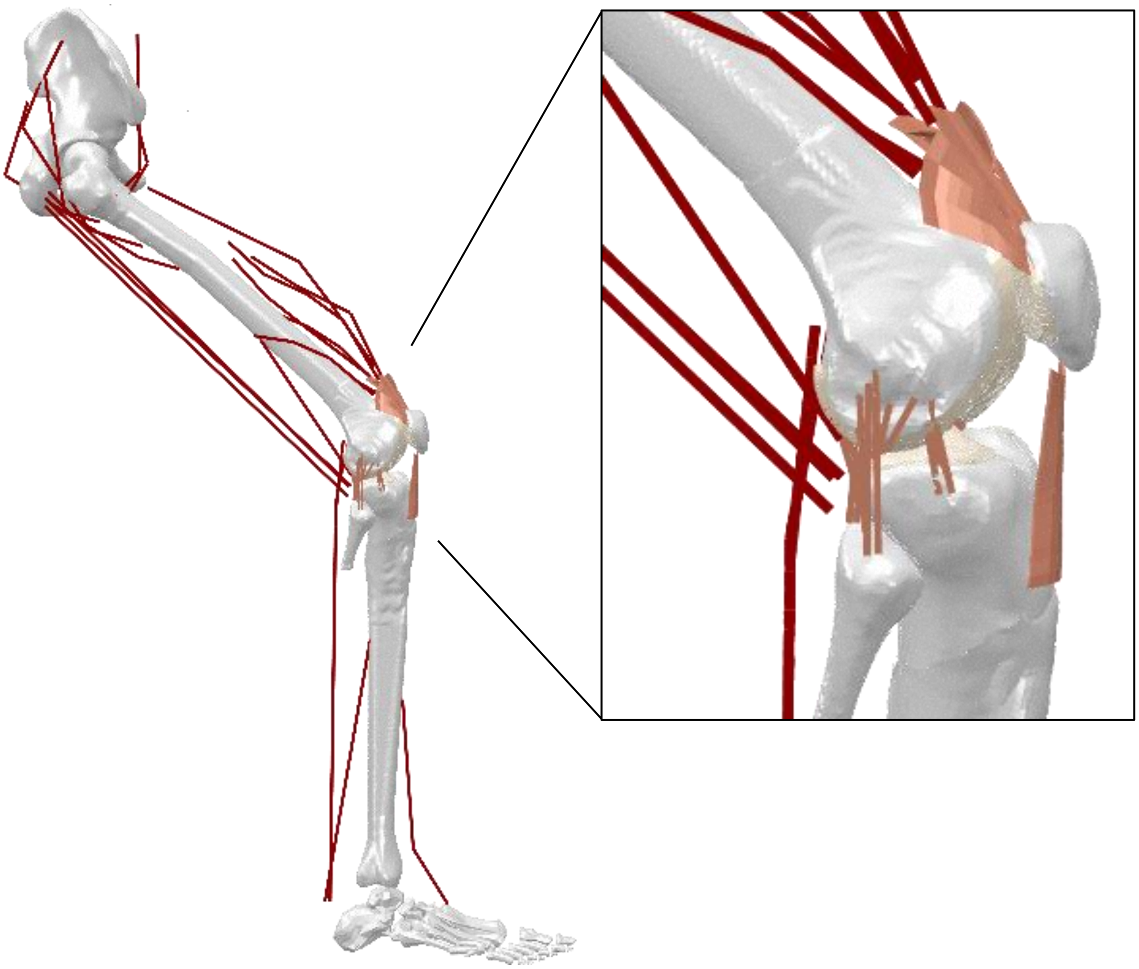

Figure 4.1 The lower limb musculoskeletal finite element model with two calibrated specimen specific knees ("S1" pictured). The knees included TF and PF soft tissue structures whose response was calibrated to in vitro experiments (Ali et al., 2016; Harris et al., 2016). The model 15 unique muscles comprised of 20 musculotendon fibers which span the lower limb previously calibrated to match mean healthy isometric knee flexion-extension torque results (Hume et al., 2018).

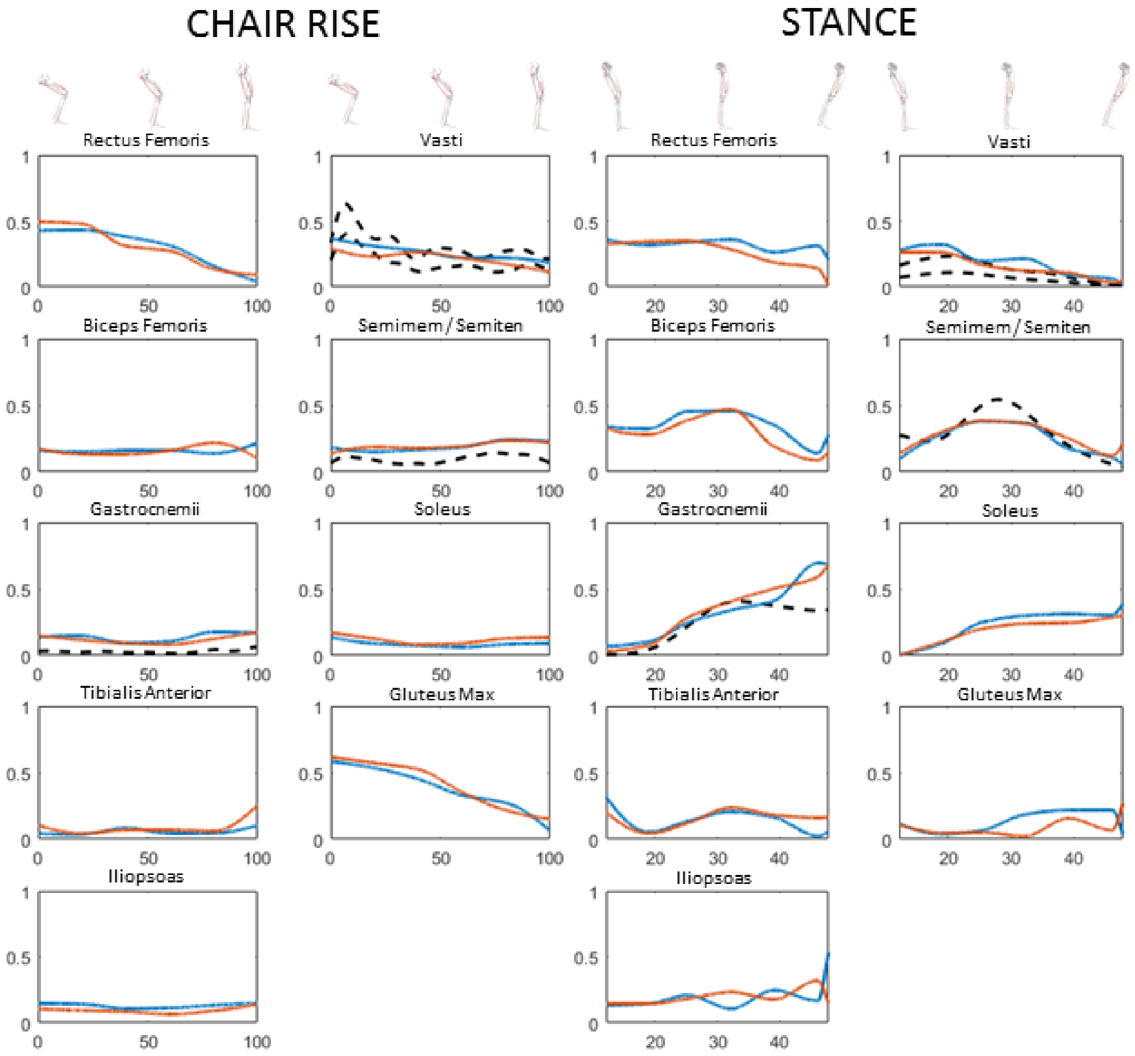

Figure 4.2 Predicted model activations for Model 1 (blue) and Model 2 (orange) and normalized subject EMG (black) plotted for chair rise (left) and the stance phase of gait (right).

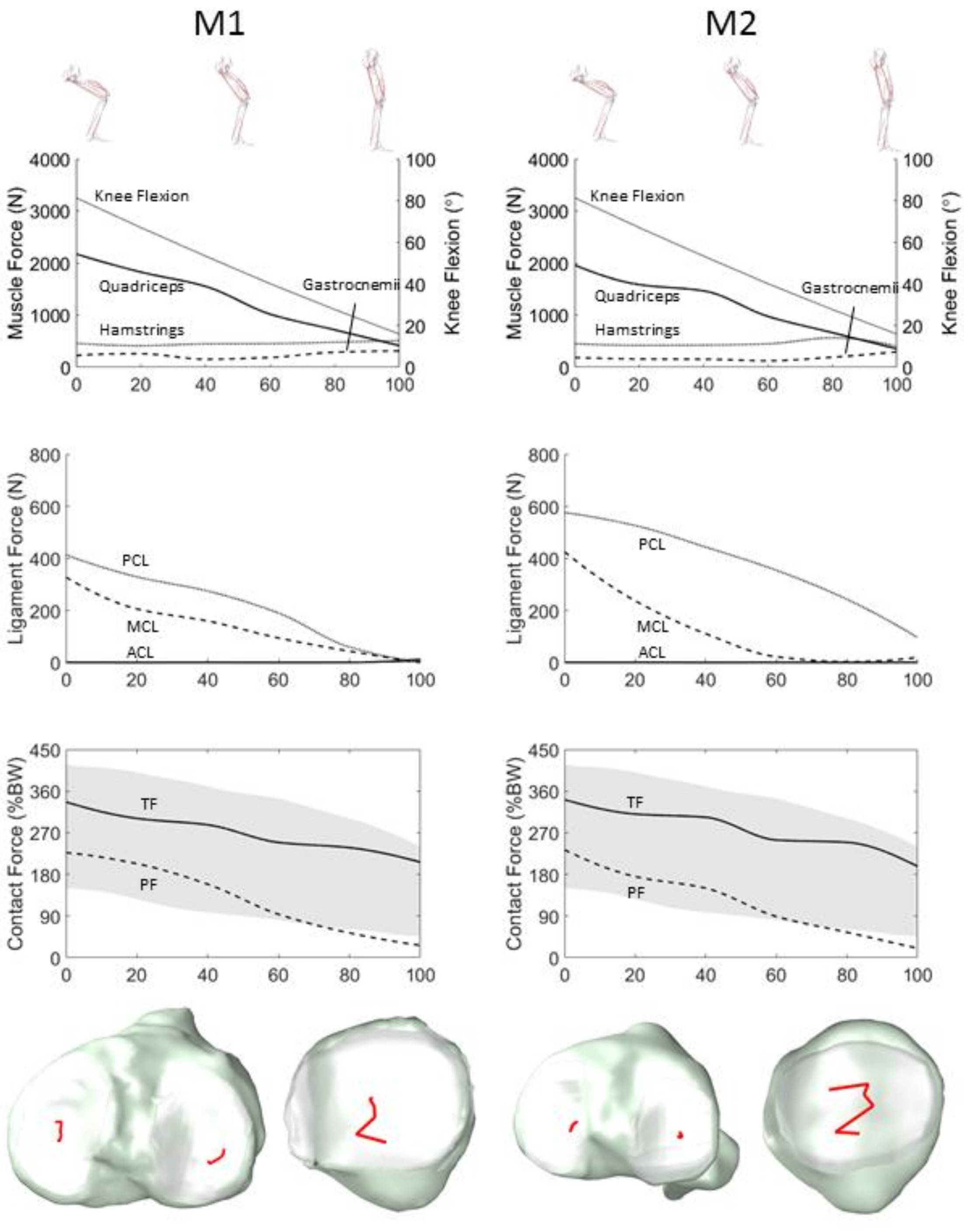

Figure 4.3 Forces prescribed by static optimization in muscle groups crossing the knee, forces carried by tibiofemoral ligaments, contact forces (TF/PF) plotted against telemetric implant data (Bergmann et al., 2014), and motion of the COP during the chair rise activity.

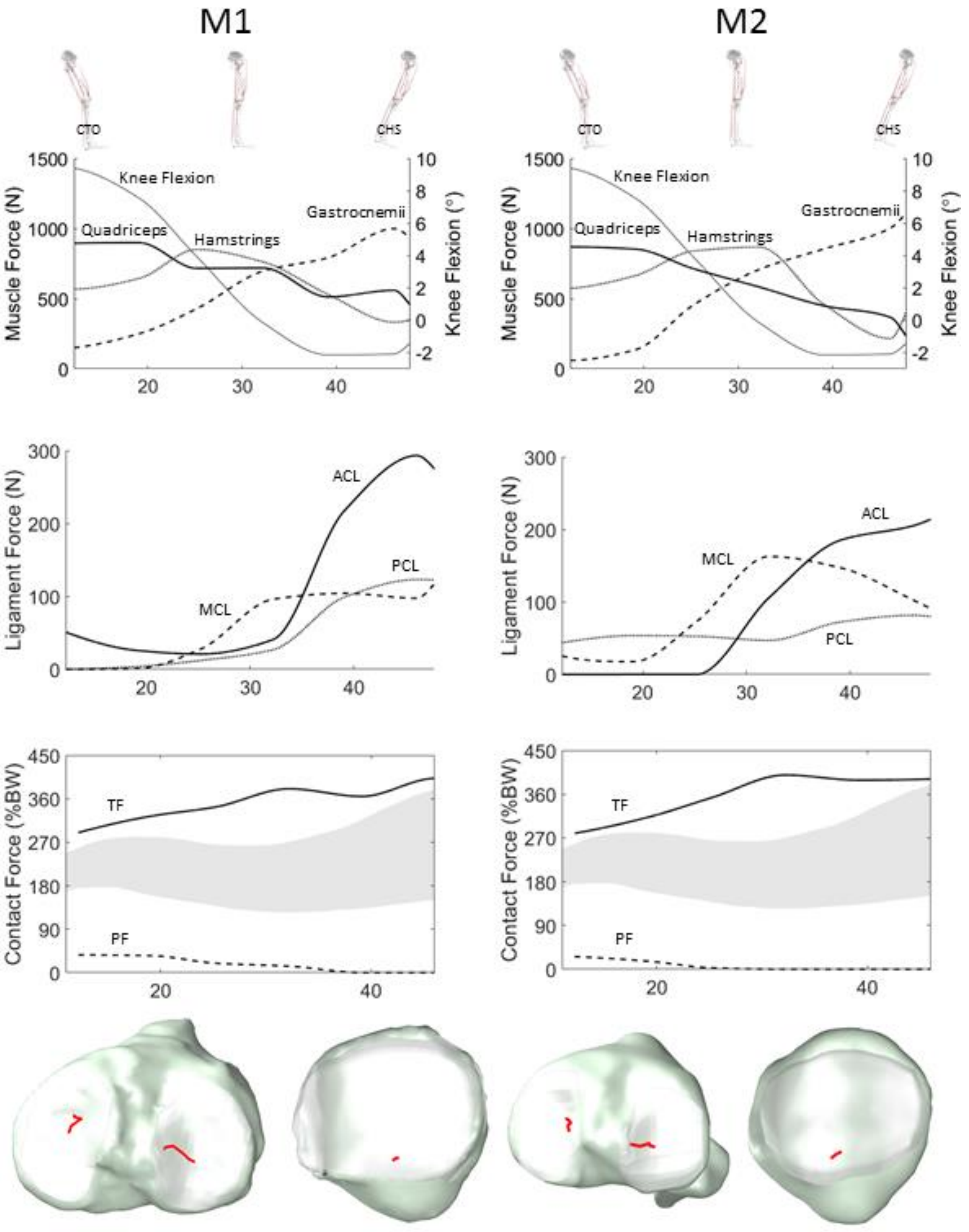

Figure 4.4 Forces prescribed by static optimization in muscle groups crossing the knee, forces carried by tibiofemoral ligaments, contact forces (TF/PF) plotted against telemetric implant data (Bergmann et al., 2014), and motion of the COP during the gait activity.

# CHAPTER 5. COMPARISON OF MARKER-BASED AND STEREO RADIOGRAPHY KNEE KINEMATICS IN ACTIVITIES OF DAILY LIVING

## 5.1. Abstract

Movement of the marker positions relative to the body segments obscures in vivo joint level motion. Alternatively, tracking bones from radiography images can provide precise motion of the bones at the knee but is impracticable for measurement of body segment motion. Consequently, researchers have combined marker-based knee flexion with kinematic splines to approximate the translations and rotations of the tibia relative to the femur. Yet, the accuracy of predicting six degree-of-freedom joint kinematics using kinematic splines has not been evaluated. The objectives of this study were to (1) compare knee kinematics measured with a marker-based motion capture system to kinematics acquired with high speed stereo radiography (HSSR) and describe the accuracy of marker-based motion to improve interpretation of results from these methods, and (2) use HSSR to define and evaluate a new set of knee joint kinematic splines based on the in vivo kinematics of a knee extension activity. Simultaneous measurements were recorded from eight healthy subjects using HSSR and marker-based motion capture. The marker positions were applied to three models of the lower extremity to calculate tibiofemoral kinematics and compared to kinematics acquired with HSSR. As demonstrated by normalized RMSE above 1.0, varus-valgus rotation (1.26), medial-lateral (1.26), anterior-posterior (2.03), and

superior-inferior translations (4.39) were not accurately measured. Using kinematic splines improved predictions in varus-valgus (0.81) rotation, and medial-lateral (0.73), anterior-posterior (0.69), and superior-inferior (0.49) translations. Using splines to predict tibiofemoral kinematics as a function knee flexion can lead to improved accuracy over marker-based motion capture alone, however this technique was limited in reproducing subject-specific kinematics.

## 5.2. Introduction

Marker-based motion capture is the established standard for the quantification of human movement. Video cameras are used to locate the position of markers placed on the body in a calibrated motion capture volume, and from these marker positions the movement of the body segments and their relative motions at the joints are calculated (Kadaba et al., 1990; Taylor et al., 1982). This technology has helped researchers and clinicians glean valuable information from a wide variety of patient populations and has an ongoing impact on clinical and scientific practice. The kinematics of the joints measured with marker-based motion capture assume no movement of markers relative to the bones. That is, the markers are assumed to be rigidly fixed to the body segments. However, movement of the overlying skin and soft tissues relative to the underlying bones introduces uncertainty in the marker positions relative to the body segments and obscures in vivo joint level motion (Benoit et al., 2006; Cappozzo et al., 1996; Li et al., 2012; Reinschmidt et al., 1997; Stagni et al., 2005). Estimations of this uncertainty typically fall between 10 mm and 30 mm of relative motion between the markers and underlying bone, although error of 42 mm has been reported at the distal thigh (Stagni et al., 2005). At the knee, this amount of uncertainty makes joint-level measurement challenging. In some degrees of freedom (DOF), the actual relative motion between bones at the knee occurs on a scale of a few millimeters or degrees (Anderst et al., 2009; Kefala et al., 2017; Li et al., 2004; Torry et al., 2011). These small joint motions are very difficult to measure with skin-marker-based tracking systems yet are of keen interest to many investigators for understanding healthy knee motion and the changes that accompany injury (Ali et al., 2017; Moglo and Shirazi-Adl, 2005) and repair (Clary et al., 2013; Heyse et al., 2017; Schwechter and Fitz, 2012).

Measurement of knee joint kinematics using dynamic radiography allows for direct analysis of joint motion with high accuracy. Dynamic radiography records a series of x-ray images of the bones of interest that are then used to reconstruct joint motion by matching the pose of the subject’s bones to the images (Anderst et al., 2009; Ivester et al., 2015; Kefala et al., 2017; Li et al., 2004; Torry et al., 2011). Accuracy for kinematic tracking of radiography images at the knee has been reported in static joint orientations between 0.15 mm - 0.20 mm and 0.2° - 0.4°, and for dynamic tracking 0.1° - 0.9° rotation with translational DOF peaking at 0.7 mm (Anderst et al., 2009; Ivester et al., 2015; Li et al., 2004; Miranda et al., 2011; Torry et al., 2011). However, radiography cannot achieve the large measurement volume that is frequently required for analysis of body segment motion common in musculoskeletal modeling. For this reason, some studies use marker-based motion capture with radiography of the knee to capture motion of the body simultaneously with precise measurement in regions of interest (Navacchia et al., 2017, 2016b; Zheng et al., 2014).

Combining marker-based motion capture and dynamic radiography for measurement of knee motion is currently impractical for most laboratories as dynamic radiography systems are not widely available and require time-consuming post-processing of image data.  To compensate for the lack of precise rotational and translational measurements, some researchers have assumed that motion of the tibia relative to the femur follows a predictable pattern as a function of knee flexion angle (Arnold et al., 2010; Delp et al., 1990), and substituted in vitro measurements of knee kinematics. In particular, Walker et al. (Walker et al., 1988) measured the motion of the femur and tibia using radiographs while flexing and extending the knees of 23 cadaveric specimens via a motor attached to the quadriceps tendon. The kinematic results were scaled to an average sized knee and fit with splines for varus-valgus (VV), internal-external (IE), anterior-posterior (AP), and superior-inferior (SI) DOF (medial-lateral (ML) was excluded) as a function of knee flexion-extension (FE)(Walker et al., 1988) and have been implemented in a commonly used biomechanical model (Arnold et al., 2010).  However, knee kinematics measured in vitro may differ significantly from those obtained under natural loading conditions in living humans, and post mortem changes in tissue properties may further influence the natural articulation that occurs at the knee in cadaveric specimens. Recent measurements of healthy kinematics using dynamic radiography bone tracking provide the opportunity to refine the use of kinematic splines in knee motion measurement.  An in vivo analysis of knee flexion-extension in healthy subjects using stereo radiography may yield improved kinematic polynomial splines for use in biomechanical modeling.

Two objectives were developed for this study. The first objective was to compare knee kinematics measured with a marker-based motion capture system to kinematics acquired with stereo radiography and describe the accuracy of marker-based motion to improve interpretation of results from these methods. The second objective was to use stereo radiography to define and evaluate a new set of knee joint kinematic splines based on the in vivo kinematics of a knee extension activity. Based on prior assessments (Li et al., 2012; Reinschmidt et al., 1997), we hypothesized that marker-based kinematics would accurately describe knee flexion-extension, and that the other five DOF of the knee would not be accurately measured. We also hypothesized that kinematic splines based on subject measurements would more accurately replicate subject knee motion as compared to prior splines based on in vitro measurements.

## 5.3. Methods

Eleven healthy subjects (5M/6F, 65.2±4.3 yr, 167.3±13.9 cm, 70.4±9.9 kg) were recruited to participate in the study. All subjects provided informed consent to a protocol approved by the Institutional Review Board of the University of Denver. Subjects were less than 30 kg/m$^2$ BMI and had no history of surgery or injury to the lower limb. Each subject performed a series of activities including seated knee extension, gait, step down, and a walking pivot turn. After familiarizing the subjects with each activity, a single dynamic radiography recording was taken for each activity.

Knee kinematics from high speed stereo radiography (HSSR) first reported by Kefala et al. (Kefala et al., 2017) were used here for comparison to marker-based kinematics of the same subjects. A previously described HSSR imaging system (Ivester et al., 2015) was used to capture knee kinematics during each activity. Briefly, the system consisted of two custom radiography sources positioned at a relative angle of 60°. High-speed cameras (Vision Research, Wayne, NJ) captured the images produced by the image intensifiers. A custom calibration cube with implanted tantalum beads was used to calibrate the imaging space between the two cameras. The data were synchronized via a step function sent from the high-speed cameras to the motion capture system allowing for a temporally aligned comparison between the two modalities. Bone tracking from the HSSR images was performed in Autoscoper (Brown University, RI) to obtain the pose of each bone throughout the different tasks. Knee kinematics were calculated from the bone transformations giving rotations and translations about the flexion axis of the femur using the ordered cardan sequence XYZ, defined by a positive rotation of the distal segment about the X axis representing flexion, a positive rotation about the Y axis representing varus rotation, and a positive rotation about the Z axis representing internal rotation.

6 DOF knee kinematics for the knee extension activity obtained from HSSR bone tracking were interpolated to one-degree increments of knee flexion and averaged for 8 of the 11 subjects who participated in the study. The averaged kinematics were then fit with polynomial equations to represent secondary DOF in a healthy population as a function of knee flexion. The order of the equations was chosen such that the coefficient of determination ($R^2$) was greater than 0.95 for each DOF. During the HSSR measurements, marker positions were recorded with an 8-camera motion capture system (Vicon Motion Systems Inc., Centennial, CO) at 100 Hz. Fifty retroreflective markers were placed on bony landmarks and used to define a whole-body marker set with increased emphasis on

lower limb segments (Figure 5.1). All marker trajectory data were filtered using a 4th order Butterworth filter with a cutoff frequency of 6 Hz. To determine knee kinematics during the activities, the marker positions recorded from the subjects were applied to three different models of the lower extremity.

First, the marker data were applied in Visual 3D (V3D) (C-motion, Germantown, MD) to a 7-segment lower extremity model with six DOF at the knee joint. The segments included in this model were pelvis, thighs, shanks, and feet. There were no constrained DOF at the knee and all 6 DOF were explicitly calculated using the relative translations and displacements of the tibia to the femur (6DOF Model). Kinematics were calculated in V3D using a least squares approximation between the markers fixed to the model and those placed on the subject. The pose of the femur and tibia was then used to calculate 6 DOF unconstrained joint kinematics at the knee.  Although it is not common practice to use marker data to estimate translations that occur at the knee, we chose to calculate them here for comparison to the subsequent methods that use splines to predict kinematics for these DOF.

Second, the marker data were applied to a previously defined 7-segment musculoskeletal model in OpenSim 3.2 (OpenSim, Stanford, CA)(Arnold et al., 2010; Delp et al., 1990). The three angular DOF (FE, VV, IE) were calculated explicitly using marker data (3DOF Model), while kinematic splines from Walker et al. (Walker et al., 1988) determined the translations at the knee (ML, AP, SI) as a function of flexion angle (Arnold et al., 2010; Gaffney et al., 2016). In addition to the knee, the hip and ankle joints were represented with 3 and 1 rotational DOF joints, respectively. Kinematics were calculated in OpenSim using a weighted least squares approximation to minimize the distance between model markers and subject markers, while also maintaining constrained or prescribed DOF at the joint (Lu and O’Connor, 1999).

Finally, the same 7-segment musculoskeletal model in OpenSim was used as above, except substituting kinematic splines derived from HSSR measurements (1DOFSP Model) to determine the five secondary DOF at the knee (VV, IE, ML, AP, SI) as a function of flexion angle.

All models were scaled according to each subject’s anthropometric measurements from static subject trials.  Specifically, each model was scaled using ratios of the distance between markers placed at bony landmarks on each subject, and virtual markers placed at corresponding locations on the model. The pelvis was scaled using relative distances between markers placed on the left and right anterior and posterior superior iliac spines. The thighs were scaled using relative distances between markers placed on the greater trochanter and lateral femoral epicondyle. The shanks were scaled using relative distances between markers placed on the medial and lateral femoral epicondyles, and the medial and lateral malleoli. Lastly, the feet were scaled using the relative distance between markers placed on the heel and the toe tip. Kinematics were calculated for four activities (seated knee extension, gait, step down, and a walking pivot turn) using the cardan sequence as defined above. The designated zero for all DOF in each of the three modeling applications was set at full knee extension determined from HSSR and established simultaneously at that same instant in the marker-based models to illustrate the relative differences in kinematics between the three models.

To evaluate the accuracy of the three different modeling strategies, data were compared in two ways. First, mean error of the marker-based methods was calculated relative to the HSSR kinematics during the knee extension activity. This was accomplished by interpolating the FE DOF in all modeling techniques to one-degree increments from 0° to 105° of knee flexion, allowing for all other DOF to be compared as a function of flexion angle. Second, root mean squared error (RMSE) values were calculated for each activity in each DOF and normalized by the total excursion of that DOF during the task. The goal of this metric, which has been used previously (Akbarshahi et al., 2010; Stagni et al., 2005), was to compare overall accuracy of different modeling techniques, in various DOF, over a variety of tasks. Normalized RMSE reveals errors that exceed the DOF being measure. For example, an error of 5° in VV might exceed the range of VV during walking. Accordingly, a normalized value of RMSE greater than 1.0 indicated a RMSE that exceeded the range of motion measured with HSSR during the activity and indicated the inability to accurately reproduce kinematics in that DOF. Finally, to evaluate the polynomial splines created from HSSR, the splines were compared with the results of Walker et al.(Walker et al., 1988) and used to predict secondary kinematics for subjects 9, 10, and 11, which were then compared to kinematics obtained from HSSR bone tracking for those subjects.

## 5.4. Results

The 6DOF Model predicted large amounts of translation in the AP and SI DOF (Figure 5.2) for the knee extension task, resulting in maximum mean AP error of 20.9 mm at 100° of knee flexion and maximum mean SI error of 19.7 mm at 105° of knee flexion. Maximum mean error in the ML DOF from full extension through 40° of knee flexion was

3.4 mm and then increased to 7.0 mm at 105° of knee flexion. There was better kinematic agreement between the rotational DOF measured using HSSR and the 6DOF Model. Maximum VV rotational error reached 5.9°, and maximum IE rotation error was 7.0°. Across activities, normalized RMSE values were less than 0.55 in FE for knee extension, gait, step down, and pivot (Table 5.1), and substantially greater for VV and IE rotation as well as ML, AP, and SI translation, with the exception of IE rotation during knee extension (0.33) and pivot (0.29).

The 3 DOF Model predicted lower mean errors than the 6 DOF model for the knee extension task, with maximum values reaching 5.6 mm at 105° in the AP DOF and 7.0 mm at 105° in the SI DOF (Figure 5.2). Error in ML increased from full extension through 40° of knee flexion where it peaked at 3.6 mm. Maximum mean VV error in the 3 DOF Model reached 5.9°, while that in IE rotation reached 4.7°. Like the IE error in the 6 DOF Model, there was a sharp increase in early flexion that plateaued at 20° with little change through the rest of knee flexion. Normalized RMSE values were less than 0.57 in FE for knee extension and step down with gait and pivot resulting in 0.71 and 0.82, respectively (Table 5.1). Normalized RMSE of VV and IE were greater than 1.0, with the exception of IE during knee extension and pivot. Kinematic splines represented in the 3 DOF model have RMSE values that were much lower than those calculated for the 6 DOF model. RMSE values were less than 1.0 in the ML DOF for all activities, less than 0.77 in the AP DOF except for the knee extension task (1.10), and less than 0.57 in the SI DOF.

The 1 DOFSP Model had maximum errors of 5.6 mm at 105° in the AP DOF, and 6.2 mm at 105° in the SI DOF during the knee extension task (Figure 5.2). Mean error in

AP translation was 1.35 mm from 0° to 80° of knee flexion then increased up to the maximum of 5.6 mm. Mean ML translational error was similar between the 3DOF and 1 DOFSP models with a maximum of 3.4 mm. The 1 DOFSP Model reported a maximum mean error in VV of 2.7°, while maximum IE rotational error was 4.2°. The 1 DOFSP Model had a slower increase in error when compared to the 3 DOF Model from 0° to 40° of knee flexion at which point the max error was 4.2° without much deviation through the remainder of the activity. Mean errors for VV and IE rotation were nearly identical to the 3 DOF Model. One notable difference was the lower mean error predicted in early flexion, between 5° and 20° of knee flexion, for the IE DOF in the 1 DOFSP Model. Normalized RMSE of VV and IE rotation were less than 1.0, except for IE rotation during gait and VV rotation during pivot (Table 5.1). Kinematic splines represented in the 1 DOFSP model have RMSE values that were much lower than those calculated for the 6 DOF model, with the exception of the IE DOF during the gait and pivot activities. Normalized RMSE values were less than 1.0 in all translational DOF for all activities. Kinematic splines created from the in vivo knee extension kinematics were similar in trend and magnitude to the in vitro results of Walker et al. (Walker et al., 1988) (Figure 5.3) but had notable differences that impacted the prediction of ML, AP, and SI DOF in the 1 DOFSP Model (the coefficients for these equations have been provided in Table 5.2).

Kinematic splines were used to predict kinematics in all 5 secondary DOF for three new subjects and compared with kinematics obtained via HSSR bone tracking (Figure 5.4). Mean normalized RMSE values for IE rotation, and AP and SI translations were less than 1.0 (0.39, 0.46, 0.57, respectively) (Table 5.3). Splines for VV and ML DOF failed to accurately represent the subject specific kinematics with mean normalized RMSE values exceeding 1.0 (1.17, 1.08). Normalized RMSE results in the IE DOF were smallest during the knee extension (0.17) and step down (0.31), and while gait (0.50) and pivot (0.59) fell below 1.0, the trend in the IE DOF for the pivot did not follow the HSSR kinematics (Figure 5.4).

## 5.5. Discussion

Marker-based motion capture is an essential tool for measurement of joint kinematics, however soft tissue motion introduces uncertainties into the motion of the underlying bones. The objectives of this work were to compare knee kinematics measured with a marker-based motion capture system to kinematics acquired with HSSR to describe the accuracy of marker-based motion to improve interpretation of results from these methods, and to use HSSR to define and evaluate a set of knee joint kinematic splines based on the in vivo kinematics of a knee extension activity to predict subject-specific knee kinematics. As hypothesized, knee flexion angle was accurately measured by marker-based modeling techniques (as illustrated by the normalized RMSE values in Tables 1 and 3), however all other DOF were not accurately measured except IE in limited cases. On average, using kinematic splines obtained from healthy knee extension kinematics led to an improvement in kinematic predictions when compared with the 3 DOF Model and the 6 DOF Model in VV, ML, AP, and SI DOF. Notably, the unconstrained 6 DOF Model had the lowest normalized RMSE in IE when compared to 1 DOFSP and 3 DOF Models. The kinematic splines implemented from HSSR produced mean errors nearly identical to splines created in prior work from in vitro measurements (Walker et al., 1988). The comparison to results from the test cohort of three subjects suggested that using splines to predict VV, IE, ML, AP, and SI DOF as a function of knee flexion can lead to improved accuracy over marker-based motion capture alone, but the technique may be limited in reproducing subject-specific kinematics.

The first objective compared knee kinematics measured with a marker-based motion capture system to kinematics acquired with HSSR and described the accuracy of marker-based motion. FE rotation was accurately measured in all tasks and models, however the kinematics predicted for the VV DOF in the 3DOF and 6DOF Models (those without implemented splines) showed poor accuracy when compared to HSSR-based kinematics. The normalized VV RMSE exceeded 1.0 in nearly all scenarios for the 6 DOF and 3 DOF Models. This outcome was supported by the results of prior research studies that also found little agreement between marker-based and precise methods of VV measurement in absolute error (Tsai et al., 2011) and normalized RMSE (Akbarshahi et al., 2010; Stagni et al., 2005). Given the consistent agreement of this outcome across studies, the continued prolific use of marker-based methods to measure VV rotation of the knee appears unwarranted. Our results showing inadequate accuracy of IE measurement in walking and step-down were mirrored by prior research as well (Akbarshahi et al., 2010; Benoit et al., 2006; Tsai et al., 2011). However, in contrast to some prior studies, kinematics measured by the 3 DOF and 6 DOF models in IE rotation followed the trend of the HSSR kinematics for the two tasks with larger excursions in the IE DOF, knee extension and pivot. A few prior researchers have found similar trends in IE accuracy (Stagni et al., 2005; Tsai et al., 2011). Even so, our IE rotational error increased abruptly between 0° and 25°

of flexion during the knee extension task, after which point the IE error remained constant (Figure 5.2). This error might be attributed to the inability of marker-based methods to adequately capture the screw-home mechanism, a well-documented kinematic phenomenon (Kim et al., 2015). Past 25° there was very little change in error, suggesting the ability of marker-based methods to capture large amounts of IE rotation in complex tasks.

The second objective used HSSR to define and evaluate a new set of knee joint kinematic splines based on the in vivo kinematics of the knee extension activity. The splines implemented in the 1 DOFSP Model improved mean normalized RMSE across all activities in all DOF relative to the marker-based kinematics, except for the IE DOF for the 6 DOF Model. However, accuracy of the VV DOF, though improved over marker-based techniques, remained poor for pivot and gait. These task specific differences can be explained by the small VV excursion during the gait and pivot tasks which inflates the normalized RMSE. For example, the 1 DOFSP Model accurately reproduced VV during the knee extension task (0.41) as this task had the greatest excursion of VV. Moreover, VV kinematics appeared to be highly subject dependent, with large differences in location of the kinematic envelope of each subject. Mean normalized RMSE were similar between the training and test cohorts (Table 1, Table 3), demonstrating that a sufficient number of subjects were used to create the in vivo kinematic splines. The high normalized RMSE results illustrated the challenge of matching all six DOF for a single subject (Table 3). Arguably, based on the differing results for different tasks, separate splines should be created for each activity. For example, kinematic splines derived for turning and cutting might be useful to improve the prediction of IE rotation in pivoting activities. While trends in IE rotation and AP and SI translations were moderately recreated by the kinematic splines, the kinematics were frequently not representative of the actual subject kinematics during unique tasks (e.g. IE rotation during pivot and SI translation during knee extension).

When compared to splines reported for cadaveric knee specimens (Walker et al., 1988), the in vivo kinematic splines were similar across all DOF with a few notable differences. IE splines from in vivo kinematics were similar to in vitro in trend but showed a more rapid initial increase to 7° internal rotation at 10° knee flexion, and maximum internal rotation of 17.6° compared to 15°. In addition, unlike Walker et al. (Walker et al., 1988), the spline representing the in vivo AP DOF predicted small translation in the subjects until 50° of flexion, beyond which AP translation increased to a maximum of 6.5 mm at 105°. These differences were most likely due to differences in loading conditions between the in vitro and in vivo experimental configurations. Most notably, active and passive forces were present in the hamstring muscles of the subjects, which were not applied in the in vitro experiment. Despite these differences, our hypothesis that kinematic splines based on subject measurements would more accurately produce knee motion as compared to splines based on in vitro measurements was not supported. The results of this study show almost identical RMSE calculated for the two spline methods. As supported by the variation of RMSE between the different tasks, we believe that the similarity in these results indicate that subject variability in the form of unique subject kinematics (Kefala et al., 2017) and the laxity of the joint (Harris et al., 2016) allow for changes between tasks that make it difficult to use one set of kinematic equations to accurately represent 6 DOF kinematics universally across tasks and subject populations. Even though normalized RMSE was improved with kinematic splines, challenges persist in predicting subject-specific knee motion as shown by differences between spline-based and HSSR-based subject-specific kinematics (Figure 5.4).

Limitations of the present study included the use of only two different modeling techniques with a single marker set. The 3 DOF and 6 DOF models used here were representative of conventional marker-based practice (Arnold et al., 2010; Gaffney et al., 2016; Zhang et al., 2015), even so other marker-based techniques may yield better results (Andriacchi et al., 1998). In addition, no attempt was made to compensate for the soft tissue artifact that most likely explains the errors in kinematics produced by marker-based methods (see Cereatti et al.(Cereatti et al., 2017) for a review). Using different subject populations and activities to produce kinematic splines might yield different results. Our subject cohort had BMI less than 30 kg/m$^2$; greater soft tissue artifact and subsequent kinematic errors might occur in subjects with higher BMI (Lerner et al., 2014). Furthermore, measurement of different activities might reveal different sensitivities in each DOF, as might occur during dynamic out-of-plane-movement, such as a cutting maneuver (Reinschmidt et al., 1997; Stagni et al., 2005).

In conclusion, knee kinematics measured with a marker-based motion capture system compared to kinematics acquired with HSSR revealed FE rotation to be accurately measured in all tasks and models, however the kinematics predicted for the VV DOF in the 3 DOF and 6 DOF Models showed poor accuracy when compared to HSSR-based kinematics. Similarly, IE measurement in walking and step-down had poor accuracy, however, IE rotation followed the trend of the HSSR kinematics for knee extension and pivot - tasks with larger excursions in the IE DOF. Implementing kinematic splines improved mean normalized RMSE across all activities, including joint translations (which were universally inaccurate with the 6 DOF Model). However, accuracy remained poor for pivot and gait. Using splines to predict VV, IE, ML, AP, and SI DOF as a function knee flexion led to improved accuracy over marker-based motion capture alone, yet the accuracy of in vivo kinematic splines was sufficient only in the IE, AP, and SI DOF, with limitations in reproducing subject-specific kinematics.

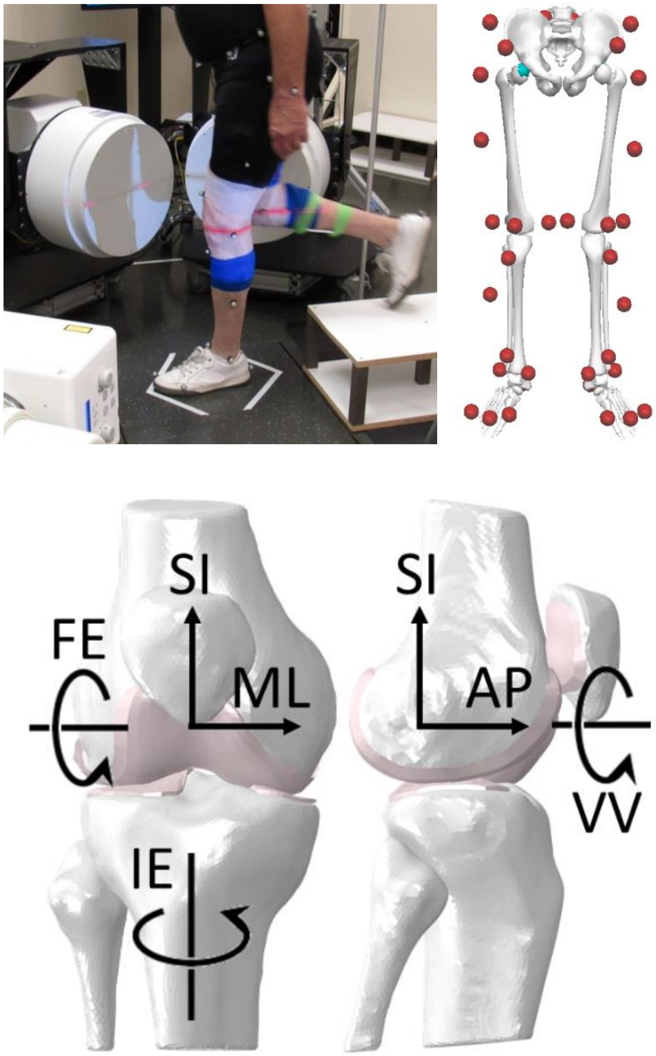

Figure 5.1 (top-left) Simultaneous biplane radiography and optical motion capture highlighting lower extremity marker set. (top-right) Experimental marker set. (bottom) Coordinate system used for resolution of knee kinematics.

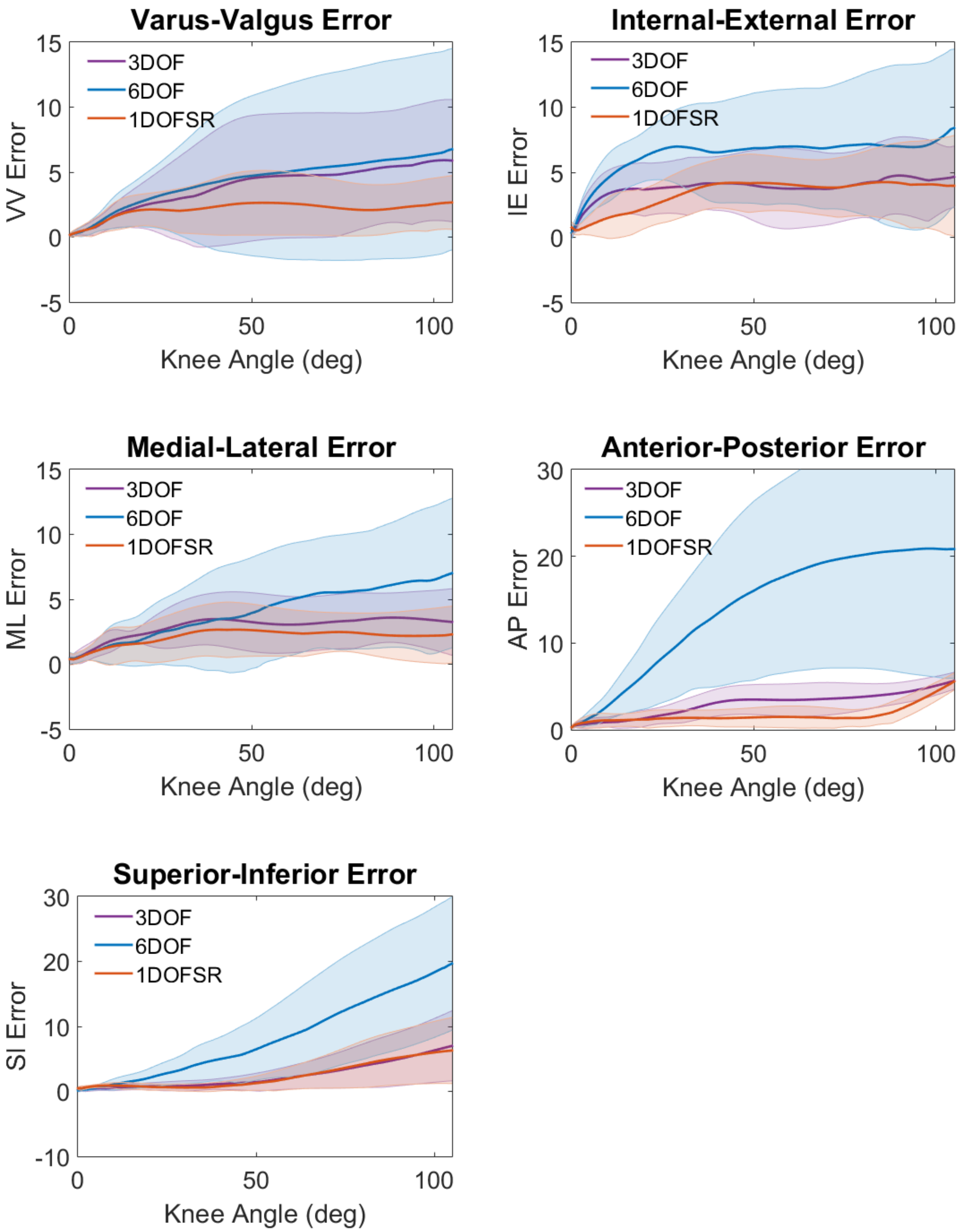

Figure 5.2 Mean error and standard deviation for each modeling modality across all subjects during the knee extension task.

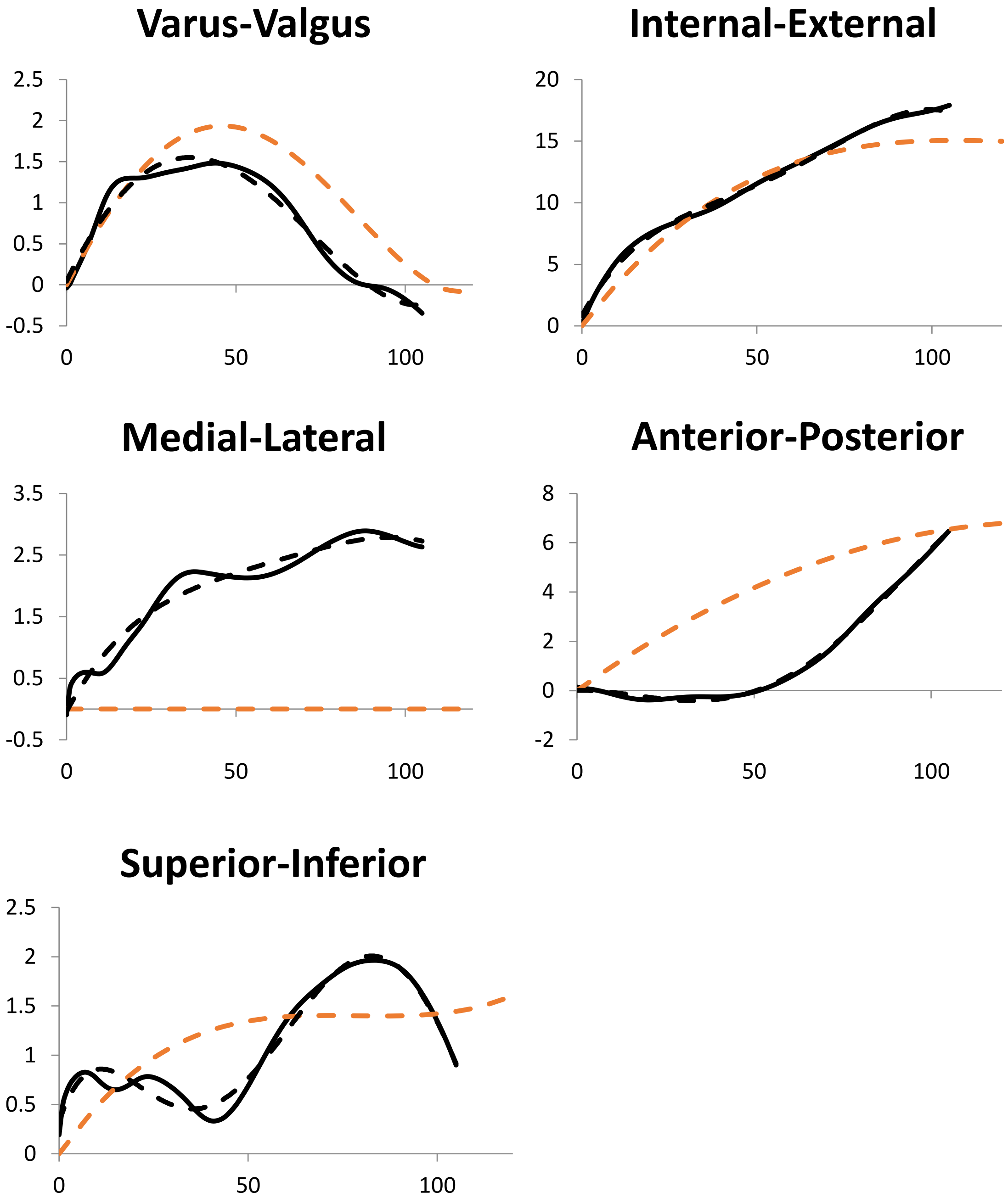

Figure 5.3 Mean subject kinematics (black-solid) plotted as a function of flexion angle for secondary DOF with kinematic spline (black-dashed) and Walker et al splines (red-dashed) (Arnold et al., 2010; Walker et al., 1988).

Table 5.1 RMSE normalized by total excursion during the activity as measured with HSSR. Green cells denote normalized RMSE < 0.5, blue cells denote RMSE < 1.0, and white indicates RMSE > 1.0.

| | 3DOF FE | 6DOF FE | 1DOFSP FE | 3DOF VV | 6DOF VV | 1DOFSP VV | 3DOF IE | 6DOF IE | 1DOFSP IE |
|---|---|---|---|---|---|---|---|---|---|
| **EXT** | 0.02 | 0.02 | 0.02 | 1.18 | 1.45 | 0.41 | 0.21 | 0.33 | 0.17 |
| **GAIT** | 0.71 | 0.55 | 0.71 | 2.10 | 1.45 | 0.99 | 2.08 | 1.27 | 1.53 |
| **PIV** | 0.82 | 0.38 | 0.82 | 3.36 | 1.26 | 1.01 | 0.59 | 0.29 | 0.54 |
| **STEPD** | 0.57 | 0.43 | 0.57 | 2.19 | 0.87 | 0.82 | 1.42 | 0.93 | 0.78 |
| **MEAN** | **0.53** | **0.35** | **0.53** | **2.21** | **1.26** | **0.81** | **1.08** | **0.71** | **0.76** |

| | 3DOF ML | 6DOF ML | 1DOFSP ML | 3DOF AP | 6DOF AP | 1DOFSP AP | 3DOF SI | 6DOF SI | 1DOFSP SI |
|---|---|---|---|---|---|---|---|---|---|
| **EXT** | 0.52 | 1.00 | 0.40 | 1.10 | 4.71 | 0.95 | 0.45 | 1.66 | 0.37 |
| **GAIT** | 0.87 | 1.33 | 0.84 | 0.77 | 1.68 | 0.73 | 0.57 | 7.83 | 0.69 |
| **PIV** | 0.76 | 1.19 | 0.76 | 0.42 | 0.81 | 0.56 | 0.43 | 3.82 | 0.43 |
| **STEPD** | 0.98 | 1.52 | 0.91 | 0.36 | 0.93 | 0.53 | 0.41 | 4.24 | 0.47 |
| **MEAN** | **0.78** | **1.26** | **0.73** | **0.66** | **2.03** | **0.69** | **0.47** | **4.39** | **0.49** |

Table 5.2 Polynomial coefficients for kinematic splines that maintained $R^2$ >= 0.95.

| | **$C_0$** | **$C_1$** | **$C_2$** | **$C_3$** | **$C_4$** | **$C_5$** |
|---|---|---|---|---|---|---|
| **VV** | 4.428e-2 | 8.550e-2 | -1.233e-3 | -1.094e-6 | 4.598e-8 | |
| **IE** | 8.326e-1 | 5.149e-1 | -1.213e-2 | 1.562e-4 | -6.965e-7 | |
| **ML** | -4.258e-2 | 1.035e-1 | -2.009e-3 | 2.100e-5 | -8.438e-8 | |
| **AP** | 2.219e-3 | 4.709e-3 | -1.623e-3 | 3.916e-5 | -1.767e-7 | |
| **SI** | 3.222e-1 | 1.153e-1 | -7.937e-3 | 1.912e-4 | -1.776e-6 | 5.533e-9 |

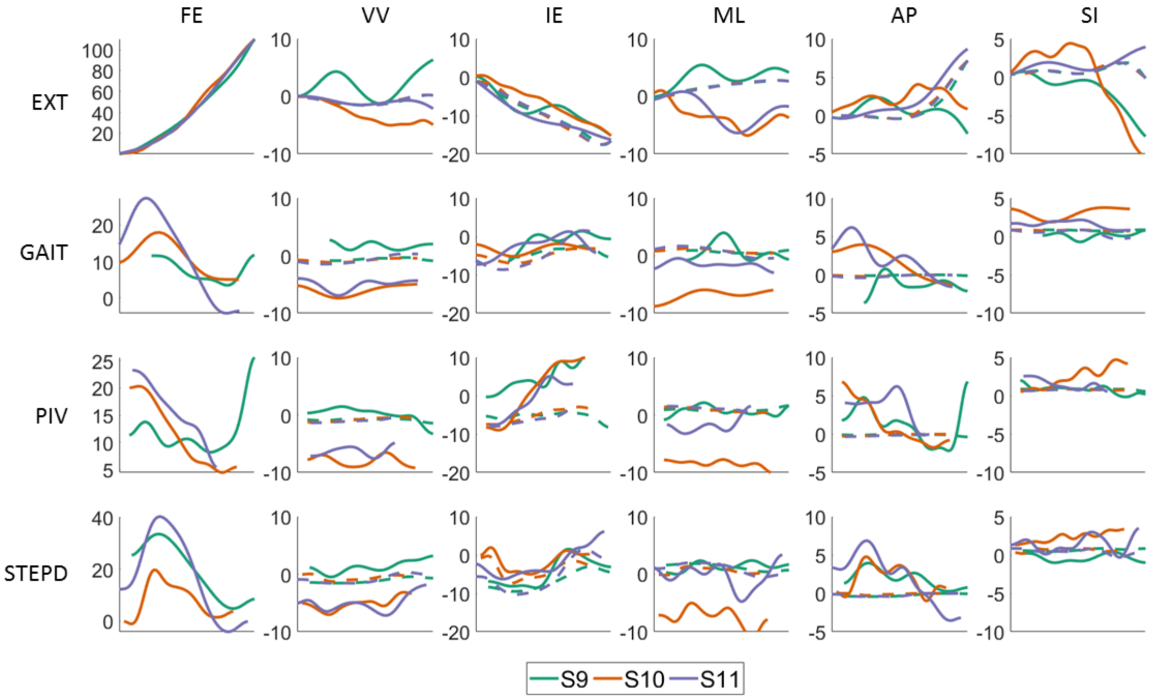

Figure 5.4 Kinematics calculated for 3 subjects using radiography-based bone tracking (solid) and kinematic splines developed from in vivo knee extension (dashed). Results plotted as a function of % activity.

Table 5.3 Mean RMSE normalized by total excursion for the three subjects depicted in Figure 4, comparing the radiography-based kinematics to kinematic spline results.

| | **VV-S** | **IE-S** | **ML-S** | **AP-S** | **SI-S** |
|---|---|---|---|---|---|
| **EXT** | 0.45 | 0.17 | 0.61 | 0.48 | 0.36 |
| **GAIT** | 1.56 | 0.50 | 1.33 | 0.43 | 084 |
| **PIV** | 1.67 | 0.59 | 1.68 | 0.44 | 0.41 |
| **STEPD** | 0.90 | 0.31 | 0.68 | 0.51 | 0.66 |
| **MEAN** | **1.17** | **0.39** | **1.08** | **0.46** | **0.57** |

# CHAPTER 6. A COMPUTATIONAL FRAMEWORK FOR BUILDING EXPLICIT FINITE ELEMENT MUSCULOSKELETAL SIMULATIONS DIRECTLY FROM LABORATORY DATA

## 6.1. Abstract

The interaction between muscle forces, muscle moment arms, and joint torque at the knee is an important relationship that influences the biomechanics of the musculoskeletal system. Finite element (FE) analyses allow for representation of structures such as joints and ligaments in sufficient detail to allow for accurate solutions of the internal stresses and strains in structures including complex contact conditions and material representations. Studies which performed muscle force optimization directly in a finite element framework were often limited in complexity to avoid lengthy computational time. However, recent advances in computational efficiency and control schemes for muscle force prediction have made these solutions more practical. Yet, the formulation of subject-specific MSFE simulations remains a challenging problem. The objectives of this work were to develop a computational framework to build and run simulations which (1) scale the size of MSFE models and efficiently estimate (2) joint kinematics and (3) muscle forces from data collected in the motion lab. A computational framework was built using MATLAB and python to interface directly with model input and output files. The software used laboratory

marker data to scale model segment lengths and estimate joint kinematics of subjects performing two activities. Concurrent muscle force and tissue strain estimations were performed using static optimization based on the estimated kinematics and ground reaction forces transformed to the foot. RMSE between subject and model marker locations fell between 3.5 mm and 11 mm indicating success in model scaling and kinematics estimation. Estimated muscle forces, ligament stress, and tibiofemoral contact compared well with previous studies and results from instrumented knee implants. This software will improve the usability of complex musculoskeletal simulations in a finite element framework.

## 6.2. Introduction

The interaction between muscle forces, muscle moment arms, and joint torque at the knee is an important relationship that influences the biomechanics of the musculoskeletal system and can only be described in a model that incorporates both joint deformability and muscle mechanics (Shelburne and Pandy, 2002)(see Chapter 3). Muscle forces contribute to joint load and have a strong influence on joint mechanics (Lenhart et al., 2015), which in turn partially determine muscle length, line-of-action, and moment arm (Fiorentino, 2013; Navacchia et al., 2017). Finite element (FE) analyses allow for representation of structures such as joints and ligaments in sufficient detail to allow for accurate solutions of the internal stresses and strains in structures including complex contact conditions and material representations such as anisotropic hyperelastic behavior (Fitzpatrick et al., 2010). Even so, studies which performed muscle force optimization directly in a finite element framework were often limited in complexity to avoid lengthy computational time (Adouni et al., 2012; Halloran et al., 2010, 2009; Lin et al., 2010). However, recent advances in computational efficiency (see Chapter 4) and control schemes for muscle force prediction (Navacchia et al. in review) have made these solutions more practical. Yet, the formulation of subject-specific MSFE simulations remains a challenging problem. The sequential approach to musculoskeletal modeling remains reliant on rigid body dynamics software packages for estimation of joint kinematics and transformation of ground reaction forces and moments to the musculoskeletal model. Using a separate tool creates a mismatch in joint mechanics between models of various complexities. As previously illustrated for muscle modeling (see Chapter 4), when used for kinematics estimation and load application the series modeling approach also inherits differences given active deformation of the joint and varying kinematic profiles.

The objectives of this work were to develop a computational framework to build and run simulations which (1) scale the size of MSFE models and efficiently estimate (2) joint kinematics and (3) muscle forces from data collected in the motion lab.

## 6.3. Methods

### 6.3.1. Computational Framework

A computational framework was developed to create a user-friendly software application for performing musculoskeletal finite element simulation work in ABAQUS/Explicit (Figure 6.1). The objectives of the framework were to (1) scale a generically sized MSFE model using optical marker data obtained from subject experiments, (2) estimate joint kinematics for the MSFE model using optical marker data, and (3) estimate muscle forces using kinematics and ground reaction forces and moments applied directly to the MSFE model. The software was written using MATLAB and python. MATLAB was used to manipulate model nodal geometry, build modeling input files, assign amplitudes (e.g. kinematics, kinetics, muscle and ground reaction forces), and manage asynchronous process control during optimization of kinematics and muscle forces. Python was used to interface directly with the FE input/output files to gather information needed for various steps in the modeling process. As an example, Python was used to read the resultant location of the foot center of mass (COM) after estimating kinematics to appropriately transform the ground reaction forces and moments to the foot for muscle force estimation. After development of the software was completed a proof-of-concept was performed by scaling the generic MSFE model and estimating kinematics and muscle forces for two subjects performing chair rising and gait.

### 6.3.2. Human Experiments

Laboratory measurements were collected from 2 healthy subjects in a previous study which considered activities of daily living in an older adult population (Kefala et al., 2017). Subject 1 (age 78, 153.0 cm, 59.1 kg) and Subject 2 (age 58, 177.2 cm, 74.5 kg) were chosen due to their differences in weight and height which required scaling from the generic MSFE model. The subjects provided informed consent to participate in a University of Denver IRB approved study. Each subject was screened for history of orthopedic injury to the lower extremity joints and conditions that limit function such as advanced osteoarthritis. Optical marker motion and force-plate reaction forces and moments were collected during chair rising and the stance phase of gait.

### 6.3.3. Musculoskeletal Model

An MSFE model of the lower limb including specimen-specific knee model was created for dynamic analyses in ABAQUS/Explicit (SIMULIA, Providence, RI) (Figure 6.2). The formulation for the model of the knee has been discussed previously (Ali et al., 2017, 2016; Harris et al., 2016)(see Chapters 3 and 4) but will be summarized below. The model included specimen-specific bone and cartilage geometry which were segmented from CT and MRI, respectively. Contact was modeled with a pressure-overclosure relationship, based on elastic foundation theory, previously verified to accurately mimic deformable contact (Fitzpatrick et al., 2010). The model included a 1 DOF hinge-joint at the ankle, a 3 DOF ball-joint at the hip, and 6 DOF joints representing the tibiofemoral (TF) and patellofemoral (PF) joints.

TF and PF ligaments were calibrated to specimen specific laxity and flexion-extension tests (Ali et al., 2016; Harris et al., 2016). Seven ligamentous structures crossing the tibiofemoral joint were represented and modeled as bundles of point-to-point tension-only non-linear springs which were calibrated to the joint laxity envelope of the same specimen whose geometry was used to build the knee ("S1" in Harris et al.). Patellar and quadriceps tendon were modeled as 2D reinforced membrane elements permitted to wrap over cartilage and bone (Baldwin et al., 2009).

Twenty muscles spanning the hip, knee, and ankle were represented as 3-element Hill-type muscles. The muscles represented in the model were soleus, gastrocnemius (medialis and lateralis), tibialis anterior, vastus medialis (3 musculotendon units), vastus intermedius, vastus lateralis (2 units), rectus femoris, semimembranosus, semitendinosus, biceps femoris short and long head, gluteus maximus (3 units), iliacus, and psoas. Insertion and origin were derived initially from anatomical landmarks as reported by Delp et al. (2007). Muscle geometries were calibrated such that moment arms calculated during passive knee flexion closely matched values reported from *in vitro* experiments (Buford et al., 1997). Hill-type muscle model parameters were calibrated to match mean isometric flexion and extension torques recorded from healthy subjects (Hume et al., 2018).

### 6.3.4. Model Scaling

The purpose of model scaling is to take a generically sized model, and with the help of optical marker data from a standing static trial, scale the segment lengths of the generic model to match the subject's segment lengths. The ability to scale each segment of the MSFE model is an important aspect of musculoskeletal modeling and likely paramount to the success of accurate kinematics and muscle force estimations (Lund et al., 2015). The software gives the user the ability to choose any two markers to scale any of three axes (ML, AP, SI) of a segment. Input files including bony geometries of the MSFE model (pelvis, right femur, right tibia, right midfoot) were imported into the scaling software. A standing static subject trial with full body marker set obtained from the subject experiments was imported and aligned with the MSFE bony geometry. Markers extraneous to lower limb modeling, such as those on the upper extremity and contralateral limb, were removed. Markers were then individually placed on appropriate bony landmarks through the software to echo placement from the *in vivo* data collection. The newly aligned markers were exported as an input file of the MSFE model and rigidly fixed to each segment. Scaling was performed on each segment of the MSFE model using the ratio of the distances between markers placed at the proximal and distal ends of each segment of the model when compared to the *in vivo* static trial. For example, the thigh segment was scaled using the ratio of the lengths between the markers placed on the greater trochanter and the lateral epicondyle of the femur. These scaling factors were then used to scale the model along the long axis of each segment. Model anthropometrics were updated using the subject mass and new geometries defined by scaled model marker locations (Hanavan, 1964). The software was then used to export a model with updated geometry for subsequent analyses.

### 6.3.5. Kinematics Estimation

Kinematics were estimated from motion capture data for the stance phase of gait and a chair rise activity. Marker data from subject experiments were imported into the software and appropriately cropped to include only the time range of interest for each activity. For gait this included stance phase, and for chair rise this included the duration from dual limb weight acceptance to full knee extension. The data were then down sampled to minimize the required number of optimizations, and thus computational time, of the analyses. Markers defining the angle at the hip, knee, and ankle were defined and used as initial guesses for the kinematics optimization routine. Input files corresponding to kinematics guesses were exported from the software.

Kinematics optimization was performed at 5 Hz for chair rising, which corresponded to 7 and 8 time points for Subjects 1 and 2, respectively. To illustrate extensibility of the modeling framework optimization was performed at 5 Hz and 20 Hz for stance phase, which corresponded to 6 and 15 time points for Subjects 1 and 2, respectively. All 36 time points were optimized in parallel using the software to improve computational efficiency of the modeling process. The goal of the optimization was to minimize the weighted least squares distance between the model markers and the experimental marker positions. Kinematics describing the position and rotation of the pelvis, three rotations of the hip joint, flexion of the knee joint, and flexion of the ankle joint were solved for using a bounded Nelder-Mead simplex direct search algorithm. The varus-valgus, internal-external, medial-lateral, anterior-posterior, and super-inferior DOF were solved for implicitly in the model through the interaction of muscle, ligament, and articular contact. While six DOF kinematics at the knee could be prescribed using radiography-based kinematics or kinematic splines eliminating contact and improving computational time, full contact solutions were obtained to highlight the robustness of a single framework MSFE musculoskeletal model.

### 6.3.6. Muscle Forces Estimation

Muscle forces were estimated for Subject 1 and 2 for gait and chair rise. The software used the resultant kinematics of the MSFE model and ground reaction forces and moments from *in vivo* subject experiments to transform and apply reaction loads to the foot center of mass. Like the kinematics estimation, optimization was performed on 36 time points corresponding to two activities for Subject 1 and 2. The goal of the optimization was to minimize the residual flexion torques developed by each joint required to maintain the kinematics obtained previously while minimizing the sum of the squared muscle stress (Crowninshield and Brand, 1981). Once again, secondary DOF at the knee were solved for based on the interaction between muscle forces, ligament, and articular contact. TF ligament loads, as well as TF and PF contact forces and center of pressure locations were obtained for both subjects during each activity. Kinematics were compared in passive (kinematics optimization) and active (muscle force optimization) to demonstrate the effects of a single framework deformable joint representations. Muscle forces, contact forces, and ligament loading are reported for each subject during the two activities.

## 6.4. Results

The time required by the user to scale the MSFE model and build the simulation input files for kinematics estimation and muscle force estimation using the software framework took less than 2 hours in total. Results reported for both models will be reported as "Subject 1, Subject 2", unless otherwise stated.

### 6.4.1. Model Scaling

Scaling was performed on Subject 1 and Subject 2 (Figure 6.3). The femur and tibia were scaled along the long axis of the bones using the ratio of the distances between the greater trochanter and lateral femoral epicondyle, and the lateral femoral epicondyle down to the lateral malleolus, respectively. The foot was scaled in the AP direction using the ratio of the distance between the calcaneus and head of the first metatarsal. The pelvis was scaled in the ML direction using the ratio of the distance between markers placed on the anterior-superior iliac spines. Scaling parameters can be found in Table 6.1 for both subjects.

### 6.4.2. Kinematics Estimation

Parallel simulations of kinematics estimation for chair rise and gait required 40 hours using a desktop workstation with 2 Intel Xeon Gold 3.20 GHz processors (32 cores in total) and 128.0 GB of memory. Each iteration of kinematic optimization took approximately 5 minutes of computational time, therefore requiring a maximum of 500 iterations to complete all 36 time-points. Results for kinematics optimization had root mean squared errors that fell between 3.5 mm and 11 mm for both activities (Figure 6.4). Generally, chair rising saw larger RMSE results than gait due to the soft tissue artifact seen in deep hip and knee flexion. Anterior and posterior-superior iliac spines (ASIS, PSIS), medial and lateral femoral epicondyles (MKNE, LKNE), and medial and lateral ankle (MANK, LANK) were assigned weights of 5 with the remaining markers assigned weights of 1. Due to large amounts of occlusion seen to ASIS markers during chair rise, the weights were changed to 1 and markers placed on the pelvic crest were increased to 5. Secondary kinematics at the knee were solved implicitly based on the interaction of muscle, ligament, and cartilage contact. The relative changed was calculated during the chair rise between secondary TF kinematics from passive kinematics estimation and from active muscle force optimization (Figure 6.5). Maximum differences seen in anterior-posterior (-10.1 mm) and internal-external (-18.8 mm) DOF illustrate changes due to loading exhibited by the joint and the importance of a high fidelity joint representation in kinematics and muscle force estimation.

### 6.4.3. Muscle Forces Estimation

Parallel simulations of muscle force optimization for chair rise and gait required 60 hours using the same desktop workstation. Each iteration took approximately 6 minutes of computational time, therefore requiring a maximum of 600 iterations to complete all time-points.

During the chair rise activity, quadriceps forces peaked during largest knee flexion (2690, 4440 N) and decreased as the knee extended (347, 798 N) (Figure 6.2). Resultant muscle forces at the hip were small, except for Subject 2’s gluteus maximus at the beginning of the chair rising activity (S2: 724 N). Ankle plantar and dorsiflexor muscles were also small in magnitude, except for Subject 1’s plantar flexors which increased as the knee extended. TF contact forces were largest during deepest knee flexion (373%, 507% BW) and decreased as the knee extended (244%, 282% BW), except for Subject 2 which saw a moderate increase during the last 30% of the activity. PF contact forces mimicked the muscle forces estimated for the quadriceps with peak contact occurring in deepest knee flexion (325%, 502% BW). The PCL and MCL carried load throughout the chair rise, peaking at the beginning of the activity with 389, 552 N and 390, 532 N, respectively.

During the stance phase of gait, quadriceps forces peaked during weight acceptance (1155, 1170 N) while gastrocnemii forces increased throughout stance and peaked at contralateral heel-strike (550, 911 N) (Figure 6.3). TF contact forces peaked during full weight acceptance (378%, 366% BW) with a second peak occurring at contralateral heel-strike (335%, 430% BW) driven by gastrocnemii forces. PF contact forces mimicked quadriceps forces and saw a peak during weight acceptance (93%, 49% BW). Ligament loads were small in magnitude, with both Subject 1 and 2 seeing a large peak in PCL loading occurring just before toe-off (191, 402 N).

## 6.5. Discussion

A computational framework to estimate joint kinematics and muscle forces in a single framework multi-scale musculoskeletal finite element model was developed using

MATLAB (Mathworks, Natick, MA) and Python for software development and model interfacing. The musculoskeletal model combined representations of the bones, muscles, tendons, and ligaments into a deformable model of the lower extremity. The framework developed included functionality for scaling the generic MSFE model to match subject segment lengths and scale anthropometric parameters based on optical markers placed on bony landmarks. Kinematics were estimated using a least squares optimization to estimate 3, 1, and 1 DOF kinematics at the hip, knee, and ankle respectively. The 5 secondary DOF at the knee were solved for implicitly through the interaction of cartilage, ligament, and muscle. Muscle forces were estimated using an inverse dynamics approach which utilized a static optimization to solve the muscle redundancy problem. Analysis was performed to estimate muscle forces and tissue strain concurrently to provide a more realistic pathway for musculoskeletal modeling. This research is important because it demonstrated the ability to estimate kinematics and muscle forces directly in a finite element environment from laboratory data such as optical marker motion and force plate reaction loads.

Model scaling was performed using the ratio of marker distances on the model compared to the subjects. Generally, Subject 1 was smaller in stature while Subject 2 was larger. Non-linear isotropic three-dimensional segment scaling is possible in the presented software, however scaling was performed along the long axis of the femur and tibia to limit the effect on the musculoskeletal system geometry affecting moment arms and lines of action calibrated previously. Despite subject bony geometry being unavailable for validation in the current study, model scaling was successfully demonstrated by the minimum RMSE values for Subject 1 (3.4 mm) and Subject 2 (5.2 mm) during kinematics estimation. Recent work has demonstrated non-isotropic scaling of musculoskeletal models from sparse landmarks using an articulated statistical shape model (Zhang et al., 2016). This method saw significant improvements in pelvis and femur segment scaling when compared to isotropic scaling methods. Scaling methods which take advantage of subject imaging or non-isotropic scaling techniques may yield improved results when scaling high fidelity MSFE models. However, isotropic segment-based scaling of the complex MSFE model allowed for a more realistic and repeatable estimation of subject specific kinematics and muscle forces.

Kinematics were estimated for Subjects 1 and 2 performing a chair rise task and during the stance phase of gait. Kinematics estimated from the same model as used in muscle force estimations provide a more accurate modeling pathway to eliminate the gap inherited by combining models of various complexities. Rigid body musculoskeletal modeling provides a fast method to estimate kinematics, but the knee is often represented as a hinge (Shelburne and Pandy, 1997) or using average kinematics obtained from cadaveric passive motion (Arnold et al., 2010; Delp et al., 2007). The MSFE modeling framework estimated 3, 1, and 1 DOF kinematics at the hip, knee, and ankle, respectively. The MSFE model also implicitly estimated secondary DOF at the knee determined by the interaction of cartilage contact, ligament restraint, and muscle loading. To the authors' knowledge this novel approach has not been performed previously and represents a step forward in musculoskeletal modeling using high fidelity joint representations. Previous work has demonstrated the effect of joint deformability on muscle forces and joint torques at the knee (see Chapters 3 and 4) supporting the need for single framework simulations with high fidelity joint representations when performing muscle force estimations. Joint deformability plots of Subjects 1 and 2 performing the chair rise show the change in kinematics at the knee between unloaded and loaded conditions for both subjects (Figure 6.5). Loaded conditions include applied ground reaction forces and moments and applied muscle force estimations while the unloaded condition includes prescribed and implicitly defined kinematics at the hip, knee, and ankle. The large changes seen in anterior-posterior and internal-external DOF affect muscle moment arms and thus muscle effectiveness. Single framework solutions effectively deal with the differences caused by subject-specific kinematics and complex joint response.

Muscle forces estimated during chair rising compared well with trends and magnitudes of previous predictions (Shelburne and Pandy, 2002). As expected the quadriceps peaked at largest knee flexion angles with minimal contribution from the antagonistic hamstring muscle group or gastrocnemii. Joint load predictions were similar to previously reported results from telemetric knee implants (Bergmann et al., 2014). Subject 2's deviation from the ±1 standard deviation bounds echoed the increased quadriceps forces at full extension and in deepest knee flexion. Loading of the PCL throughout the chair rising activity corroborated results reported by Shelburne and Pandy (2002). The knee model used in this MSFE model exhibits load sharing between the PCL and MCL during this activity, which was also echoed by results presented in Chapter 4.

Muscle forces estimated during the stance phase of gait compare well with previous estimations (Adouni and Shirazi-Adl, 2014a; Anderson and Pandy, 2001b). Quadriceps forces peaked during weight acceptance and gastrocnemii forces peaked at toe off as expected. Muscle forces predicted by the hamstrings and quadriceps oscillated between 50° and 70°. This can likely be explained by the inability of the static optimization technique to incorporate history dependence in muscle predictions. This is a common problem associated with static optimization and inverse kinematics and as much of a concern in rigid body dynamics as it is finite element musculoskeletal modeling. Tibiofemoral contact forces, though larger, imitate the dual peaked results demonstrated by the telemetric implant data. Both Subjects 1 and 2 see minimal ligament contribution during stance phase, with an expected peak of the PCL near toe-off.

The computational time required to run single framework finite element solutions for chair rising and gait, including both kinematics and muscle force estimation, was 100 hours in total. The four cases, described by two subjects each performing two activities, included 29 optimizations and were run in parallel simultaneously on four different workstations. Recent finite element optimization-based solutions reported run times between 32 hours and 4 weeks and included planar models of the joints (Halloran et al., 2010, 2009) and surrogate representations of the contact mechanism (Halloran et al., 2009; Lin et al., 2010). Musculoskeletal models implemented in rigid body dynamics software packages allow for fast estimation of kinematics and muscle forces, but they lack the ability to model complex anisotropic material representations (Ali et al., 2017). The work presented here both improves upon and highlights the ability to perform concurrent simulation of muscle force estimation and tissue strain analysis in a single framework using optimization-based prediction of joint kinematics and muscle forces.

Limitations associated with scaling and kinematics involve the placement of markers on the MSFE model. While it is straightforward to place markers on bony landmarks, the software does not give feedback as to the relative location of markers placed at mid-thigh or mid-tibia. Marker sets which include rigid clusters of markers located at mid segment would likely see an increase in RMSE results. Including functionality to scale the location of mid-segment markers based on placed markers at the proximal and distal segment ends would improve kinematic predictions. Furthermore, the neutral position of the foot should be calibrated prior to kinematics estimation. Placement of markers on the outside of the sneaker can lead to variable results with offsets in ankle-plantarflexion angle. Though not a limitation of methods, computational time is a consideration when performing FEA. Estimating kinematics and muscle forces in the MSFE represented nearly 100 hours of computational time, despite the parallel process control API developed in this work. MSFE models lend themselves to model modularity and thus hybrid optimization routines should be considered which perform quick, non-contact, rigid optimizations (kinematics, muscle forces) which then switch back over to complex representations during the last 10% of the optimization (using cost-function performance). This work also involves several limitations concerned with model representation. The ground reaction forces and moments were transformed to the resultant foot COM location after muscle forces estimated from laboratory EMG were applied to the model as an initial guess. The following optimization of muscle forces based on the minimization of muscle stress and resultant joint torque represents a change in distribution of force within muscle groups (minimize muscle stress) and change of total force contributions of antagonistic groups (minimize residual joint torques). The redistribution of muscle forces elicits changes in the internal-external DOF of the knee, as well as medial-lateral contact distribution which influences the hip-knee-ankle alignment. These changes in kinematics and alignment affect the final location of the foot COM during static optimization and thus diminish the integrity of the transformation of ground reaction forces and moments to the foot. Furthermore, the changes seen in internal-external rotation of the tibia and foot caused by changes in hamstring or quadriceps internal force distribution is not entirely realistic. Although the reaction forces and moments are applied to the foot center of mass, the lack of real contact represents a simplification in MSFE modeling that ultimately affects the accuracy of the tissue strain analysis. Promising results have been demonstrated in multibody dynamic analysis framework, ADAMS (MSC Software Corporation, Santa Ana, CA), which uses a deformable foot segment with regions of contact defined by elastic foundation theory (Guess et al., 2014). This implementation, like other rigid body dynamics applications, is limited in its ability to model complex material properties and deformation. Finding a computationally efficient method of foot-ground contact in MSFE modeling would improve the accuracy of joint and tissue stress analysis. A final limitation is concerned with computational time. Although improved over previous simulations, 40 hours of inverse kinematics and 60 hours of static optimization still represents a hurdle preventing these techniques from widespread use. MSFE modeling allows for modular model complexity of tissue definitions which can dramatically affect solution speeds. Furthermore, work in hybrid architecture (GPU/CPU) explicit finite element simulation appears promising

(Banihashemi, 2015) and will likely usher large improvements in computational time required for complex MSFE simulations.

In summary, a computational framework to build and perform concurrent estimation of muscle forces and tissue strain analysis was created to improve the accessibility of MSFE simulation. The study used optical marker-based motion and ground reaction forces and moments obtained in the lab to directly drive kinematics and muscle force estimation in a high-fidelity model of the lower which was scaled to subjects' size and anthropometrics. This software will improve the usability of complex musculoskeletal simulations in a finite element framework.

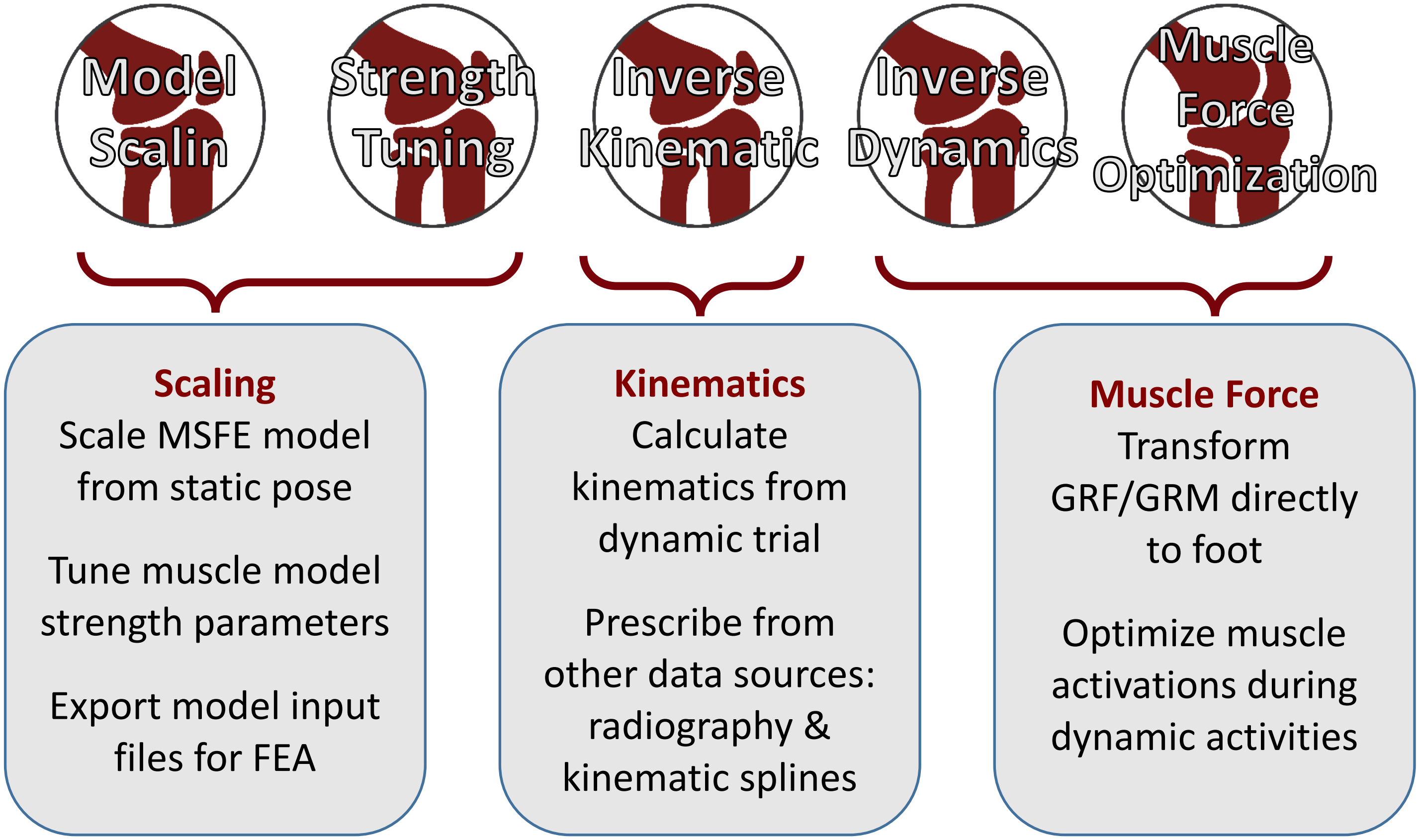

Figure 6.1 Flow chart describing the components of the computational framework: model scaling, inverse kinematics, and muscle force optimization. The framework represents a user-friendly approach to complex musculoskeletal finite element simulation.

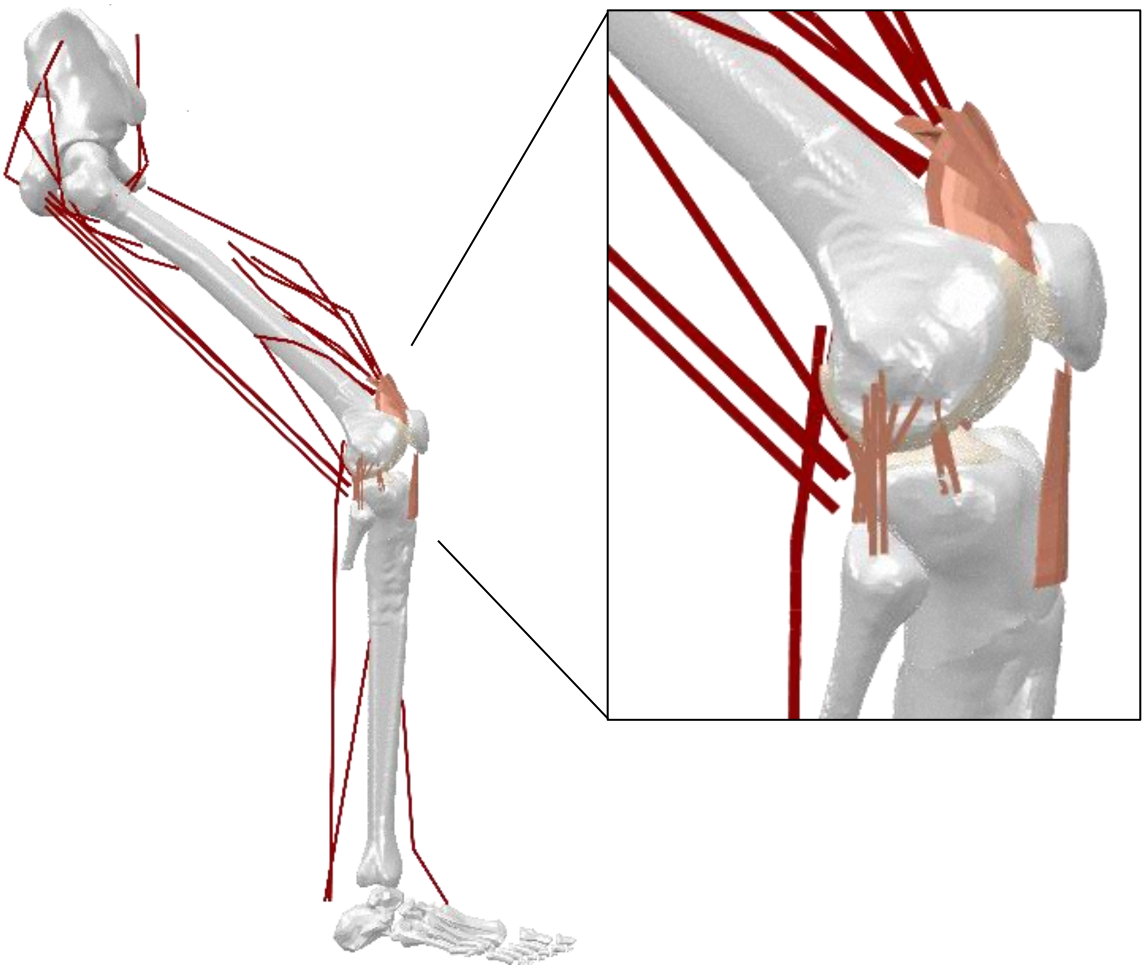

Figure 6.2 The lower limb musculoskeletal finite element model with calibrated specimen specific knee. The knees included TF and PF soft tissue structures whose response was calibrated to in vitro experiments (Ali et al., 2016; Harris et al., 2016). The model 15 unique muscles comprised of 20 musculotendon fibers which span the lower limb previously calibrated to match mean healthy isometric knee flexion-extension torque results (Chapter 3).

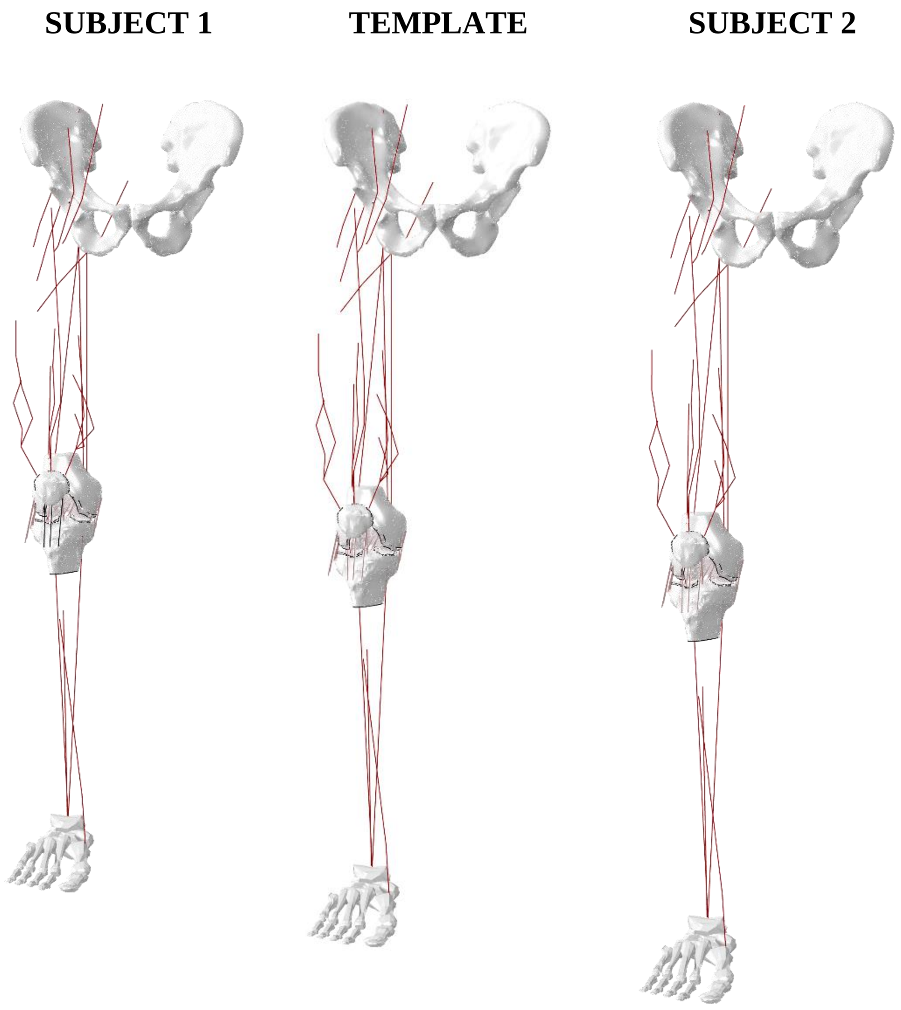

SUBJECT 1 TEMPLATE SUBJECT 2

Figure 6.3 Scaled lower limb models for Subjects 1 and 2 on either side of the template model.

Table 6.1 Scaling parameters used for Subject 1 and 2.

| | Subject 1 | Subject 2 |
|---|---|---|
| Pelvis ML | 1.09 | 1.00 |
| Femur SI | 0.97 | 1.02 |
| Tibia SI | 0.96 | 1.08 |
| Foot AP | 1.14 | 1.19 |

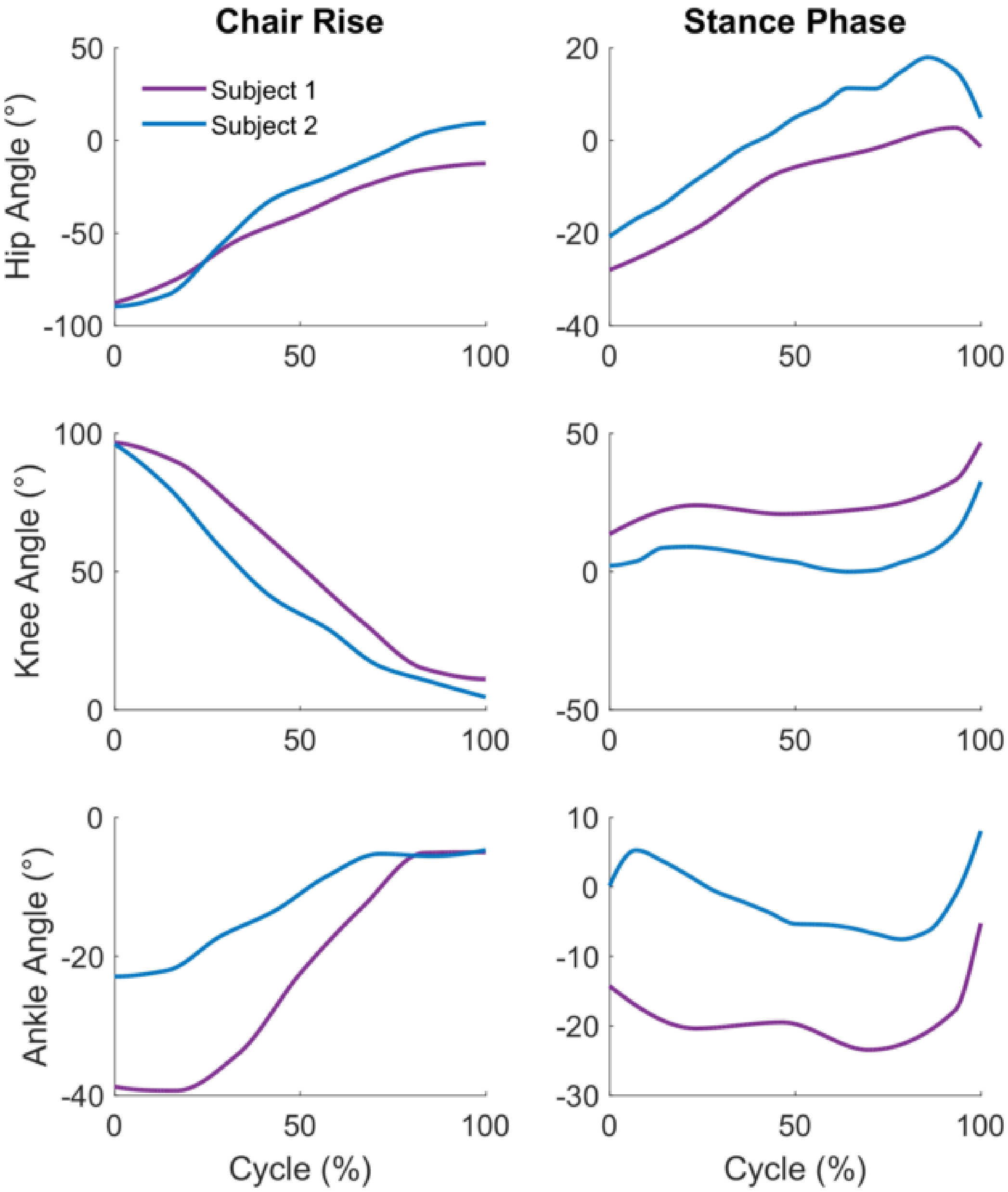

Figure 6.4 Subject-specific kinematics estimated at the hip, knee, and ankle for the flexion-extension DOF for Subject 1 and 2 while performing a chair rise and during the stance phase of gait.

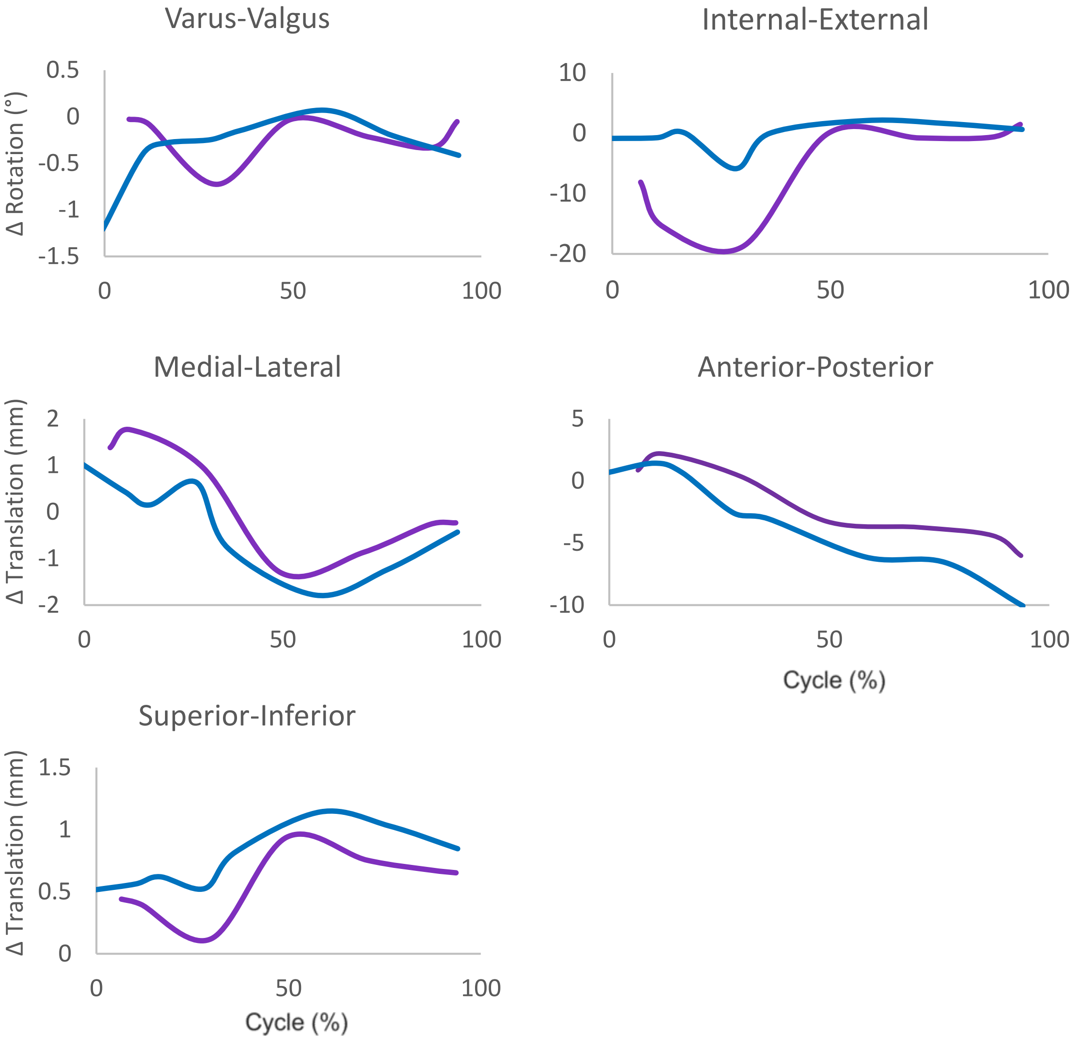

Figure 6.5: Change in implicitly described knee joint kinematics due to application of ground reaction loading at the foot and estimated muscle forces during chair rising for Subject 1 (blue) and Subject 2 (red). Secondary DOF knee kinematics are determined by the interaction of muscle forces, ligament constraint, and cartilage contact.

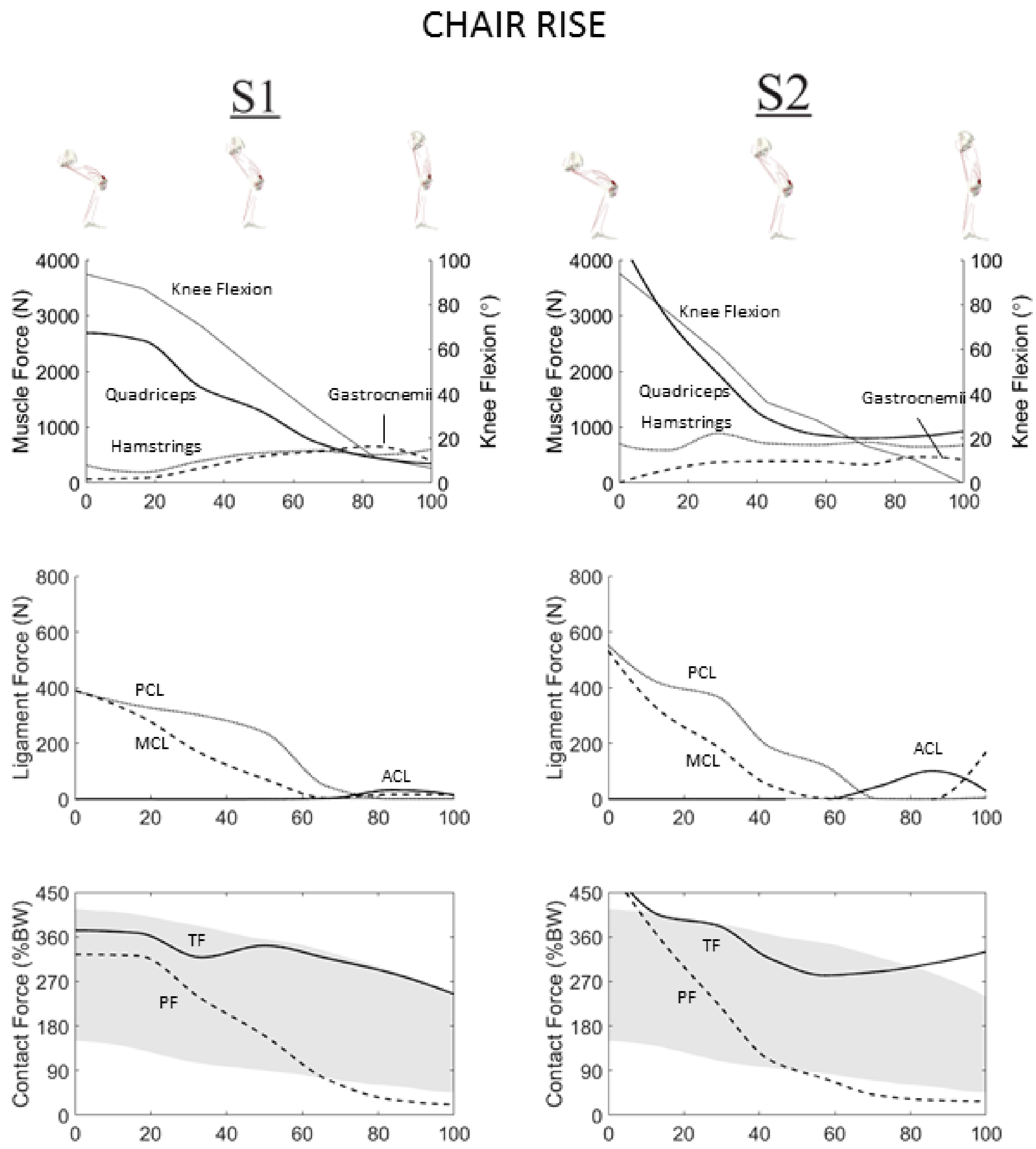

Figure 6.6: Forces prescribed by static optimization in muscle groups crossing the knee, forces carried by tibiofemoral ligaments, and contact forces (TF/PF) plotted against telemetric implant data (Bergmann et al., 2014) during a chair rise activity.

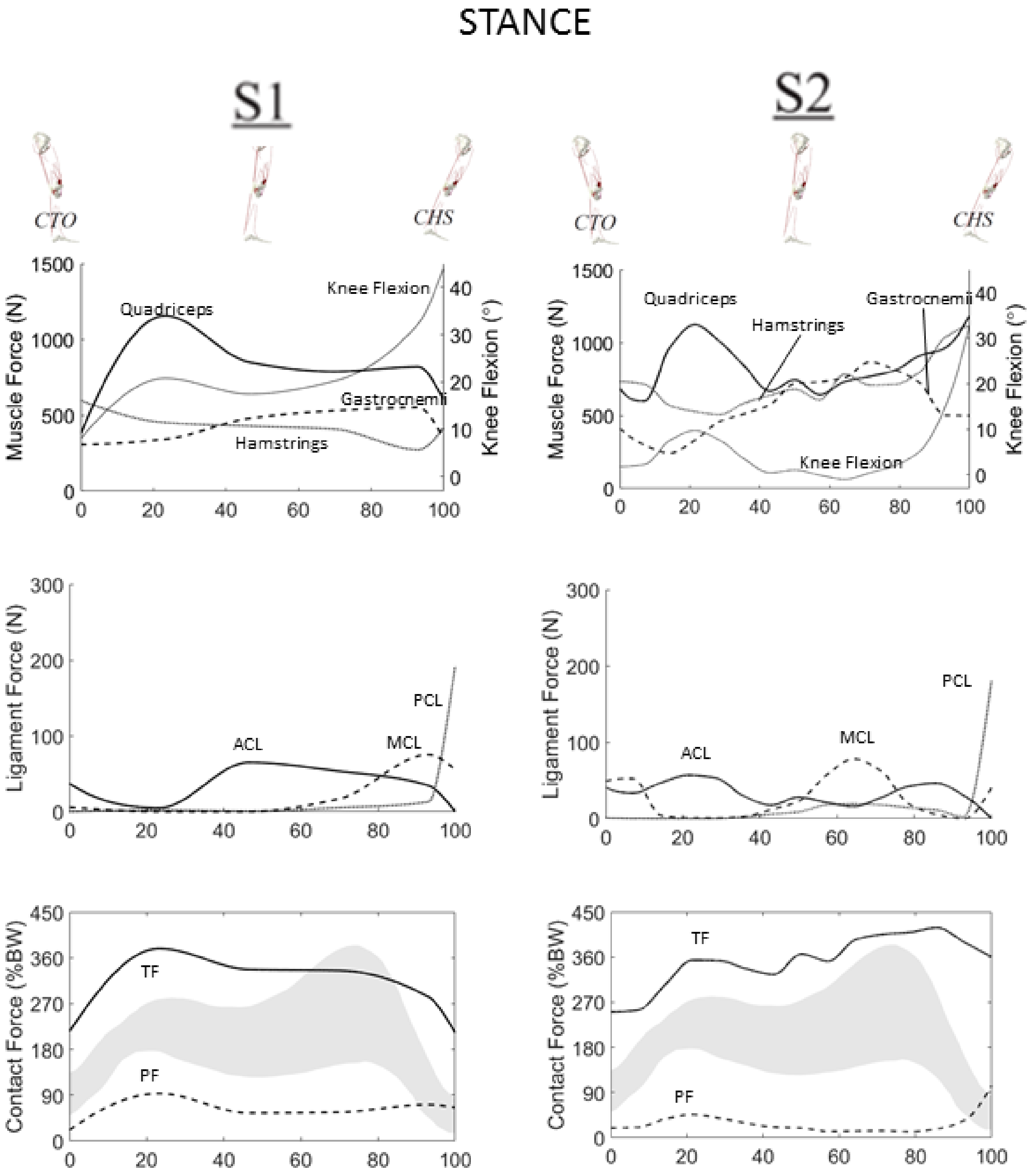

Figure 6.7: Forces prescribed by static optimization in muscle groups crossing the knee, forces carried by tibiofemoral ligaments, and contact forces (TF/PF) plotted against telemetric implant data (Bergmann et al., 2014) during the stance phase of gait.

# CHAPTER 7. CONCLUSIONS AND RECOMMENDATIONS

The objective of this dissertation was to advance upon current methods in single framework finite element musculoskeletal modeling. Single framework simulations are currently the state-of-the-art in musculoskeletal simulation work, but due to their high level of complexity have seen relatively minimal usage in the field of biomechanics. The goal was to improve the accessibility and usability of musculoskeletal finite element simulations by addressing three issues that are currently limiting the progression of this research: *model personalization*, *modeling infrastructure*, and *computational efficiency*.

Chapter 3 described the knee torque response of a single framework musculoskeletal finite element model with deformable representation of the knee and calibrate it to the average strength response from healthy subject sample during isometric flexion and extension activities. The force-length curve that represents the response of single fiber muscle models has been described as too short (Herzog and ter Keurs, 1988) limiting its ability to represent active tension through the entire excursion of the joint (Blemker and Delp, 2006, 2005). The multi-fiber representation of the quadriceps mechanism described in chapter 3, coupled with the calibration of muscle parameters used to describe force generating characteristics has improved the representation of strength response at the joint. This improvement in model personalization led to the accurate response of flexion and extension torque, which was then used to analyze response to loading that occurred at the knee due to a calibrated specimen-specific ligament representation. Large changes in flexion moment arms were observed in the model which have not been described previously in maximum isometric simulations and served to highlight the importance of a deformable model of the knee when estimating muscle forces.

Chapter 4 considered single framework muscle force estimations and tissue strain analyses. Static optimization, a common algorithm for solving the muscle redundancy problem, was used to estimate muscle forces while minimizing the sum of muscle stress. A computational environment was built to control parallel optimization of muscle forces at different time points throughout gait and chair rise; 13 time points were considered in total. The simulation of both tasks took nearly 60 hours for each subject. The time required to complete these simulations shows a large improvement over previous studies which performed complex muscle modeling directly in a finite element framework (Halloran et al., 2010, 2009). Muscle forces, ligament loads, and contact distribution compared well with previously reported simulation work and loads reported in patients with telemetric implants. As described in Chapter 2, the inverse dynamics method and static optimization technique are limited by the need for joint kinematics as input. There is currently no technique for estimating kinematics in a finite element environment and thus kinematics and ground reaction forces and moments were obtained from similarly sized subjects from OpenSim. This work highlighted the need for improved methods of kinematics estimation in single framework musculoskeletal simulation.

Chapter 5 considered the accuracy of marker-based methods for estimating kinematics when compared to kinematics obtained from radiography-based bone tracking. It was shown that the flexion-extension degree of freedom (DOF) in all activities, and the internal-external DOF in activities with large excursion proved reliable in reproducing kinematics obtained from dynamic radiography. As described in Chapter 2, rigid body dynamics applications allow for computationally efficient estimation of kinematics, kinetics, and muscle forces in simplified representations of the body and joints. Kinematic splines based on the motion of cadaveric knees (Walker et al., 1988) have been implemented in a commonly used rigid body musculoskeletal model (Arnold et al., 2010) to improve upon the hinge representation of the knee joint. Updated kinematic polynomial splines were developed in this work based on the average healthy motion of the knee recorded using stereo radiography during *in vivo* knee extension to further improve kinematics predictions during simulation of activities performed *in vivo*. Although the results of this work highlighted the activity- and subject-specific differences in kinematics obtained from radiography-based methods, future work may consider subject-specific kinematic splines to describe healthy knee motion through computational modeling. Single framework musculoskeletal simulation work is computationally expensive, limiting its usefulness in the clinical setting. Previous work has incorporated surrogate representations of model features which drive large simulation time, such as contact (Lin et al., 2010). As an alternative, prescribed secondary DOFs as a function of flexion angle may lead to improved computational time during kinematics or muscle force optimization in single framework musculoskeletal models.

Chapter 6 presented a computational framework for estimating joint kinematics and muscle forces in a single framework musculoskeletal finite element (MSFE) model. To the author’s knowledge, no such software currently exists. OpenSim has seen success due in part to its ease of use and open source nature which has made it accessible to researchers around the globe. The development of such a software for MSFE simulation will lead to increased accessibility and usability of these methods through different areas of interest. The goal of this work was to develop a modeling infrastructure which acted to improve the computational efficiency of these optimization approaches to MSFE simulation by managing parallelization and asynchronous process control. The framework was successful in estimating subject specific kinematics at the hip, knee, and ankle while allowing for the complex interaction of cartilage, ligament, and muscle to determine the secondary kinematics at the knee. Muscle force estimation was then performed, and results were presented to illustrate the ability of MSFE models to predict tissue strains concurrently with muscle force estimations.

The work presented here seeks to improve upon current methods in MSFE modeling through improvements in *model personalization*, *modeling infrastructure*, and *computational efficiency*. Methods presented here parallel sophistication seen in models developed and presented in recent literature. Work by Guess et al. has shown concurrent prediction of muscle and tibiofemoral contact forces in healthy (Guess et al., 2013) and implanted knee joints (Guess et al., 2014) using MD Adams (MSC Software Corporation, Santa Ana, CA). The implementation of the lower limb model used 1-D non-linear springs to represent ligaments, and cartilage contact using regional contact defined by elastic foundation theory. Concurrent muscle and tibiofemoral contact force estimations have also been performed in SIMM (Musculographics Inc., Santa Rosa, CA) (Smith et al., 2015, 2016). Smith et al. estimated kinematics using marker data as input while prescribing secondary DOF at the knee as a function of knee flexion. Muscle forces were estimated during activities while accounting for the interaction of ligament (1-D springs), muscle forces, and cartilage contact (elastic foundation theory). AnyBody (AnyBody Technology, Aalborg, Denmark) has also been used to perform concurrent muscle force, contact, and ligament strain (1-D spring) analysis in TKA (Chen et al., 2016) and healthy populations (Marra et al., 2015) using a novel force dependent contact approach which allowed for more efficient elastic contact calculations. These four model implementations were developed in multi-body dynamics software applications in such a way as to push the software to the limits of potential sophistication. This dissertation has seen the presentation of a MSFE model with specimen-specific ligament representation (1-D non-linear springs) and cartilage contact (elastic foundation theory) built in a finite element framework. This work has improved upon the current state-of-the-art, specifically due to the formulation of the model for FEA which sets it apart from current work in the field of musculoskeletal modeling. FEA allows for research questions which explore stress-driven pathologies such as osteoarthritis and its effects on bone and cartilage strength, malalignment and success in outcomes to procedures such as high tibial osteotomy, and fixation or loosening seen after total joint replacement. Analysis of joint response to stresses and strains associated with these pathologies during *in vivo* loading can only be performed on a model developed for FEA with the ability to estimate kinematics and muscle forces from subject specific laboratory marker and forceplate data.

Future work in this area should seek to improve *quasi-subject-specific* joint soft tissue representations. Population based modeling using statistical shape models has been used to successfully predict cartilage and ligament geometry from subject-specific bony geometry (Smoger, 2016). As described throughout this work, understanding the *in vivo* loading of cartilage, meniscus, and ligament is nearly impossible. However, future efforts should be made to quantify the subject-specific joint-scale response from *in vivo* experiments. Chapter 5 described a method for reproducing mean knee kinematics of a healthy adult cohort performing a passive knee extension. Previous work calibrated ACL and PCL ligament parameters of the MSFE model with subject-specific knee articular geometry to best match subject-specific knee extension kinematics (Ali, 2017). Given highly accurate kinematics obtainable using high-speed stereo radiography (HSSR) it should be possible to calibrate *quasi-subject-specific* joint response, given reconstruction or prediction of articular cartilage as described previously. Alternatively, calibration to a mean joint laxity response for predicted or segmented subject-specific cartilage and ligament geometry would continue to progress toward the goal of truly subject-specific musculoskeletal finite element modeling.

Although this computational framework improves the efficiency and usability of high fidelity musculoskeletal modeling, work must continue to improve computational run times. Recent work has considered graphics processing units (GPUs) and hybrid solutions for explicit finite element analysis with promising results (Banihashemi, 2015). Within the next decade computers with the ability to compute $10^{18}$ floating point operations (exaflops) per second will be introduced (Vuduc and Czechowski, 2011). It is believed these computers will more closely mimic the architecture seen in the GPU, which is distinguished by its scalability and large memory bandwidth. However, improvements in performance aren't defined purely by the transfer of simulation work to the GPU, but more specifically FEA formulations which play to the GPU's hardware architecture with high concurrency (high volume updates) and regional nodal coherence (localized group updates) (Banihashemi, 2015). Therefore, some of the responsibility to improve MSFE falls to the developers behind finite element analysis (FEA) software packages. ABAQUS currently supports GPU integration for ABAQUS/Standard job formulations but lacks supports for the Explicit domain. Hybrid integration of CPU and GPU load sharing would reap substantial improvements in computational time making single framework MSFE modeling increasingly useable.

In conclusion this work described and improved upon current limitations associated with single framework finite element musculoskeletal simulation, specifically *model personalization, modeling infrastructure,* and *computational efficiency.* There will always be the need for improvements to research methods, but it is the author's hope that this work will be useful to the field of biomechanics and anyone interested in musculoskeletal modeling.

# REFERENCES

Ackerman, M.J., 1998. The Visible Human Project. Proc. IEEE 86, 504–511.

Adouni, M., Shirazi-Adl, A., 2014b. Partitioning of knee joint internal forces in gait is dictated by the knee adduction angle and not by the knee adduction moment. J. Biomech. 47, 1696–1703.

Adouni, M., Shirazi-Adl, A., 2014a. Evaluation of knee joint muscle forces and tissue stresses-strains during gait in severe OA versus normal subjects. J. Orthop. Res. 32, 69–78.

Adouni, M., Shirazi-Adl, A., Shirazi, R., 2012. Computational biodynamics of human knee joint in gait: From muscle forces to cartilage stresses. J. Biomech. 45, 2149–2156.

Akbarshahi, M., Schache, A.G., Fernandez, J.W., Baker, R., Banks, S., Pandy, M.G., 2010. Non-invasive assessment of soft-tissue artifact and its effect on knee joint kinematics during functional activity. J. Biomech. 43, 1292–301.

Ali, A.A., 2017. Specimen-Specific Natural, Pathological, and Implanted Knee Mechanics Using Finite Element Modeling. Univesity of Denver.

Ali, A.A., Harris, M.D., Shalhoub, S., Maletsky, L.P., Rullkoetter, P.J., Shelburne, K.B., 2017. Combined measurement and modeling of specimen-specific knee mechanics for healthy and ACL-deficient conditions. J. Biomech. 57, 117–124.

Ali, A.A., Shalhoub, S.S., Cyr, A.J., Fitzpatrick, C.K., Maletsky, L.P., Rullkoetter, P.J., Shelburne, K.B., 2016. Validation of predicted patellofemoral mechanics in a finite element model of the healthy and cruciate-deficient knee. J. Biomech. 49, 302–309.

An, K., Takahashi, K., Harrigan, T., Chao, E., 1984. Determination of muscle orientations and moment arms. J. Biomech. Eng. 106, 280.

Anderson, D.E., Madigan, M.L., Nussbaum, M. a, 2007. Maximum voluntary joint torque as a function of joint angle and angular velocity: model development and application to the lower limb. J. Biomech. 40, 3105–13.

Anderson, F., Pandy, M., 2001a. Dynamic Optimization of Human Walking. J. Biomech. Eng. 123, 381.

Anderson, F., Pandy, M., 2001b. Static and dynamic optimization solutions for gait are practically equivalent. J. Biomech. 34, 153–61.

Anderson, F.C., Pandy, M.G., 1999. A Dynamic Optimization Solution for Vertical Jumping in Three Dimensions. Comput. Methods Biomech. Biomed. Engin.

Anderson, F.C., Pandy, M.G., 2003. Individual muscle contributions to support in normal walking. Gait Posture 17, 159–69.

Anderst, W., Zauel, R., Bishop, J., Demps, E., Tashman, S., 2009. Validation of three-dimensional model-based tibio-femoral tracking during running. Med. Eng. Phys. 31, 10–16.

Andriacchi, T.P., Alexander, E.J., Toney, M.K., Dyrby, C., Sum, J., 1998. A point cluster method for in vivo motion analysis: applied to a study of knee kinematics. J. Biomech. Eng. 120, 743–9.

Armitage, O.E., Oyen, M.L., 2017. Indentation across interfaces between stiff and compliant tissues. Acta Biomater. 56, 36–43.

Arnold, E.M., Ward, S.R., Lieber, R.L., Delp, S.L., 2010. A model of the lower limb for analysis of human movement. Ann. Biomed. Eng. 38, 269–79.

Audu, M.L., Davy, D.T., 1985. The Influence of Muscle Model Complexity in Musculoskeletal Motion Modeling. J. Biomech. Eng. 107, 147.

Baldwin, M., Clary, C., Maletsky, L.P., Rullkoetter, P.J., 2009. Verification of predicted specimen-specific natural and implanted patellofemoral kinematics during simulated deep knee bend. J. Biomech. 42, 2341–2348.

Baldwin, M.A., Langenderfer, J.E., Rullkoetter, P.J., Laz, P.J., 2010. Development of subject-specific and statistical shape models of the knee using an efficient segmentation and mesh-morphing approach. Comput. Methods Programs Biomed. 97, 232–240.

Banihashemi, S., 2015. Parallel Explicit FEM Algorithms Using GPUs. Georgia Institute of Technology.

Bell, K.J., Ounpuu, S., DeLuca, P.A., Romness, M.J., 2002. Natural progression of gait in children with cerebral palsy. J. Pediatr. Orthop. 22, 677–82.

Bendjaballah, M., Shirazi-Adl, a, Zukor, D., 1997. Finite element analysis of human knee joint in varus-valgus. Clin. Biomech. 12, 139–148.

Bendjaballah, M.Z., Shirazi-Adl, A., Zukor, D.J., 1998. Biomechanical response of the passive human knee joint under anterior-posterior forces. Clin. Biomech. 13, 625–633.

Benoit, D.L., Ramsey, D.K., Lamontagne, M., Xu, L., Wretenberg, P., Renström, P., 2006. Effect of skin movement artifact on knee kinematics during gait and cutting motions measured in vivo. Gait Posture 24, 152–164.

Bergmann, G., Bender, A., Graichen, F., Dymke, J., Rohlmann, A., Trepczynski, A., Heller, M.O., Kutzner, I., 2014. Standardized Loads Acting in Knee Implants. PLoS One 9, e86035.

Besier, T.F., Fredericson, M., Gold, G.E., Beaupré, G.S., Delp, S.L., 2009. Knee muscle forces during walking and running in patellofemoral pain patients and pain-free controls. J. Biomech. 42, 898–905.

Bigliani, L.U., Pollock, R.G., Soslowsky, L.J., Flatow, E.L., Pawluk, R.J., Mow, V.C., 1992. Tensile properties of the inferior glenohumeral ligament. J. Orthop. Res. 10, 187–197.

Blemker, S.S., Asakawa, D.S., Gold, G.E., Delp, S.L., 2007. Image-based musculoskeletal modeling: applications, advances, and future opportunities. J. Magn. Reson. Imaging 25, 441–51.

Blemker, S.S., Delp, S.L., 2005. Three-dimensional representation of complex muscle architectures and geometries. Ann. Biomed. Eng. 33, 661–673.

Blemker, S.S., Delp, S.L., 2006. Rectus femoris and vastus intermedius fiber excursions predicted by three-dimensional muscle models. J. Biomech. 39, 1383–1391.

Brekelmans, W.A.M., Poort, H.W., Slooff, T.J.J.H., 1972. A new method to analyse the mechanical behaviour of skeletal parts. Acta Orthop. 43, 301–317.

Buchanan, T.S., Lloyd, D.G., Manal, K., Besier, T.F., 2004. Neuromusculoskeletal modeling: estimation of muscle forces and joint moments and movements from measurements of neural command. J. Appl. Biomech. 20, 367–95.

Buford, W., Ivey F.M., J., Malone, J.D., Patterson, R.M., Peare, G.L., Nguyen, D.K., Stewart, a. a., 1997. Muscle balance at the knee - Moment arms for the normal knee and the ACL-minus knee. IEEE Trans. Rehabil. Eng. 5, 367–379.

Buford, W.L., Ivey, F.M., Nakamura, T., Patterson, R.M., Nguyen, D.K., 2001. Internal/external rotation moment arms of muscles at the knee: Moment arms for the normal knee and the ACL-deficient knee. Knee 8, 293–303.

Cappozzo, A., Catani, F., Leardini, a., Benedetti, M.G., Della Croce, U., 1996. Position and orientation in space of bones during movement: Experimental artefacts. Clin. Biomech. 11, 90–100.

Carbone, V., Fluit, R., Pellikaan, P., van der Krogt, M.M., Janssen, D., Damsgaard, M., Vigneron, L., Feilkas, T., Koopman, H.F.J.M., Verdonschot, N., 2015. Tlem 2.0–A Comprehensive Musculoskeletal Geometry Dataset For Subject-Specific Modeling Of Lower Extremity. J. Biomech. 48, 1–8.

Cereatti, A., Bonci, T., Akbarshahi, M., Aminian, K., Barré, A., Begon, M., Benoit, D.L., Charbonnier, C., Dal Maso, F., Fantozzi, S., Lin, C.C., Lu, T.W., Pandy, M.G., Stagni, R., van den Bogert, A.J., Camomilla, V., 2017. Standardization proposal of soft tissue artefact description for data sharing in human motion measurements. J. Biomech. 62, 5–13.

Chandrashekar, N., Mansouri, H., Slauterbeck, J., Hashemi, J., 2006. Sex-based differences in the tensile properties of the human anterior cruciate ligament. J. Biomech. 39, 2943–2950.

Chen, P.-Q., Wang, J.-L., Tsuang, Y.-H., Liao, T.-L., Huang, P.-I., Hang, Y.-S., 1998. The postural stability control and gait pattern of idiopathic scoliosis adolescents. Clin. Biomech. (Bristol, Avon) 13, S52–S58.

Chen, S.S., Falcovitz, Y.H., Schneiderman, R., Maroudas, A., Sah, R.L., 2001. Depth-dependent compressive properties of normal aged human femoral head articular cartilage: Relationship to fixed charge density. Osteoarthr. Cartil. 9, 561–569.

Chen, Z., Zhang, Z., Wang, L., Li, D., Zhang, Y., Jin, Z., 2016. Evaluation of a subject-specific musculoskeletal modelling framework for load prediction in total knee arthroplasty. Med. Eng. Phys. 38, 708–716.

Clary, C.W., Fitzpatrick, C.K., Maletsky, L.P., Rullkoetter, P.J., 2013. The influence of total knee arthroplasty geometry on mid-flexion stability: An experimental and finite element study. J. Biomech. 46, 1351–1357.

Crowninshield, R.D., Brand, R.A., 1981. A physiologically based criterion of muscle force prediction in locomotion. J. Biomech. 14, 793–801.

Cyr, A.J., Shalhoub, S.S., Fitzwater, F.G., Ferris, L.A., Maletsky, L.P., 2015. Mapping of Contributions From Collateral Ligaments to Overall Knee Joint Constraint: An Experimental Cadaveric Study. J. Biomech. Eng. 137, 61006–61007.

Delp, S.L., Anderson, F.C., Arnold, A.S., Loan, P., Habib, A., John, C.T., Guendelman, E., Thelen, D.G., 2007. OpenSim: open-source software to create and analyze dynamic simulations of movement. IEEE Trans. Biomed. Eng. 54, 1940–50.

Delp, S.L., Loan, J.P., Hoy, M.G., Zajac, F.E., Topp, E.L., Rosen, J.M., 1990. An interactive graphics-based model of the lower extremity to study orthopaedic surgical procedures. IEEE Trans. Biomed. Eng. 37, 757–767.

DeVita, P., Rider, P., Hortobágyi, T., 2016. Reductions in knee joint forces with weight loss are attenuated by gait adaptations in class III obesity. Gait Posture 45, 25–30.

Donahue, T.L.H., Hull, M.L., Rashid, M.M., Jacobs, C.R., 2002. A finite element model of the human knee joint for the study of tibio-femoral contact. J. Biomech. Eng. 124, 273–80.

Draganich, L.F., Andriacchi, T.P., Andersson, G.B.J., 1987. Interaction between intrinic knee mechanics and the knee extensor mechanism. J. Orthop. Res. 5, 539–547.

Dul, J., Johnson, G.E., Shiavi, R., Townsend, M.A., 1984. Muscular synergism-II. A minimum-fatigue criterion for load sharing between synergistic muscles. J. Biomech. 17, 675–684.

Ettema, G.J.C., Huijing, P.A., 1994. Effects of distribution of muscle fiber length on active length-force characteristics of rat gastrocnemius medialis. Anat. Rec. 239, 414–420.

Fernandez, J.W., Hunter, P.J., 2005. An anatomically based patient-specific finite element model of patella articulation: towards a diagnostic tool. Biomech. Model. Mechanobiol. 4, 20–38.

Fiorentino, N.M., 2013. Rectus Femoris Knee Muscle Moment Arms Measured in Vivo During Dynamic Motion With Real-Time Magnetic Resonance Imaging. J. Biomech. Eng. 135, 044501.

Fitzpatrick, C.K., Baldwin, M. a, Rullkoetter, P.J., 2010. Computationally efficient finite element evaluation of natural patellofemoral mechanics. J. Biomech. Eng. 132, 121013.

Fitzpatrick, C.K., Baldwin, M.A., Clary, C.W., Maletsky, L.P., Rullkoetter, P.J., 2014. Evaluating knee replacement mechanics during ADL with PID-controlled dynamic finite element analysis. Comput. Methods Biomech. Biomed. Engin.

Fitzpatrick, C.K., Steensen, R.N., Tumuluri, A., Trinh, T., Bentley, J., Rullkoetter, P.J., 2016. Computational analysis of factors contributing to patellar dislocation. J. Orthop. Res. 34, 444–453.

Forwood, M.R., Neal, R.J., Wilson, B.D., 1985. Scaling segmental moments of inertia for individual subjects. J. Biomech. 18, 755–761.

Fregly, B.J., Bei, Y., Sylvester, M.E., 2003. Experimental evaluation of an elastic foundation model to predict contact pressures in knee replacements. J. Biomech. 36, 1659–1668.

Fukashiro, S., Komi, P. V., Järvinen, M., Miyashita, M., 1993. Comparison between the directly measured achilles tendon force and the tendon force calculated from the ankle joint moment during vertical jumps. Clin. Biomech. 8, 25–30.

Gaffney, B.M., Harris, M.D., Davidson, B.S., Stevens-Lapsley, J.E., Christiansen, C.L., Shelburne, K.B., 2016. Multi-Joint Compensatory Effects of Unilateral Total Knee Arthroplasty During High-Demand Tasks. Ann. Biomed. Eng. 44, 2529–2541.

Gravel, D., Arsenault, A.B., Lambert, J., 1987. Soleus-gastrocnemius synergies in controlled contractions produced around the ankle and knee joints: an EMG study. Electromyogr. Clin. Neurophysiol. 27, 405–13.

Grood, E.S., Suntay, W.J., Noyes, F.R., Butler, D.L., 1984. Biomechanics of the knee-extension exercise. Effect of cutting the anterior cruciate ligament. J. Bone Joint Surg. Am. 66, 725–34.

Guess, T.M., Liu, H., Bhashyam, S., Thiagarajan, G., 2013. A multibody knee model with discrete cartilage prediction of tibio-femoral contact mechanics. Comput. Methods Biomech. Biomed. Engin. 16, 256–270.

Guess, T.M., Stylianou, A.P., Kia, M., 2014. Concurrent Prediction of Muscle and Tibiofemoral Contact Forces During Treadmill Gait. J. Biomech. Eng. 136, 021032.

Gulotta, L. V., Choi, D., Marinello, P., Knutson, Z., Lipman, J., Wright, T., Cordasco, F.A., Craig, E. V., Warren, R.F., 2012. Humeral component retroversion in reverse total shoulder arthroplasty: A biomechanical study. J. Shoulder Elb. Surg. 21, 1121–1127.

Haight, D.J., Lerner, Z.F., Board, W.J., Browning, R.C., 2014. A comparison of slow, uphill and fast, level walking on lower extremity biomechanics and tibiofemoral joint loading in obese and nonobese adults. J. Orthop. Res. 32, 324–330.

Halloran, J.P., Ackermann, M., Erdemir, A., van den Bogert, A.J., 2010. Concurrent musculoskeletal dynamics and finite element analysis predicts altered gait patterns to reduce foot tissue loading. J. Biomech. 43, 2810–2815.

Halloran, J.P., Erdemir, A., van den Bogert, A.J., 2009. Adaptive Surrogate Modeling for Efficient Coupling of Musculoskeletal Control and Tissue Deformation Models. J. Biomech. Eng. 131, 011014.

Hanavan, E.P., 1964. A mathematical model of the human body. AMRL-TR-64-102. Aerospace 1–149.

Harris, M.D., Cyr, A.J., Ali, A.A., Fitzpatrick, C.K., Rullkoetter, P.J., Maletsky, L.P., Shelburne, K.B., 2016. A Combined Experimental and Computational Approach to Subject-Specific Analysis of Knee Joint Laxity. J. Biomech. Eng. 138, 081004.

Herzog, W., ter Keurs, H.E., 1988. Force-length relation of in-vivo human rectus femoris muscles. Pflugers Arch. Eur. J. Physiol. 411, 642–647.

Heyse, T.J., Slane, J., Peersman, G., Dirckx, M., van de Vyver, A., Dworschak, P., Fuchs-Winkelmann, S., Scheys, L., 2017. Kinematics of a bicruciate-retaining total knee arthroplasty. Knee Surgery, Sport. Traumatol. Arthrosc.

Hill, A. V., 1938. The Heat of Shortening and the Dynamic Constants of Muscle. Proc. R. Soc. B Biol. Sci. 126, 136–195.

Hug, F., Lacourpaille, L., Maïsetti, O., Nordez, A., 2013. Slack length of gastrocnemius medialis and Achilles tendon occurs at different ankle angles. J. Biomech. 46, 2534–2538.

Hume, D.R., Navacchia, A., Ali, A.A., Shelburne, K.B., 2018. The Interaction of Muscle Moment Arm, Knee Laxity, and Torque in a Multi-Scale Musculoskeletal Model of the Lower Limb. J. Biomech. 76, 173–180.

Ivester, J.C., Cyr, A.J., Harris, M.D., Kulis, M.J., Rullkoetter, P.J., Shelburne, K.B., 2015. A Reconfigurable High-Speed Stereo-Radiography System for Sub-Millimeter Measurement of In Vivo Joint Kinematics. J. Med. Device. 9, 041009.

Jagodzinski, M., Leis, A., Iselborn, K.W., Mall, G., Nerlich, M., Bosch, U., 2003. Impingement pressure and tension forces of the anterior cruciate ligament. Knee Surgery, Sport. Traumatol. Arthrosc. 11, 85–90.

Jensen, R.H., Davy, D.T., 1975. An investigation of muscle lines of action about the hip: A centroid line approach vs the straight line approach. J. Biomech. 8.

Kadaba, M.P., Ramakrishnan, H.K., Wootten, M.E., 1990. Measurement of lower extremity kinematics during level walking. J. Orthop. Res. 8, 383–92.

Kefala, V., Cyr, A.J., Harris, M.D., Hume, D.R., Davidson, B.S., Kim, R.H., Shelburne, K.B., 2017. Assessment of Knee Kinematics in Older Adults Using High-Speed Stereo Radiography. Med. Sci. Sports Exerc. 49, 2260–2267.

Kim, H.J., Fernandez, J.W., Akbarshahi, M., Walter, J.P., Fregly, B.J., Pandy, M.G., 2009. Evaluation of predicted knee-joint muscle forces during gait using an instrumented knee implant. J. Orthop. Res. 27, 1326–1331.

Kim, H.Y., Kim, K.J., Yang, D.S., Jeung, S.W., Choi, H.G., Choy, W.S., 2015. Screw-Home Movement of the Tibiofemoral Joint during Normal Gait: Three-Dimensional Analysis. Clin. Orthop. Surg. 7, 303.

Klein Horsman, M.D., Koopman, H.F.J.M., van der Helm, F.C.T., Prosé, L.P., Veeger, H.E.J., 2007. Morphological muscle and joint parameters for musculoskeletal modelling of the lower extremity. Clin. Biomech. 22, 239–247.

Koo, S., Andriacchi, T.P., 2008. The knee joint center of rotation is predominantly on the lateral side during normal walking. J. Biomech. 41, 1269–1273.

Lenhart, R.L., Kaiser, J., Smith, C.R., Thelen, D.G., 2015. Prediction and Validation of Load-Dependent Behavior of the Tibiofemoral and Patellofemoral Joints During Movement. Ann. Biomed. Eng. 43, 2675–2685.

Lerner, Z.F., Board, W.J., Browning, R.C., 2014. Effects of obesity on lower extremity muscle function during walking at two speeds. Gait Posture 39, 978–84.

Li, G., Kaufman, K.R., Chao, E.Y.S., Rubash, H.E., 1999. Prediction of Antagonistic Muscle Forces Using Inverse Dynamic Optimization During Flexion/Extension of the Knee. J. Biomech. Eng. 121, 316.

Li, G., Wuerz, T.H., DeFrate, L.E., 2004. Feasibility of using orthogonal fluoroscopic images to measure in vivo joint kinematics. J. Biomech. Eng. 126, 314–318.

Li, K., Zheng, L., Tashman, S., Zhang, X., 2012. The inaccuracy of surface-measured model-derived tibiofemoral kinematics. J. Biomech. 45, 2719–2723.

Limbert, G., Taylor, M., Middleton, J., 2004. Three-dimensional finite element modelling of the human ACL: Simulation of passive knee flexion with a stressed and stress-free ACL. J. Biomech. 37, 1723–1731.

Lin, Y.-C., Walter, J.P., Banks, S. a, Pandy, M.G., Fregly, B.J., 2010. Simultaneous prediction of muscle and contact forces in the knee during gait. J. Biomech. 43, 945–52.

Lu, T.W., O'Connor, J.J., 1999. Bone position estimation from skin marker co-ordinates using global optimisation with joint constraints. J. Biomech. 32, 129–134.

Lund, M.E., Andersen, M.S., de Zee, M., Rasmussen, J., 2015. Scaling of musculoskeletal models from static and dynamic trials. Int. Biomech. 2, 1–11.

Lunnen, J.D., Yack, J., LeVeau, B.F., 1981. Relationship between muscle length, muscle activity, and torque of the hamstring muscles. Phys. Ther. 61, 190–5.

MacWilliams, B.A., Cowley, M., Nicholson, D.E., 2003. Foot kinematics and kinetics during adolescent gait. Gait Posture 17, 214–224.

Maletsky, L.P., Hillberry, B.M., 2005. Simulating Dynamic Activities Using a Five-Axis Knee Simulator. J. Biomech. Eng. 127, 123.

Manal, K., Buchanan, T.S., 2003. A Numerical Method for Estimating Tendon Slack Length. Adv. Bioeng. 2003, 235–236.

Mannen, E.M., Anderson, J.T., Arnold, P.M., Friis, E.A., 2015. Mechanical analysis of the human cadaveric thoracic spine with intact rib cage. J. Biomech. 48, 2060–2066.

Markolf, K.L., Mensch, J.S., Amstutz, H.C., 1976. Stiffness and laxity of the knee--the contributions of the supporting structures. A quantitative in vitro study. J. Bone Joint Surg. Am. 58, 583–94.

Markolf, K.L., O'Neill, G., Jackson, S.R., McAllister, D.R., 2004. Effects of Applied Quadriceps and Hamstrings Muscle Loads on Forces in the Anterior and Posterior Cruciate Ligaments. Am. J. Sports Med. 32, 1144–1149.

Marra, M.A., Vanheule, V., Fluit, R., Koopman, B.H.F.J.M., Rasmussen, J., Verdonschot, N., Andersen, M.S., 2015. A Subject-Specific Musculoskeletal Modeling Framework to Predict In Vivo Mechanics of Total Knee Arthroplasty. J. Biomech. Eng. 137, 020904.

Mattei, L., Campioni, E., Accardi, M.A., Dini, D., 2014. Finite element analysis of the meniscectomised tibio-femoral joint: implementation of advanced articular cartilage models. Comput. Methods Biomech. Biomed. Engin.

Meloni, G.R., Fisher, M.B., Stoeckl, B.D., Dodge, G.R., Mauck, R.L., 2017. Biphasic Finite Element Modeling Reconciles Mechanical Properties of Tissue-Engineered Cartilage Constructs Across Testing Platforms. Tissue Eng. Part A 23, 663–674.

Miranda, D.L., Schwartz, J.B., Loomis, A.C., Brainerd, E.L., Fleming, B.C., Crisco, J.J., 2011. Static and Dynamic Error of a Biplanar Videoradiography System Using Marker-Based and Markerless Tracking Techniques. J. Biomech. Eng. 133, 121002.

Moglo, K.E., Shirazi-Adl, A., 2003. Biomechanics of passive knee joint in drawer: Load transmission in intact and ACL-deficient joints. Knee 10, 265–276.

Moglo, K.E., Shirazi-Adl, A., 2005. Cruciate coupling and screw-home mechanism in passive knee joint during extension-flexion. J. Biomech. 38, 1075–1083.

Myers, C. a., Torry, M.R., Shelburne, K.B., Giphart, J.E., LaPrade, R.F., Woo, S.L.-Y., Steadman, J.R., 2012. In Vivo Tibiofemoral Kinematics During 4 Functional Tasks of Increasing Demand Using Biplane Fluoroscopy. Am. J. Sports Med. 40, 170–178.

Myers, C.A., Laz, P.J., Shelburne, K.B., Judd, D.L., Huff, D.N., Winters, J.D., Stevens-Lapsley, J.E., Rullkoetter, P.J., 2018. The impact of hip implant alignment on muscle and joint loading during dynamic activities. Clin. Biomech. 53, 93–100.

Navacchia, A., 2016. Multiscale Musculoskeletal Modeling of the Lower Limb. University of Denver.

Navacchia, A., Kefala, V., Shelburne, K.B., 2017. Dependence of Muscle Moment Arms on In Vivo Three-Dimensional Kinematics of the Knee. Ann. Biomed. Eng. 45, 789–798.

Navacchia, A., Myers, C.A., Rullkoetter, P.J., Shelburne, K.B., 2016a. Prediction of In Vivo Knee Joint Loads Using a Global Probabilistic Analysis. J. Biomech. Eng. 138, 031002.

Navacchia, A., Rullkoetter, P.J., Schütz, P., List, R.B., Fitzpatrick, C.K., Shelburne, K.B., 2016b. Subject-specific modeling of muscle force and knee contact in total knee arthroplasty. J. Orthop. Res. 34, 1576–1587.

Pandy, M.G., 2001. Computer modeling and simulation of human movement. Annu.Rev.Biomed.Eng 3:245-73., 245–273.

Pandy, M.G., Shelburne, K.B., 1998. Theoretical analysis of ligament and extensor-mechanism function in the ACL-deficient knee. Clin. Biomech. 13, 98–111.

Rajagopal, A., Dembia, C.L., DeMers, M.S., Delp, D.D., Hicks, J.L., Delp, S.L., 2016. Full-Body Musculoskeletal Model for Muscle-Driven Simulation of Human Gait. IEEE Trans. Biomed. Eng. 63, 2068–2079.

Reinschmidt, C., Van Den Bogert, a. J., Nigg, B.M., Lundberg, a., Murphy, N., 1997.

Effect of skin movement on the analysis of skeletal knee joint motion during running. J. Biomech. 30, 729–732.

Richards, C., Higginson, J.S., 2010. Knee contact force in subjects with symmetrical OA grades: Differences between OA severities. J. Biomech. 43, 2595–2600.

Schipplein, O.D., Andriacchi, T.P., 1991. Interaction between active and passive knee stabilizers during level walking. J. Orthop. Res. 9, 113–9.

Schwechter, E.M., Fitz, W., 2012. Design rationale for customized TKA: A new idea or revisiting the past. Curr. Rev. Musculoskelet. Med. 5, 303–308.

Shelburne, K.B., Pandy, M.G., 1997. A musculoskeletal model of the knee for evaluting ligament forces during isometric contractions. J. Biomech. 30, 163–176.

Shelburne, K.B., Pandy, M.G., 2002. A dynamic model of the knee and lower limb for simulating rising movements. Comput. Methods Biomech. Biomed. Engin. 5, 149–159.

Shelburne, K.B., Torry, M.R., Pandy, M.G., 2005. Muscle, ligament, and joint-contact forces at the knee during walking. Med. Sci. Sports Exerc. 37, 1948–1956.

Shelburne, K.B., Torry, M.R., Pandy, M.G., 2006. Contributions of Muscles , Ligaments , and the Ground-Reaction Force to Tibiofemoral Joint Loading During Normal Gait 1983–1990.

Sherman, M.A., Seth, A., Delp, S.L., 2015. Effectiveness in Biomechanical Models Using 1–18.

Shim, V.B., Fernandez, J.W., Gamage, P.B., Regnery, C., Smith, D.W., Gardiner, B.S., Lloyd, D.G., Besier, T.F., 2014. Subject-specific finite element analysis to characterize the influence of geometry and material properties in Achilles tendon rupture. J. Biomech. 47, 3598–3604.

Smith, C., Lenhart, R., Kaiser, J., Vignos, M., Thelen, D., 2015. Influence of Ligament Properties on Tibiofemoral Mechanics in Walking. J. Knee Surg. 29, 099-106.

Smith, C.R., Vignos, M.F., Lenhart, R.L., Kaiser, J., Thelen, D.G., 2016. The Influence of Component Alignment and Ligament Properties on Tibiofemoral Contact Forces in Total Knee Replacement. J. Biomech. Eng. 138, 1–10.

Smoger, L.M., 2016. Statistical Modeling to Investigate Anatomy and Function of the Knee. University of Denver.

Smoger, L.M., Fitzpatrick, C.K., Clary, C.W., Cyr, A.J., Maletsky, L.P., Rullkoetter, P.J., Laz, P.J., 2015. Statistical modeling to characterize relationships between knee anatomy and kinematics. J. Orthop. Res. 33, 1620–1630.

Stagni, R., Fantozzi, S., Cappello, A., Leardini, A., 2005. Quantification of soft tissue artefact in motion analysis by combining 3D fluoroscopy and stereophotogrammetry: A study on two subjects. Clin. Biomech. 20, 320–329.

Sueyoshi, T., Small, S.R., Elliott, J.B., Gibbs, G.E., Seale, R.B., Ritter, M.A., 2017. Mechanical Strength of the Proximal Tibia Following Total Knee Arthroplasty: A Cadaveric Study of Resection Depth and Bone Density. Surg. Technol. Int. 31, 170–176.

Taylor, K.D., Mottier, F.M., Simmons, D.W., Cohen, W., Pavlak, R.J., Cornell, D.P., Hankins, G.B., 1982. An automated motion measurement system for clinical gait analysis. J. Biomech. 15, 505–516.

Thelen, D.G., Anderson, F.C., 2006. Using computed muscle control to generate forward dynamic simulations of human walking from experimental data. J. Biomech. 39, 1107–1115.

Thelen, D.G., Won Choi, K., Schmitz, A.M., 2014. Co-simulation of neuromuscular dynamics and knee mechanics during human walking. J. Biomech. Eng. 136, 021033.

Torry, M.R., Shelburne, K.B., Peterson, D.S., Giphart, J.E., Krong, J.P., Myers, C., Steadman, J.R., Woo, S.L.Y., 2011. Knee kinematic profiles during drop landings: A biplane fluoroscopy study. Med. Sci. Sports Exerc. 43, 533–541.

Tsai, T.Y., Lu, T.W., Kuo, M.Y., Lin, C.C., 2011. Effects of soft tissue artifacts on the calculated kinematics and kinetics of the knee during stair-ascent. J. Biomech. 44, 1182–1188.

Tsirakos, D., Baltzopoulos, V., Bartlett, R., 1997. Inverse Optimization: Functional and Physiological Considerations Related to the Force-Sharing Problem. Crit. Rev. Biomed. Eng. 25, 371–407.

Umberger, B.R., 2010. Stance and swing phase costs in human walking. J. R. Soc. Interface 7, 1329–40.

Unsworth, A., Dowson, D., Wright, V., 1975. The Frictional Behavior of Human Synovial Joints—Part I: Natural Joints. J. Lubr. Technol. 97, 369.

Vuduc, R., Czechowski, K., 2011. What GPU computing means for high-end systems. IEEE Micro 31, 74–78.

Walker, P.S., Rovick, J.S., Robertson, D.D., 1988. The effects of knee brace hinge design and placement on joint mechanics. J. Biomech.

Walter, J.P., Korkmaz, N., Fregley, B., Pandy, M., 2015. Contribution of tibiofemoral joint contact to net loads at the knee in gait. J. Orthop. Res. 33.

Ward, S.R., Davis, J., Kaufman, K.R., Lieber, R.L., 2007. Relationship between muscle stress and intramuscular pressure during dynamic muscle contractions. Muscle Nerve 36, 313–9.

Ward, S.R., Eng, C.M., Smallwood, L.H., Lieber, R.L., 2009. Are Current Measurements of Lower Extremity Muscle Architecture Accurate? Clin. Orthop. Relat. Res. 467, 1074–1082.

Woo, S.L.Y., Hollis, J.M., Adams, D.J., Lyon, R.M., Takai, S., 1991. Tensile properties of the human femur- anterior cruciate ligament-tibia complex. Am. J. Sports Med. 19, 217–225.

Yamaguchi, G.T., Zajac, F.E., 1989. A planar model of the knee joint to characterize the knee extensor mechanism. J. Biomech. 22, 1–10.

Yao, J., Salo, A.D., Lee, J., Lerner, A.L., 2008. Sensitivity of tibio-menisco-femoral joint contact behavior to variations in knee kinematics. J. Biomech. 41, 390–398.

Zajac, F.E., 1989. Muscle and tendon: properties, models, scaling, and application to biomechanics and motor control. Crit. Rev. Biomed. Eng. 17, 359–411.

Zhang, J., Fernandez, J., Hislop-Jambrich, J., Besier, T.F., 2016. Lower limb estimation from sparse landmarks using an articulated shape model. J. Biomech. 49, 3875–3881.

Zhang, Y., Yao, Z., Wang, S., Huang, W., Ma, L., Huang, H., Xia, H., 2015. Motion analysis of Chinese normal knees during gait based on a novel portable system. Gait Posture 41, 763–768.

Zheng, L., Li, K., Shetye, S., Zhang, X., 2014. Integrating dynamic stereo-radiography and surface-based motion data for subject-specific musculoskeletal dynamic modeling. J. Biomech. 47, 3217–3221.

# APPENDIX A. RELATED PUBLICATIONS

Hume DR, Navacchia A, Ali AA, Shelburne KB, The Interaction of Muscle Moment Arm, Knee Laxity, and Torque in a Multi-Scale Musculoskeletal Model of the Lower Limb. J. Biomech. (2018), https://doi.org/10.1016/j.jbiomech.2018.05.030

Hume DR, Kefala V, Harris MD, Shelburne KB, Comparison of Marker-Based and Stereo Radiography Knee Kinematics in Activities of Daily Living. *Annals of Biomedical Engineering* (Accepted June 2018).

Navacchia A, Hume DR, Rullkoetter PJ, Shelburne KB. Closed Loop Muscle Control of a Finite Element Musculoskeletal Model of the Lower Limb. *Journal of Biomechanics* (In Review).

Kefala V, Cyr AJ, Harris MD, Hume DR, Davidson BS, Kim RH, Shelburne KB, Assessment of Knee Kinematics in Older Adults Using High-Speed Stereo Radiography. *Medicine & Science in Sports & Exercise*. 2017.

Hume DR, Navacchia A, Rullkoetter PJ, Shelburne KB, Muscle Force Estimations with a Finite Element Multi-Scale Musculoskeletal Model of the Healthy Human Knee. *64th Annual Meeting of the Orthopaedic Research Society.* New Orleans, LA, 2018. *Accepted for poster presentation, #1722.*

Hume DR, Navacchia A, Harris MD, Ali AA, Shelburne KB, Strength Response of a Specimen-Specific Multi-Scale Musculoskeletal Model of the Healthy Human Knee. *62nd Annual Meeting of the Orthopaedic Research Society.* Orlando, FL, 2016. *Accepted for podium presentation, #240.*

Harris MS, Ali AA, Navacchia A, Hume DR, Fitzpatrick CK, Rullkoetter PJ, Shelburne KB, A Multi-Scale Finite Element Framework for Modeling Natural Knee Mechanics. *Summer Biomechanics, Bioengineering, and Biotransport.* Snowbird, UT, 2015. *Accepted for podium presentation, #314.*

Hume DR, Cyr AJ, Kefala V, Gaffney BMM, Shelburne KB, Comparison of Marker-Based and Stereo Radiography Knee Kinematics in Assessment of Activities of Daily Living. *62nd Annual Meeting of the American College of Sports Medicine.* San Diego, CA, 2015. *Accepted for poster presentation, #213.*

Kefala V, Cyr AJ, Hume DR, Shelburne KB, Assessment of Normal Knee Kinematics During Activities of Daily Living in Older Adults. *62nd Annual Meeting of the American College of Sports Medicine.* San Diego, CA, 2015. *Accepted for poster presentation, #5.*

# APPENDIX B. COMPUTATIONAL FRAMEWORK: FILES AND FEATURES

## ApplyNodeset2Model.m

This script builds a GUI which allows the user to load MSFE bony geometry (.inp) as well as a static motion capture trial (.csv/.txt). Once loaded, the markers can be positioned appropriately on the MSFE geometry and exported as a model input file (.inp).

*Functional Decomposition*

Load FE Bone Geometry: Uses the function READ_MESH_NUMS_AJC.m or stlread_ascii_binary() to read in either an input file (.inp) or a CAD geometry file and load the nodes and elements associated with five segments: pelvis, femur, tibia, patella, and midfoot. The segments are plotted in the axes located on the left side of the GUI.

Load Static Marker Trial: Prompts the user to choose a static subject trial saved in either .txt or .csv format and reads and formats the marker data in. The read in is straightforward and can be described as two parts: marker names, marker data. Marker names are obtained by loading the entire text file and reading text from the first marker to until the string “Frame” is found. The text is then parsed to remove the subject name in each marker string as denoted by everything before and including the colon. Marker data is parsed using the dlmread() function and hard coded offsets for the start of the numeric data. The average is taken of each marker position through time, which highlights the importance of a static subject trial. Standard deviations greater than 10mm will produce an error in the command prompt. The marker positions will then be plotted in the axes on the left side of the GUI, and the names and x, y, z, coordinates will be added to the table on the bottom right.

Transform Marker Data Set: The buttons RotX, RotY, RotZ, +dX, +dY, +dZ allow for transformation of the entire marker set. Rotations are taken about the marker set centroid. This is helpful for aligning the marker set to the MSFE model which may be positioned differently in space than the optical marker data. Values can be keyed in for the magnitude of rotation and translation to the right of each set of buttons and are in units of degrees and millimeters, respectively.

Single Marker Manipulation: Selecting a marker from the list at the bottom right, allows the user to translate individual markers to align them to bony landmarks which correspond to placement during subject data collection. Markers can also be irreversibly removed using the “Delete Marker” button.

Export Markers to FE Input File: This section allows for the current alignment of markers to be exported to MARKERS.inp using the “Export to FE” button. The file is saved in the folder from which MSFE geometry was loaded, likely the model template folder. When MSFE scaling is performed this file will get copied to the new scaled model folder, and thus it is important that ApplyNodeset2Model.m isn’t run in sequence for more than one subject at a time, otherwise the MARKERS.inp file will get overwritten. The "Export Scaling.cfg" button exports a file with information that allows the same geometry and marker file to be imported in the next phase of the software. It also exports to the model template folder.

**CalculateSegmentScaling.m**

This script builds a GUI which allows the user to load marker data from static subject trial as well as MSFE model with newly attached markers. Scaling factors can then be calculated for 1 to 3 axes representing the ML, AP, and SI DOFs of each segment. Scaling factors for each segment are calculated by selecting two markers which describe a displacement in that DOF and then taking the ratio of this distance for the two marker sets. For this reason, it is preferable to use markers position on anatomical geometry, such as femoral epicondyle or anterior superior iliac spine.

*Functional Decomposition:*

Load Scaling.cfg: This button prompts the user to browse for the Scaling.cfg file which was exported at the conclusion of the ApplyNodeset2Model GUI. The information in this file allows the software to load MSFE bony geometry and MARKER.inp file as well as the static subject trial.

Static Trial Manipulation: These buttons allow for the transformation of the static subject marker set. The purpose of this section is purely visualization when determining markers to be used for scaling factors and can be skipped if desired. Rotation occurs about the marker set centroid and is specified in degrees. Translations are specified in millimeters.

Scale [*segment*]: Each section allows for two markers to be chosen which will then be used to calculate a scaling factor for the primary (long) axis of the segment. This scaling factor will be linearly applied in each DOF unless the "Linear" checkbox is unchecked at which time scaling factors can chosen or input for the other two DOF. Although the muscle, ligament, and articular geometry is not affected at the knee, scaling of segments will affect muscle geometry which travel along them affecting moment arms.

Export Scaling Data: This button exports ScalingParameters.mat which includes individual scaling metrics determined by the GUI. Default values are 1 unless otherwise updated.

**ApplyScaling2MSFEModel.m**

This script allows the user to load in ScalingParameters.mat and apply it to segment geometry in the MSFE Model. Anthropometrics are updated and ultimately a new scaled MSFE model is exported to the user defined output folder.

*Functional Decomposition*

Build Scaling Matrices: Load scaling parameters and build scaling matrices with x, y, and z corresponding to AP, ML and SI respectively.

Build Segment Coordinate System: Segment local coordinate systems (LCS) are built using a combination of model marker and joint center locations. These LCS are then combined with the scaling matrices to define segment scaling transformation matrices which will be applied to segment nodal geometry.

Copy No-Scale Files: Files without scaling are copied to model output folder. This includes scripts, text files, and DU01 knee geometry files corresponding to ligament, bone, and cartilage geometry. Knee geometry was maintained in this software to preserve specimen-specific response.

Copy and Scale [*segment*]: Files are transformed and scaled from the knee down through the foot, and from the knee up through the pelvis. In short, the knee joint center stays centered at (0,0,0).

Update Mass: Queries the user for the subject mass in kilograms and runs the UpdateAnthro( ) function. See *Implementation* for details.

*Implementation*

scaleNodeCoordinates(infile, outfile, nodes, scaleMat, transVec, origin)

The purpose of this function is to scale nodal geometry represented by node numbers in *nodes* found in a specific input file, *infile*, by translating it by *transVec* (determined by the scaling of the previous segment) and scaling it with *scaleMat* about *origin*. The scaled input file will then be written to the output folder defined by the path *outfile*. The parameter *nodes* can be set to -1 to dictate scaling of all nodal geometry in the file.

UpdateAnthro(MarkerPath,Mass,FootAPScaleFactor)

The purpose of this function is to recalculate subject segment anthropometry based on subject *Mass* and scaled model marker coordinates found in *MarkerPath*. Model marker names have been hard coded in as the search keywords for retrieving nodal coordinates with the intention of allowing for simple “recoding” when different marker sets are used. As an example, the pelvis is defined as an elliptical cylinder using markers: RASI, RPSI, LASI, LPSI, RCRT, LCRT, RTRO. The numerical formulation for each segment anthropometric estimation assumed segments were treated as geometric objects (elliptical cylinder and conical frustum) were based on descriptions provided by Hanavan (1964). For a review, a numerical formulation can be found on the C-Motion website (C-Motion, Germantown, MD) (http://c-motion.com/v3dwiki/index.php?title=Segment_Inertia). Pelvis, femur, and tibia use this method. Foot scaling is performed using an equation for moment of inertia scaling presented previously (Forwood et al., 1985) which requires the *FootAPScaleFactor*.

## **BuildIKSims.m**

This script builds a GUI which allows the user to load in trial marker data and build simulation files to perform single frame inverse kinematics estimations using FEA. The tool lets you choose frames and select markers to provide initial guesses for optimization seeding of pelvis location, hip angle, and knee angle.

### *Functional Decomposition*

Load Dynamic Trial: This allows the user to load a .csv or .txt file with marker motion data. The marker names are parsed and then dlmread( ) is used to read the entire block of marker coordinate data. Once the data has been loaded into the program the first available frame is displayed on the axes to the left of the GUI. Number of frames, start frame, end frame, and drop down boxes with marker names are updated. Tools for rotating and zooming the view can be found at the top left of the GUI.

Crop Trial: This allows the user to select a region of interest for which inverse kinematics will be performed. Once the start and end frame are keyed in, the update button will rescale the scrollbar, update the current frame number, and replot the first available frame of marker data in the axes.

Downsample Factor: This allows the user to down sample the number of frames included in the simulation. As an example, let’s say the start frame is set to 400 and then end frame is set to 799. The current frames will read 400. Updating the downsample factor to 2 will mean that only every other frame is included, and the current frames will read 200. Updating downsample factor to 20 will change the current frames to 20. Consideration should be given to selecting a value that makes sense given the frame rate of the marker data available.

Pelvis COM, Hip Angle, Knee Angle: These areas allow the user to choose markers which represent the pelvis COM when averaged together, or the hip and knee angle when taking the angle between three markers. These values are calculated for the entire trial and used to seed the optimization with an initial guess. Calculating the pelvis COM will add a red dot in the plot to confirm the user decision. Hip and Knee angle outputs will also be displayed at the bottom of the axes and updated at each frame.

Build Simulations: After typing in the activity name, clicking on the Build Simulations button will build IK simulation files including amplitude cards for kinematics (AMP) and main files (MAIN). There are two steps to the inverse kinematics: the first step moves the model into the approximated pose from the marker estimations, and the second step will be used in to perturb each DOF until the optimization converges on a solution. The initial guess for each optimization will be exported to InitialGuess_[frameNumber].txt

**IKWrapper.m**

This script performs inverse kinematics estimation via downhill simplex given input simulation files provided by BuildIKSims( ). The software builds a simulation/optimization queue and fills it until all simulations/optimizations have completed.

*Functional Decomposition*

User settings: Define settings for simulations such as task, marker file, optimization parameters, and max number of cores to run jobs. NumCores is an important variable which defines how many threads to create at a time. Creating more threads than CPU cores is possible with this code and is problematic.

Optimization Guess: This loads the InitialGuess_[frameNumber].txt for each kinematic optimization and sets the bounds for the problem space. Bounds can not be set for each time point, so it is important that the upper and lower bounds encompass the excursion of all DOFs

Load Template Job Names: This section loads the template job information from “DU01_IK_S2_JOBLIST.txt” and “DU01_IK_S2_JOBNAME.txt”. Each file has a string or a series of strings corresponding to the job command and names with flags for variable defined values such as %TASK%, %SEED%, and %FRAME%. Seed numbers are developed randomly for each increment to deal with ABAQUS jobs freezing in a few situations and locking read/write privileges to files, preventing further analysis.

Optimization Queue: This is the core of the optimization code for both inverse kinematics and static optimization. Assuming the job queue has been defined and is empty, this code loops through and creates threads to fill each spot in the queue. A thread will then launch the runSimplex( ) wrapper on the function runIKStep_matlab(), given a frame number and associated jobParams structure. This code manages optimization start, and code cleanup once optimizations finish. As an optimization completes, if there are more that need to be run, the completed spot in the queue will be collected, emptied, and replaced with a new thread which launches the runSimplex( ) wrapper on another frame number.

Load Best Results: The optimization will return the best results which are stored in structure J{}, but for improved redundancy the final section of the code will also be able to load best results from existing optimization results files.

runIKStep_matlab(x,jobParams): This function represents a single optimization iteration and takes a design vector (x) and job parameter structure filled with frame specific information. First a random seed is defined, and then main files and amplitude cards are built specific to the values associated with this iteration (seed) of the optimization. The runSimulation() is launched which uses a .NET library to launch and monitor the simulation process. A modified version occurs on Linux which does not have access to the .NET library but the code performs similarly. When the simulation completes IKCostFun( ) calculates the cost function of the optimization iteration. The cost function for inverse kinematics is defined as the sum of the squared error between model markers and subject marker data scaled by the weights found in MARKER-WEIGHTS.txt. If markers are occluded or removed in the trial marker data they are excluded from the weighted cost function calculation. Once the cost function has been calculated the simulation files are deleted for the current iteration and the design vector and cost function are written to DesignVector_[frameNumber].txt

### **BuildSOSimulation.m**

This script builds simulation files for muscle force estimation by performing static optimization on the joint kinematics obtained in the previous step. The static optimization consists of three steps. The first step moves the musculoskeletal model obtained in the previous section. The second step applies ground reaction forces and moment to the foot center of mass an applies a generic loading of muscle forces based off an initial guess. The third step applies a perturbation on the muscle forces to resolve the residual torque at the joints. The third step is the step which is used in the optimization routine to iterate to a solution.

*Functional Decomposition – Step 1*

Load Parameters / Kinematics: This section loads kinematics from the previous step and sets params needed for simulation setup.

Template File Check: Template files are used to build the simulation files. This step checks to see that the template files exist and throws a warning popup if they do not.

Build Step 1: Use MAIN and AMP template files to build frame specific files with kinematics obtained from IK.

*Functional Decomposition – Step 2*

Template File Check: Locate Template files for MAIN, AMP, ACT, and AMPGRF.

Create MAIN 2: Build step 2 MAIN files pointing to frame specific AMP, ACT, and AMPGRF files.

Create AMP 2: Build step 2 AMP files maintaining kinematics.

Create AMPGRF 2: Foot COM is obtained from the end of Step 1. Ground reaction forces and moments obtained from laboratory data specified in *viconforceplate* are transformed to the foot COM and written to amplitude cards.

Create ACT 2: Load EMG estimates or user defined activation guesses. Read resultant muscle geometry from step 1 and estimate muscle forces using defined activations. Write these activations to ACT amplitude cards.

*Functional Decomposition – Step 3 (Optimization Step)*

Template File Check: Locate template files for MAIN, AMP, ACT, and AMPGRF.

Create MAIN 3: Build step 3 MAIN files pointing to frame specific AMP, ACT, and AMPGRF files.

Create AMP 3: Build step 3 AMP files maintaining kinematics.

Create AMPGRF 3: Foot COM is obtained from the end of Step 2. Ground reaction forces and moments obtained from laboratory data specified in *viconforceplate* are transformed to the foot COM and written to amplitude cards.

Create ACT 3: Load EMG estimates or user defined activation guesses. Read resultant muscle geometry from step 2 and estimate muscle forces using defined activations. Write these activations to ACT amplitude cards. During static optimization, step 3 will obtain a design vector of muscle activations and update the step 3 ACT file accordingly.

### SOWrapper.m

This script performs muscle force estimation via static optimization given input simulation files provided by BuildSOSimulation( ). The software builds a simulation/optimization queue and fills it until all simulations/optimizations have completed.

*Functional Decomposition*

User settings: Define settings for simulations such as task, optimization parameters, and max number of cores to run jobs. NumCores is an important variable which defines how many threads to create at a time. Creating more threads than CPU cores is possible with this code and is problematic. Scaling parameters describing the combined cost function of muscle stress cubed and residual joint torque.

Optimization Guess: The code can be configured to load the previously described EMG estimates or user defined activation guesses and sets the bounds for the problem space. Bounds for muscle activations are [0 1].

Load Template Job Names: This section loads the template job information from “DU01_SO_S2_JOBLIST.txt” and “DU01_SO_S2_JOBNAME.txt”. Each file has a string or a series of strings corresponding to the job command and names with flags for variable defined values such as %TASK%, %SEED%, and %FRAME%. Seed numbers are developed randomly for each increment to deal with ABAQUS jobs freezing in a few situations and locking read/write privileges to files, preventing further analysis.

Optimization Queue: This is the core of the optimization code for both inverse kinematics and static optimization. Assuming the job queue has been defined and is empty, this code loops through and creates threads to fill each spot in the queue. A thread will then launch the runSimplex() wrapper on the function runSOStep_matlab(), given a frame number and associated jobParams structure. This code manages optimization start, and code cleanup once optimizations finish. As an optimization completes, if there are more that need to be run, the completed spot in the queue will be collected, emptied, and replaced with a new thread which launches the runSimplex() wrapper on another frame number.

Load Best Results: The optimization will return the best results which are stored in structure J{}, but for improved redundancy the final section of the code will also be able to load best results from existing optimization results files.

runSOStep_matlab(x,jobParams): This function represents a single optimization iteration and takes a design vector (x) and job parameter structure filled with frame specific information. First a random seed is defined, and then main files and muscle forces in the ACT amplitude cards are built specific to the values associated with this iteration (seed) of the optimization. The runSimulation() function is launched which uses a .NET library to launch and monitor the simulation process. A modified version occurs on Linux which does not have access to .NET but the code performs similarly. When the simulation completes SOCostFun() calculates the cost function of the optimization iteration. The cost function for static optimization is defined as the sum of the muscle stress cubed added to the residual joint torque (N*mm). Once the cost function has been calculated the simulation files are deleted for the current iteration and the design vector and cost function are written to DesignVector_[frameNumber].txt

# APPENDIX C. COMPUTATIONAL FRAMEWORK: EXAMPLE USAGE

The purpose of this appendix is to describe the steps taken to reproduce the results presented in Chapter 6 for the Subject 1 gait activity. Steps for model scaling, kinematics estimation, and muscle force estimation will be described in detail. Emphasis will be placed on workflow and areas which require user input. Input files for ABAQUS/Explicit will be developed and exported for analyses.

The goal is to make the computational framework, *ReadySim*, available on SimTK. SimTK is a modeling community with a large user base which submits and maintains a wide variety of tools, models, and software. It is the hope of this work that making the software open source will spur further work in high fidelity musculoskeletal modeling. This document will be transferred to the Wiki section of the ReadySim page on SimTK and will serve as a live document as the software continues to grow. Be sure to check SimTK for updated code and documentation if you're referring to this document elsewhere.

## Download and Deploy

ReadySim can and should be downloaded from the SimTK website to ensure current release of the software. Once downloaded, extract the archive using a compression tool such as WinZip or WinRar to a location on the computer which does not have read/write restrictions such as the Desktop or Documents folder. Inside the ReadySim folder you will find 4 different subfolders: Code, ExampleData, UnscaledFEModel, and Tutorial.

## Model Scaling

*The purpose of the model scaling module is to take a static subject marker trial obtained from the lab and use it to scale a generic MSFE model. Scaling can be performed along 3 axes for each segment and is based on the relative distances between markers placed on the model and markers seen in the static trial. The scaling module can be divided into 3 sections: Apply Markerset to MSFE Model, Calculate Segment Scaling Factors, and Scale MSFE Model.*

### *Apply the Markerset to the MSFE Model*

From the \ReadySim\Code\Framework\ folder open up ApplyNodeset2Model.m in MATLAB. Run the file to launch the GUI.

Load the FE bone geometry by clicking on "Load Geometry". You will be prompted to select the unscaled model folder and subsequently the input files corresponding to pelvis [BONE1-PELVIS.inp], femur [BONE2-FEMUR-DU01.inp], tibia [BONE3-TIBIA-DU01.inp], patella [BONE5-PATELLA-DU01.inp], and foot (midfoot) [BONE6-MIDFOOT.inp]. These files can be found in the \ReadySim\UnscaledFEModel\ folder. Each file takes between 5-30 seconds to parse nodes and elements into MATLAB.

Once the bones appear in the plot window, load in the static marker trial [KS05_STATIC_MARKERS.csv] located in \ReadySim\ExampleData\. At this point the GUI window should look as follows:

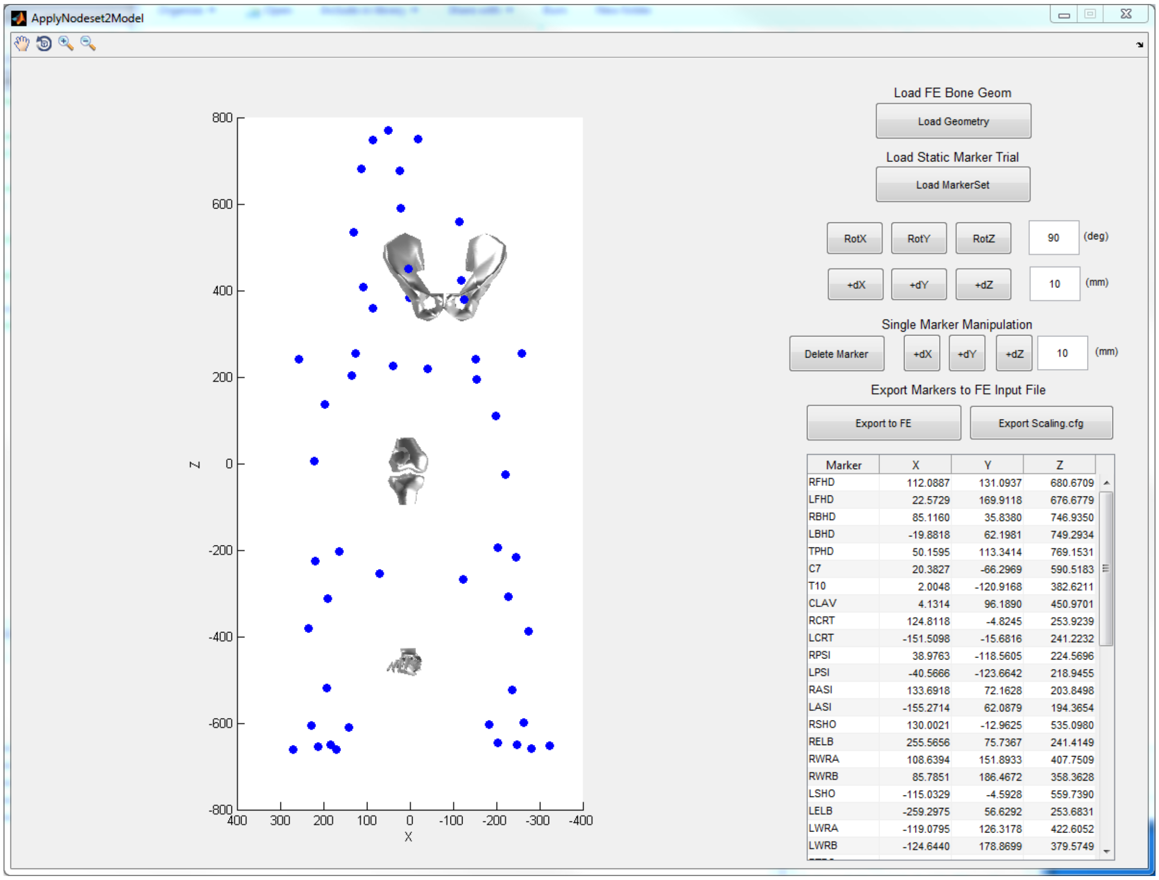

| Marker | X | Y | Z |
|---|---|---|---|
| RFHD | 112.0887 | 131.0937 | 680.6709 |
| LFHD | 22.5729 | 169.9118 | 676.6779 |
| RBHD | 85.1160 | 35.8380 | 746.9350 |
| LBHD | -19.8818 | 62.1981 | 749.2934 |
| TPHD | 50.1595 | 113.3414 | 769.1531 |
| C7 | 20.3827 | -66.2969 | 590.5183 |
| T10 | 2.0048 | -120.9168 | 382.6211 |
| CLAV | 4.1314 | 96.1890 | 450.9701 |
| RCRT | 124.8118 | -4.8245 | 253.9239 |
| LCRT | -151.5098 | -15.6816 | 241.2232 |
| RPSI | 38.9763 | -118.5605 | 224.5696 |
| LPSI | -40.5666 | -123.6642 | 218.9455 |
| RASI | 133.6918 | 72.1628 | 203.8498 |
| LASI | -155.2714 | 62.0879 | 194.3654 |
| RSHO | 130.0021 | -12.9625 | 535.0980 |
| RELB | 255.5656 | 75.7367 | 241.4149 |
| RWRA | 108.6394 | 151.8933 | 407.7509 |
| RWRB | 85.7851 | 186.4672 | 358.3628 |
| LSHO | -115.0329 | -4.5928 | 559.7390 |
| LELB | -259.2975 | 56.6292 | 253.6831 |
| LWRA | -119.0795 | 126.3178 | 422.6052 |
| LWRB | -124.6440 | 178.8699 | 379.5749 |

Select unnecessary markers from the list at the bottom right and delete them using the "Delete Marker" button. For the purposes of this tutorial the following markers were removed: RFHD, LFHD, RBHD, LBHD, TPHD, C7, T10, CLAV, RSHO, RELB, RWRA, RWRB, LSHO, LELB, LWRA, LWRB, LTRO, LTHI, LQAD, LKNE, LMKNE, LSHU, LTIB, LSHL, LANK, LMED, LHEE, LTIP, LTOE, LMET.

Next, use the two rows of buttons labeled "RotX", "RotY", "RotZ", "+dX", "+dY", "+dZ" to move the entire marker set as a whole. Lining up the pelvis markers is a good start when manipulating the entire set as it leads into simple single marker manipulations at the leg. Another approach might be to line up the long axis of the leg markers to the model limb and make single marker adjustments to the pelvis. The below image has used the first method to line up the pelvis. As you can see adjustments will need to be made to the entire marker set and thus the gross motion is a user preferred initial guess.

NOTE: Use the pan, rotate, and zoom buttons in the top left of the plot window to manipulate the view for effective marker placement.

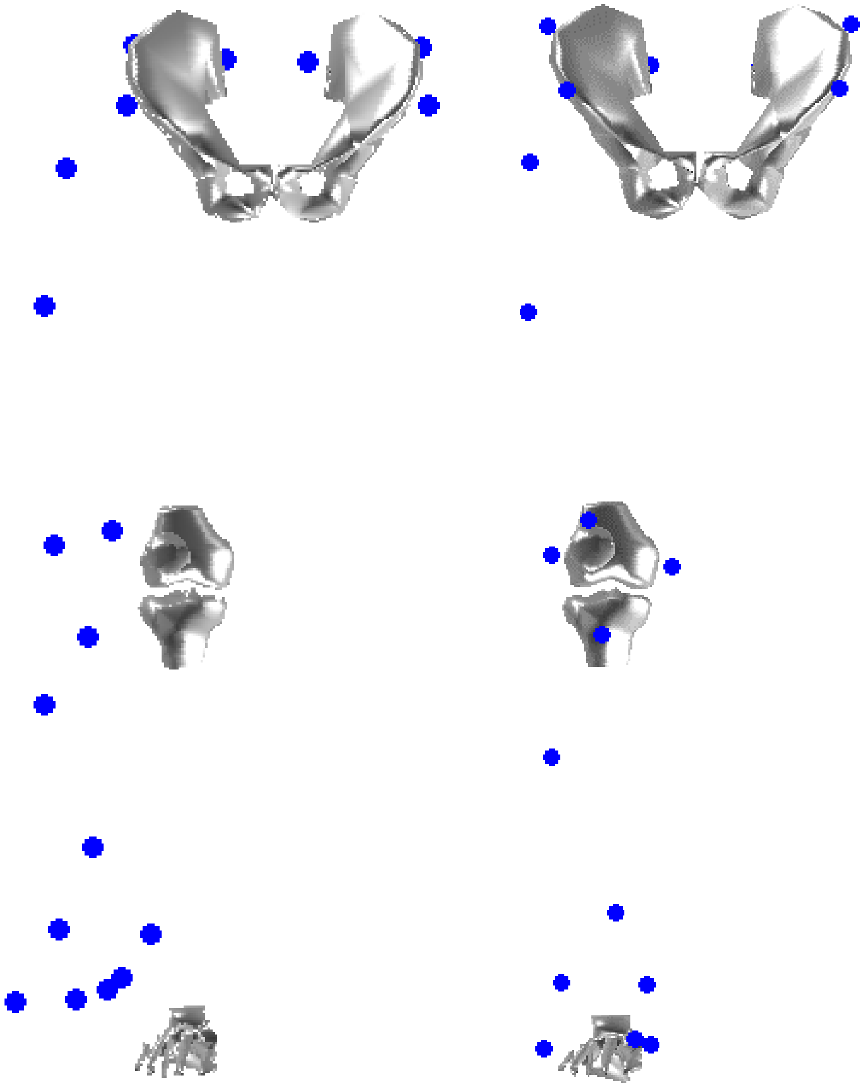

Next, use the buttons under Single Marker Manipulation, “+dX”, “+dY”, “+dZ” to manipulate the position of one marker in space and line it up with the segment or bony landmarks. Clicking on the marker in the list will allow you to use the buttons to translate it. Once this process is completed, clicking “Export to FE” will build an updated model marker file [MARKERS.inp] and place it in the \ReadySim\UnscaledFEModel\ folder. This marker file will then be copied into the scaled model folder in a subsequent step. Finally, the “Export ScalingConfig.txt” will export a file that points to location of the unscaled model, and marker file to expedite loading in future steps.

*Calculate Segment Scaling Factors for MSFE Model*

From the \ReadySim\Code\Framework\ folder open up CalculateSegmentScaling.m in MATLAB. Run the file to launch the GUI. Click “Load ScalingConfig.txt” and browse for the file exported in the unscaled model folder. After choosing this file, the loading in of nodal geometry, model markers, and static trial markers will take between 1-2 minutes to complete.

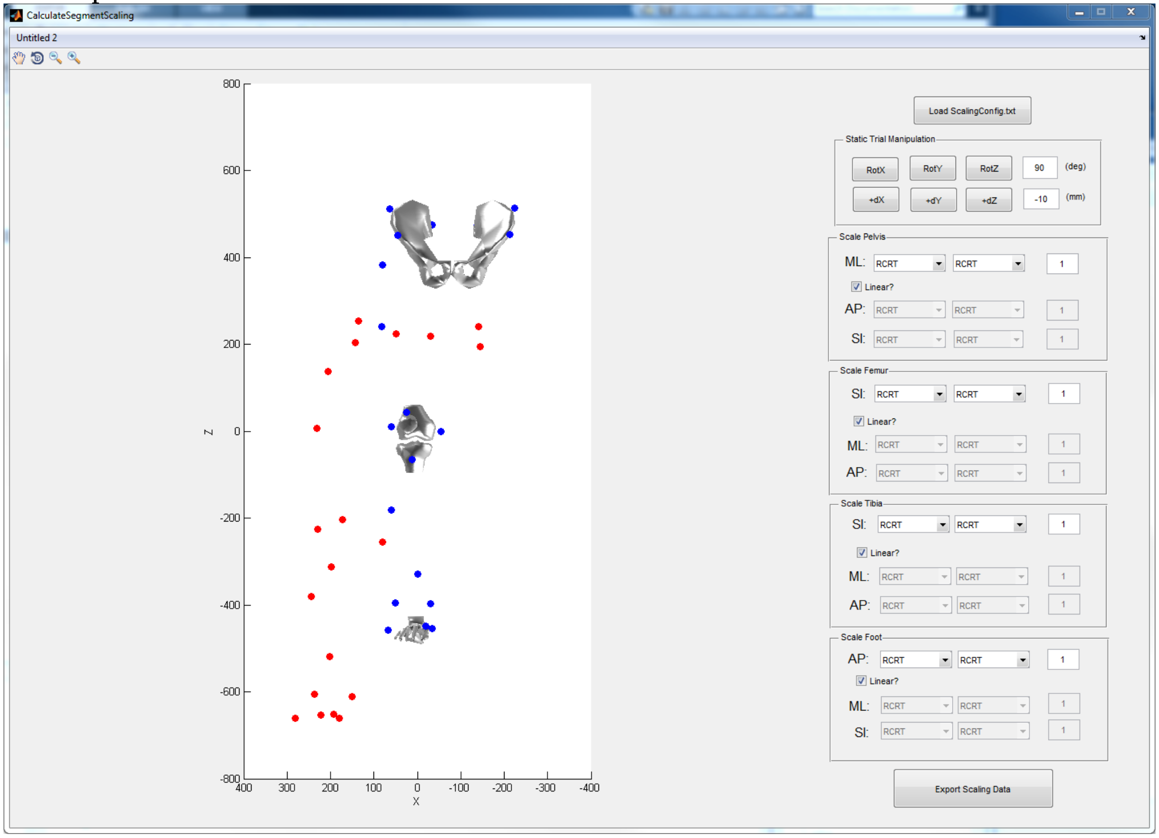

Once the model and markers have been loaded into the viewport the user can begin to define segment scaling factors for the ML, AP, and SI axes of each segment. Scaling can be performed linearly (all 3 axes use the same factor) or nonlinearly. For visual purposes, uses the Static Trial Manipulation section to translate the red markers representing the static subject trial so that comparisons can be easily made between model and subject. For this tutorial, the SI axis of femur [RASI, RKNE] and tibia [RKNE, RANK], the ML axis of the pelvis [RASI, LASI], and the AP axis of the foot [RHEE, RTOE] were scaled. Nonlinear, single dimension scaling was performed to best maintain moment arm geometry calibrated previously while scaling model segment lengths to match subject segment length. The scaling factors for pelvis, femur, tibia and foot were calculated as 1.12, 0.99, 0.96, 1.09, respectively. All remaining factors were kept at 1.0. Results may differ depending on placement of the markers onto the model in the previous step. Clicking the “Export Scaling Data” button will export ScalingParameters.mat to the unscaled model folder.

*Scale MSFE Model*

From the \ReadySim\Code\Framework\ folder open up ApplyScaling2MSFEModel.m in MATLAB. This m-file is not a GUI and has been designed using code cells which, when active, can be run using ctrl+enter.

At the beginning of the code the user will be prompted to browse for the ScalingParameters.mat file. This should be located in your unscaled model folder \ReadySim\UnscaledFEModel\. The next few cells load model markers and joint centers and build segment local coordinate systems and apply scaling parameters to these transformation matrices.

Next, the user is asked to browse for the Scaled Model Output Folder. This will need to be created, and the expected workflow would be to create the folder in the \ReadySim\ root folder. The software uses some file paths based on this folder placement. For this work the KS05 folder was created in \ReadySim\KS05\. Once the folder is selected files will be transferred which do not require scaling. The follow cells transfer files while scaling nodal geometry using the scaling matrices calculated previously for pelvis, femur, tibia, and foot. Next, the code updates the model segment masses (59kg for Subject 1), and anthropometrics.

Finally, the code updates the muscle modeling parameters based on the newly scaled segment lengths. Calibration jobs are run in ABAQUS\Explicit for both the unscaled MSFE model and the newly scaled MSFE model. The purpose of these jobs is to compare muscle force output between the two models to ensure proper scaling was performed and representative force production will occur. If the prescribed muscle forces at 50% activation differ by more than 5% between to two models the code will warn the user via the command line.

**Kinematics Estimation**

*The purpose of the kinematics estimation module is to take a dynamic marker trial obtained from the lab and use it to estimate kinematics for the scaled MSFE model. The kinematics module can be divided into 2 sections: setup, and kinematics optimization.*

*Build Simulation Setup Files for Kinematics Estimation*

From the \ReadySim\Code\Framework\ folder open up BuildIKSims.m in MATLAB. Run the file to launch the GUI.

Clicking the “Load Dynamic” button prompts the user to browse for a dynamic trial exported from Vicon Nexus 2.0+. Click the button and browse to the \ReadySim\ExampleData\ folder and choose KS05_12_MARKERS.csv, which corresponds to the gait activity.

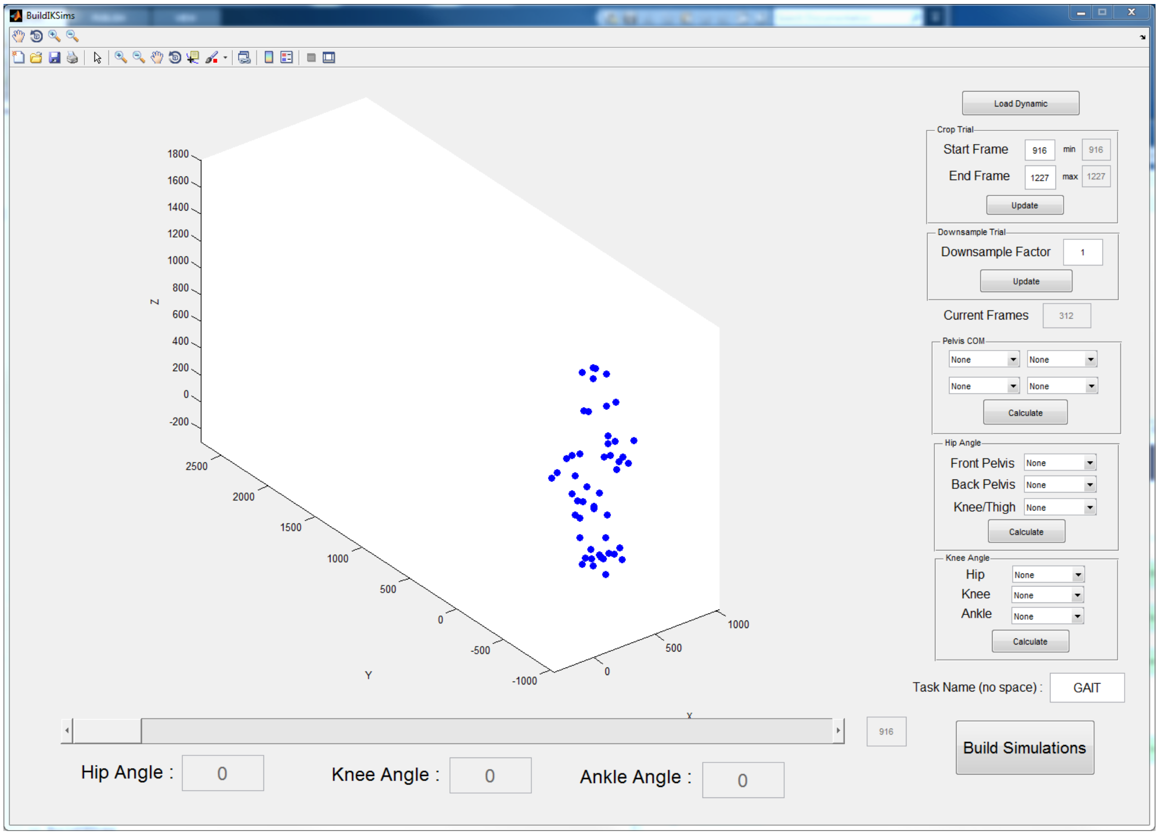

Start Frame 916 min 916

End Frame 1227 max 1227

Downsample Factor 1

Current Frames 312

Pelvis COM: None None None None

Front Pelvis None

Back Pelvis None

Knee/Thigh None

Hip None

Knee None

Ankle None

Task Name (no space) : GAIT

Hip Angle : 0

Knee Angle : 0

Ankle Angle : 0

The first step in setting up the IK simulations is to crop the trial to the region of interest. For the purposes of static optimization muscle estimation later, we will want to crop to a region where the foot is in contact with the forceplate. Set the start frame to 1069 and the end frame to 1155 and click update. The time bar, current frame, and the current frames will all updated with the new information for the cropped region. The region of interest includes 87 frames which would take a long time to run optimization on. To better facilitate parallel optimizations, we would like to down sample the input data. Setting the down sample factor to 20 will effectively sample at 5Hz, resulting in 6 optimization time points. Running 6 time points in parallel (6 threads) should be feasible on most desktop workstations.

Next the application requires you to define initial guesses for the pelvis location, hip and knee flexion angles. These values help seed the optimization to minimize required computational time. For Pelvis COM choose RASI, LASI, RPSI, LPSI and click ‘Calculate’. A red dot will appear at the calculated centroid location of those four markers. For hip angle, choose RASI, RPSI, and RKNE and click ‘Calculate’. The angle between those 3 markers will appear below the plot window and will update as the time bar is manipulated. Finally choose RTRO, RKNE, RANK and click ‘Calculate’. An estimate of knee angle will then be added below the plot.

Fill in a Task Name (GAIT for this tutorial) and click ‘Build Simulations’. You will be prompted to select the scaled model directory. For us, this corresponds to the \ReadySim\KS05\ folder. Choose this folder and click OK in the dialog box. Upon navigating to that location, you should now find AMP files (eg. AMP_DU01_IK_GAIT_1069_S1) and MAIN files (eg. MAIN_DU01_IK_GAIT_1069_S2) for the activity name, each of the subsampled frames, and two simulation steps. Finally, you will also find an InitialGuess_GAIT.txt. This file gets loaded and is used to the seed the optimization based on the location and angles we defined previously.

The optimization is divided into two steps: S1 and S2. S1 is a step which moves the model to the estimated location and prescribes the kinematics we calculated in the setup GUI. The second step is a perturbation step, which interfaces with the optimization and allows for faster simulation times. Therefore, before moving on to the optimization step, run the S1 main files for each time point. These can be run from the ABAQUS command prompt using the following command: “abaqus job=MAIN_DU01_IK_GAIT_1069_S1 double=both interactive”. This command will need to be run in separate ABAQUS command prompts for each job.

NOTE: If you are not certain of the number of virtual cores (threads) your CPU has, this is a good opportunity to make sure that your CPU usage doesn’t reach 100% while running these jobs. Be sure to understand the CPU capabilities before starting the semi-automated optimization routine.

*Perform Kinematics Estimation using Simplex Optimization*

From the \ReadySim\Code\Framework\ folder open up IKWrapper.m in MATLAB. This m-file is not a GUI and has been designed using code cells which, when active, can be run using ctrl+enter. It is important that this code is run from the \Framework\ folder as it adds other directories to the matlab path.

The first cell updates the path to include the \Framework\ folder as well as the optimization folder \FMINSEARCHBND\.

The next cell includes settings which must be updated by the user. Updating the absolute path of the rundir (scaled model folder) and jobParams.viconfile which points to the marker data from the dynamic trial. On my computer, and given the framework is located on my desktop, these two path locations are set to:
rundir =
'C:\Users\Donald\Desktop\ReadySim\KS05\';
jobParams.viconfile =
'C:\Users\Donald\Desktop\ReadySim\ExampleData\KS05_12_MARKERS.csv';
Update the paths to reflect your system configuration to point to these files and folders. This cell also reads the file “numCores.txt” to check for how many cores the user would

like the simulation to run on. Another way to think about this is how many parallel MATLAB optimizations should be run at once. A proper understanding of your CPU architecture is important for this step to prevent over utilization. In this example, we developed a simulation at 6 discrete time points in the gait phase. If our numCores file is set to 6, all simulations will be run in parallel. If the numCores file is set to 4, 4 simulations will be run in parallel. In this case the last two optimizations will begin once any of the first 4 simulations conclude. This adds considerable computational time and thus important considerations should be made when deciding on the subsample ratio to determine effective computational time.

The third cell initializes software settings, and the fourth cell defines bounds for the design vector and loads the initial guess which was exported to InitialGuess_GAIT.txt in the previous step. Marker weights are also loaded from MARKER-WEIGHTS.txt and used during the cost function calculation which performs a least-squares calculation of the model markers compared to the subject markers

The fifth cell loads job names which are used to make the call to ABAQUS and to clean up files post simulation.

The sixth cell is the core code which runs the optimization queue. It does not require any inputs not previously defined and should run inverse kinematics optimization on each time point defined in the IK Setup GUI. Once all simulations are completed the results will be parsed into ‘kin’ and ‘rmse’ variables in the MATLAB workspace. This code opens background instances of MATLAB to run each optimization.

NOTE: Dynamic pausing of optimizations is possible by editing the PAUSE_SIMS.txt file to 1. A value of 0 will continue the simulations. MATLAB batch instances will remain hooked while simulations are paused, however it frees computer resources if needed.

The final cell includes extra code to read the DesignVector_IK_GAIT_*framenum*.txt file which was written at each iteration and includes the cost function evaluation. This code is included so that optimization solutions can be obtained in the future if necessary (or to recover current results if the system goes down unexpectedly).

The final line of code is necessary to save results in KIN_*task*.mat (KIN_GAIT.mat) for the static optimization setup code which follows.

### Muscle Force Estimation

*The purpose of the muscle force estimation module is to model kinematics estimated in the previous step, apply ground reaction forces and moments to the foot, and estimate muscle forces which offset the residual torques that develop at the hip, knee, and ankle.*

*The muscle force optimization module can be divided into 2 sections: build setup files, and muscle force optimization.*

*Build Simulation Setup Files for Muscle Force Estimation*
From the \ReadySim\Code\Framework\ folder open up BuildSOSimulation.m in MATLAB. This m-file is not a GUI and has been designed using code cells which, when active, can be run using ctrl+enter.

The first cell defines paths for the runtime directory and forceplate file output from Vicon. Confirm that these files paths are correct considering the location of the \ReadySim\ folder. Force plate offsets are also included which are used when performing kinetic transformations to the foot. The code changes to the runtime directory (scaled model folder) and loads kinematics estimated in the previous step.

The remaining cells defined in this code are split into three groups that correspond to file generation for 3 different steps. The static optimization job was divided into three steps which (1) position the model kinematically based on the results of kinematics estimation, (2) apply ground reaction forces and moments and an initial muscle activation/force guess, and (3) [optimization] make perturbations to muscle forces. After the first two sections, an empty code cell prompts you to run the newly created files for Step 1 and Step 2.

Step 1 begins by checking that all necessary template files exist in the scaled model folder. These files will have been copied over during the model scaling step. A popup will prompt for any missing files. Next, MAIN files are generated based on the task name, and frame numbers. Then, AMP files are generated with amplitude curves defined for joint kinematics using the values estimated in the previous step. The user is then prompted to run the Step 1 ABAQUS simulations.

Step 2 begins in a similar fashion to Step 1 and checks for all necessary template input files. The user will be prompted if any template files are missing. MAIN files are generated for Step 2 as well as AMP files which maintain the kinematics prescribed in Step 1. Next AMPGRF files are generated which prescribe transformed force plate kinetic data to the foot COM. The applied kinetics to the foot COM are ramped from zero to the calculated value through the duration of the trial, with a period of settling at the end of the trial. The last section of Step 2 loads activation estimates (either from EMG or an educated guess), estimates muscle forces based on S1 model kinematics, and builds ACT files which ramp muscle forces to predicted values. Finally, the user is prompted to run Step2 ABAQUS simulations.

Step 3 begins by checking that all template files exist. MAIN, AMP, and AMPGRF files are generated which maintain the previously prescribed kinematics and kinetics. Transformed kinetics are updated based on the position of the new foot COM described by the kinematic changes seen at the tibiofemoral joint caused by application of muscle forces and ground reaction forces and moments. Muscle forces are also updated using the activations input to Step 2. Step 3 is the step which is used in the optimization routine, so these prescribed activations will be perturbed to solve for muscle forces at each time point. For now, the activations are held constant.

*Perform Muscle Force Estimation using Simplex Optimization*
From the \ReadySim\Code\Framework\ folder open up SOWrapper.m in MATLAB. This m-file is not a GUI and has been designed using code cells which, when active, can be run using ctrl+enter.

The first cell updates the path to include the \Framework\ folder as well as the optimization folder \FMINSEARCHBND\.

The next cell includes settings which must be updated by the user. Updating the absolute path of the rundir (scaled model folder). On my computer, and given the framework is located on my desktop, this path location is set to:

```
rundir =
'C:\Users\Donald\Desktop\ReadySim\KS05\';
```

Update the paths to reflect your system configuration to point to this folder. This cell also reads the file “numCores.txt” to check for how many cores the user would like the simulation to run on. Another way to think about this is how many parallel MATLAB optimizations should be run at once. A proper understanding of your CPU architecture is important for this step to prevent over utilization. In this example, we developed a simulation at 6 discrete time points in the gait phase. If our numCores file is set to 6, all simulations will be run in parallel. If the numCores file is set to 4, 4 simulations will be run in parallel. In this case the last two optimizations will begin once any of the first 4 simulations conclude. This adds considerable computational time and thus important considerations should be made when deciding on the subsample ratio to determine effective computational time.

The third cell initializes software settings, and the fourth cell defines bounds for the design vector and loads the frame numbers which were exported to InitialGuess_GAIT.txt in the previous step. The initial guess for optimization is described by a 20% activation across all muscles. EMG or an informed guess should be used in place of this to improve computational efficiency.

The fifth cell loads job names which are used to make the call to ABAQUS/Explicit and to clean up files post simulation.

The sixth cell is the core code which runs the optimization queue. It does not require any inputs not previously defined and should run static optimization on each time point defined in the SO setup code. Once all simulations are completed the results will be parsed into ‘acts’ and ‘rmse’ variables in the MATLAB workspace. This code opens background instances of MATLAB to run each optimization.

NOTE: Dynamic pausing of optimizations is possible by editing the PAUSE_SIMS.txt file to 1. A value of 0 will continue the simulations. MATLAB batch instances will remain hooked while simulations are paused, however it frees computer resources if needed.

The final cell includes extra code to read the designVector_SO_GAIT_*framenum*.txt file which was written at each iteration and includes the cost function evaluations. This code is included so that optimization solutions can be obtained in the future if necessary (or to recover current results if the system goes down unexpectedly).

The final line of code is used to save results in acts_*task*.mat (acts_GAIT.mat) for future analyses.